NTNU – Trondheim
Norwegian University of
Science and Technology

Fabrication of GaSb-based Y-junction Laser for Gas Spectroscopy

Kjetil Haddeland

Master of Science in Electronics
Submission date: July 2015
Supervisor: Bjørn-Ove Fimland, IET
Co-supervisor: Thanh-Nam Tran, IET

Norwegian University of Science and Technology
Department of Electronics and Telecommunications

To my beautiful wife; a ray of sunshine in a cloudy world.

Summary

Trace gas detection and pollution monitoring are becoming increasingly important for human safety and conservation of the environment. GaSb based semiconductor diode lasers, emitting in the mid-infrared wavelength region of 2–2.5 µm, are promising light source candidates for trace-gas sensing systems. In this wavelength-range, detection of gases like CO_2, CO and CH_4 with high selectivity and sensitivity is possible. For such systems, tunable light sources with a large tuning range, simple tuning scheme and large side-mode suppression ratio (SMSR) are in demand.

The Y-junction laser is a simple geometrical structure, increasing the tuning range of the optical device, without the need for complex processing steps. Two laser branches conjoin to form a folded Mach-Zehnder configuration, providing the ability for wavelength tuning by adjusting the current ratio into the two branches, which affects the interference in the merged branch.

This thesis describes the design, fabrication and testing of Y-junction laser and the related S-bend laser structure. S-bend lasers, which are an integral part of the Y-lasers, have been fabricated to investigate the relationship between curved waveguides and optical loss. The fabricated lasers show single-mode behaviour for waveguide linewidths $5\,\mu\mathrm{m}$ and below, with SMSR above $13\,\mathrm{dB}$ and output power exceeding $5\,\mathrm{mW}$. Waveguides with larger curvatures were found to exhibit larger losses. Both shallow-etch quasi-index guided waveguides and deep-etch index-guided devices were fabricated. The quasi-index guided devices have improved performance, with lower threshold current densities and increased slope efficiency.

Optimization of the ridge-waveguide etch and passivation layer etch-back is presented, laying the groundwork for improved performance in future devices.

Y-junction lasers were fabricated and large wavelength tunability $(19\,\mathrm{nm})$ and improved SMSR was demonstrated. Y-junction lasers based on the GaSb material system promises wide tuning range and simpler processing steps compared to competing structures in the mid-infrared wavelength range. Simpler processing means reduction of cost and increased yield.

Sammendrag

Deteksjon av sporgass og overvåkning av forurensing blir stadig viktigere for menneskers sikkerhet og miljø. GaSb baserte halvleder diode lasere som stråler i det mellom-infrarøde bølgelengdeområdet 2–2.5 µm er lovende kandidater som lyskilder i sporgass-deteksjonssystemer. I dette bølgelengdeområdet kan gasser som karbondioksid, karbonmonoksid og metangass detekteres med høy selektivitet og sensitivitet. Avstembare laserkilder som kan bølgelengdejusteres over et bredt bånd, har en enkel avstemmingsmekanisme og stor grad av monokromatisk utsråling, er i stor etterspørsel for slike systemer.

Y-laseren har en enkel geometrisk struktur som øker justeringsevnen uten behov for komplekse prosesseringssteg. To laser grener samles og danner et foldet Mach-Zehnder filter, hvor laserens bølgelengde kan justeres ved å endre strømforholdet inn i de to grenene, slik at interferens i den samlede grenen blir påvirket.

Denne oppgaven beskriver design, fremstilling og testing av Y-laseren og den relaterte S-bøy laser strukturen. S-bøy laseren, som er en viktig del av Y-laseren, har blitt fremstilt for å undersøke forholdet mellom bøy og optisk tap i bølgelederen. De fremstilte laserne viser stor grad av monokromatisk utstråling for bølgeledere med linjebredde i underkant av $5\,\mu\mathrm{m}$, med en side-mode reduksjon (SMSR) på $13\,\mathrm{dB}$ og utstrålt effekt i overkant av $5\,\mathrm{mW}$. Bølgelederne med størst bøy viste også et større optisk tap. Lasere ble fremstilt med både dyp-etsede indeks-ledende (IG-RW) og grunn-etsede kvasiindeksledende (QIG-RW) bølgeledere. De kvasiindeks-ledende laserne hadde bedre ytelse enn de indeks-ledende laserne fremstilt i dette arbeidet, med lavere terskelstrømtetthet og økt energikonverteringseffektivitet.

Optimalisering av etseprosessen for grunn-etsede bølgeledere og passiveringslag er presentert, som legger til grunn mulighet for økt ytelse i fremtidig fremstilte lasere.

Y-lasere har blitt fremstilt og demonstrerer stor justeringsevne av bølgelengden $(19\,\mathrm{nm})$ og økt SMSR i forhold til S-bend strukturen. Y-lasere basert på GaSb lover stor justeringsevne og enklere prosesseringssteg, sett i forhold til konkurrerende strukturer i det mellom-infrarøde spekteret. Enklere fremstilling betyr reduksjon av prosesskostnad og økt utbytte.

Preface

This thesis is submitted to the Norwegian University of Science and Technology (NTNU) for partial fulfillment of the requirements of the degree Masters of Science (MSc). The work has been carried out at the Department of Electronics and Telecommunications (IET) under the supervision of Bjørn-Ove Fimland and co-supervision of Thanh-Nam Tran.

To start, I would like to thank my supervisor, Bjørn-Ove Fimland, for guidance and the opportunity to work with laser diodes. A big thank you to my co-supervisor and collaborator Thanh-Nam Tran, for his tremendously helpful guidance and teaching of the fabrication process and numerous discussions related to it. Additionally, I would like to thank Saroj Kumar Patra, for his part in the growth of the laser diode material. I hope this thesis can be of help to them in their writing process and wish them good luck on finishing their PhD's. I would also like to thank Magnus Breivik for his insightful PhD thesis, from which this work was made possible.

Finally, I would like to thank my parents for all their support and high-spirits throughout the years leading up to this thesis.

Table of Contents

Chapter 1

Introduction

Detection and monitoring of gasous species is becoming of increasing importance for the safety of humans, especially where poisonous or otherwise harmful gases are present. Furthermore, as the consequences of pollution in the industrial and modern age are becoming more apparent, governments across the world are taking initiative to reduce emissions of green-house gases and conserve the environment. In order to comply with stricter regulations, reliable measurements of gas emissions are needed in the production-, energy- and transport industries. Additionally, optimization of plant performance in the processing industries are often dependent on accurate measurements of gas species, including pressure, flow and species concentration[1]. Both detection and measurement of such parameters can be achieved with optical absorption spectroscopy.

1.1 Background and motivation

A typical setup for absorption spectroscopy is depicted in figure 1.1. Monochromatic light is beamed through a sample volume containing the gas species and the attenuated beam is detected. By tuning the emission wavelength (λ) of the monochromatic light source a transmission spectrum can be recorded. The absorption spectrum is then found by subtracting the recorded intensity $I(\lambda)$ from the baseline $I_0(\lambda)$ of the light source. Light absorption in gas is related to quantum mechanical transitions induced by the incoming photons. If the frequency of radiation closely matches the energy difference between two

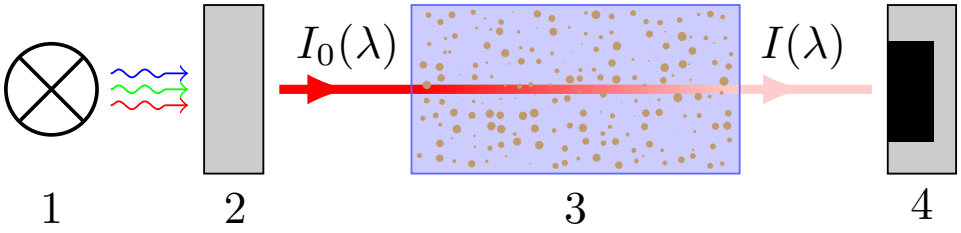

Figure 1.1: Experimental setup for absorption spectroscopy. 1: Light source; 2: monochromator; 3: sample volume; 4: detector. I_0 is the initial light intensity (also termed baseline) and I is the transmitted light intensity.

quantum states ($h\nu \approx \Delta E$), it is more likely for a transition to occur, creating an absorption line in the recorded spectrum. Since these transitions are primarily determined by the atomic and molecular composition of the gas, each gas has a unique spectral signature.

The absorption spectra of CO, CH_4 and H_2S in the mid-infrared (2–5 µm) is shown in figure 1.2. Overlap of absorption lines of different molecules increases the difficulty of detecting a specific gas. Typically atmospheric gases like CO_2 and H_2O interfere with real world systems, thus it is of particular interest to measure absorption lines in atmospheric windows, such as 2–2.35 µm as seen in figure 1.2. By measuring select absorption lines in atmospheric windows, accurate detection can be achieved even at low gas concentrations. One technique for absorption spectroscopy is tunable diode laser absorption spectroscopy (TDLAS). In TDLAS, the attenuation of a laser beam is measured, while the laser emission wavelength is tuned across a spectral region containing a particular absorption line of interest. The tunable laser diode (TLD) acts as both the light source (1) and monochromator (2) in figure 1.1.

A critical component in the TDLAS system is the TLD, which must fulfill a series of requirements for a given gas detection application. The center wavelength and tuning range of the TLD are important in determining which gas species can be analyzed by the TDLAS technique. Additionally, in the case of discontinuous tuning, the accessibility of wavelengths in the tuning range and the spectral resolution is of importance. The range of accessible wavelengths must coincide with the absorption line targeted for detection. In order to probe individual lines, the spectral linewidth of the lasing mode must be narrower than the absorption line, and the center wavelength of the mode must be tunable across the absorption line's spectral width. With a large tuning range, it is possible to detect multiple gas species with the same laser[2].

A desirable property of the TLD for TDLAS is room-temperature continous-wave (CW) operation and single-mode emission spectra, represented by large side mode suppression ratio (SMSR). The SMSR is the ratio of the dominant mode to the largest side mode, usually given in dB. Tuning of the laser is achieved by either modulating the injected current or operating temperature. Wavelength tuning by current modulation is faster and compatible with a wider range of applications[1]. The most common types of TLDs are distributed feedback (DFB) lasers, distributed Bragg reflector (DBR) lasers and vertical-cavity surface emitting lasers (VCSEL)[3]. The DFB and DBR lasers are Fabry-Perot (FP) type lasers and are edge-emitting, i.e. the light is emitted perpendicularly to the pump direction from the cleaved surface (edge) of a semiconductor crystal. These lasers typically have a small tuning range (1–$2\,\mathrm{nm}$), and highly divergent beams requiring external lenses for beam collimating. However, they can achieve a large SMSR ($> 30\,\mathrm{dB}$), which is important for the sensitivity in trace gas measurements[4]. The VCSEL exhibit a larger tuning range ($5\,\mathrm{nm}$[5]) and low beam divergence.

Junction structures offer a different approach to obtaining laser wavelength tunability. While DFB, DBR and VCSEL structures contain gratings as wavelength selective elements, the junction structures rely on interference of waves in multiple waveguides. The Y-junction laser is an interferometric laser structure that can obtain large tuning ranges ($> 40\,\mathrm{nm}$), but usually suffer from lower SMSR (up to $20\,\mathrm{dB}$)[3]. A potential benefit of this laser structure is cheaper processing, as it does not require sub-$\mu\mathrm{m}$ resolution for processing gratings. Additionally, it does not require any regrowth steps, which is common practice for creating widely tunable lasers [3]. The reduced process complexity, usually lead to an increase in processing yield and reduction in total processing cost.

1.2 Outline

This thesis, will describe fabrication and characterization of edge-emitting ridge-waveguide S-bend and Y lasers. The lasers are fabricated on a GaSb based laser diode material in NTNU NanoLab by standard cleanroom processing technology, such as mask aligner, plasma-etcher and e-beam evaporator. The main goal is to demonstrate the Y-junction laser as a potential light source candidate for TDLAS. The purpose of fabricating the S-bend lasers is to investigate the optical loss related to a curved waveguide.

In chapter 2 fundamental laser theory is presented, followed by a presentation of the lithographic mask design for tunable laser fabrication in chapter 3. Chapters 4 and 5 presents

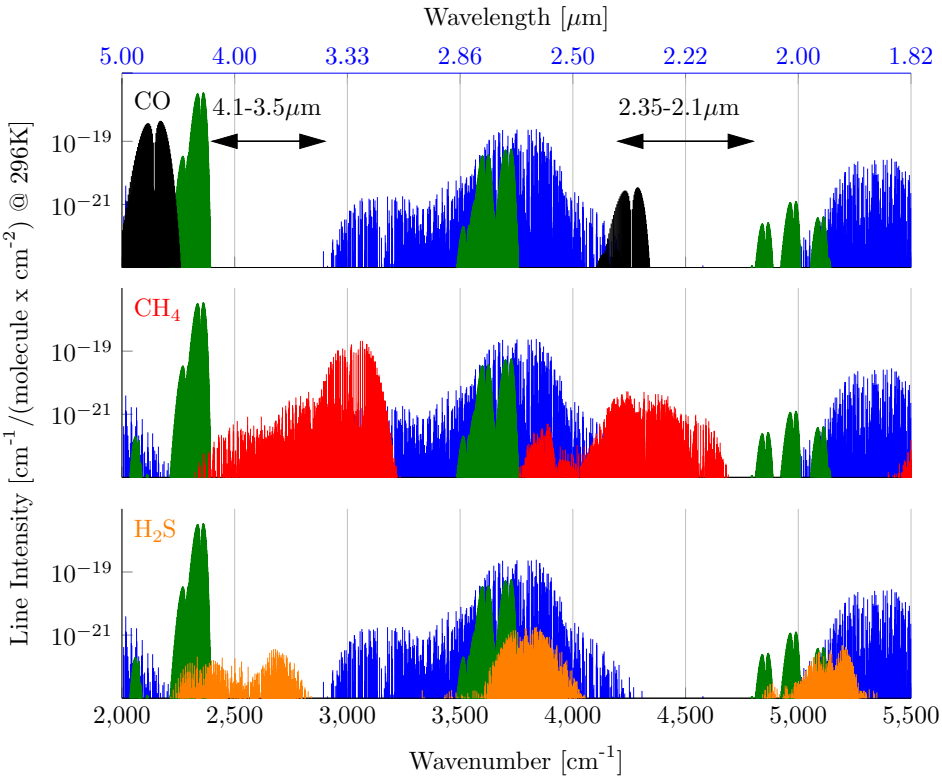

Figure 1.2: Absorption lines of CO, CH_4 and H_2S in the mid-infrared compared to absorption lines of CO_2 and H_2O in atmospheric conditions. Absorption from other atmospheric gases (e.g. N_2 and O_2) is negligible in the mid-infrared spectrum. Atmospheric absorption can be avoided in the spectral bands between 2.1–2.35 µm and 3.5–4 µm. Such atmospheric windows are ideally suited for detection of gases under atmospheric conditions, even at very low concentrations. The data is from the high-resolution transmission molecular absorption database (HITRAN) 2012 [6].

the processing and testing of the laser diodes, respectively. The relevant theory and techniques are presented first, followed by the results and discussion on a chapter-by-chapter basis. Finally, the conclusion and suggestions for further work is given in chapter 6.

Chapter 2

Laser Theory

Light amplification by stimulated emission of radiation (LASER) is a process involving generation of light by the mechanism known as stimulated emission. This section will give a brief introduction to some main aspects of laser theory. Three basic components are needed to achieve lasing; a gain medium, a waveguide and a resonator. The following sections will explain some fundamental concepts for these components, and introduce the concept of laser wavelength tuning. For a more detailed analysis, see Saleh [7] or Buus [3].

2.1 Gain medium: Interaction of radiation with atomic systems

There are three mechanisms for atomic transitions[7]:

Spontaneous emission: An atom in an excited energy level can spontaneously decay into a lower level releasing a photon with mode energy $h\nu$. Spontaneous emission is random in time, direction and phase and independent of number of photons already in a given mode. Spontaneous emission is characterized by the probability rate A_{mn}.

Absorption: An upwards transition of an atom, which is stimulated by absorption of one or more nearby photons. Absorption is characterized by the absorption transition coefficient B_{nm}.

Stimulated emission: Analogous to absorption, the presence of a photon can stimulate a downwards transition creating a second identical photon. Stimulated emission is characterized by the stimulated emission transition coefficient B_{mn}.

The three coefficients A_{mn}, B_{nm} and B_{mn} were first related by Einstein, and are often called the Einstein coefficients.

When a light beam propagates through a medium, stimulated emission and absorption processes will cause a change of the light beam power. The absorption coefficient α is defined by,

$$\frac{dI}{dz} = -\alpha I \tag{2.1}$$

By considering stimulated emission and absorption for a two level atomic system denoted by m (upper excited level) and n (lower level), and utilizing the Einstein coefficients for the processes and their relationship to the spontaneous emission probability A_{mn}, the following expression can be deduced:

$$\alpha = \frac{A_{mn}\lambda_{mn}^2}{8\pi} g(\nu)\left(\frac{g_m}{g_n}N_n - N_m\right) \tag{2.2}$$

Here $g(\nu)$ is the lineshape function, determining the line broadening mechanism of the $m \rightleftarrows n$ transitions, $g_{m,n}$ denotes the multiplicity of the atomic level (i.e. degeneracy) and $N_{m,n}$ is the population density of the level. If $\alpha > 0$ the intensity is decreasing as the wave propagates through the material, but if $\alpha < 0$ we have amplification. This occurs when:

$$\left(\frac{g_m}{g_n}N_n - N_m\right) < 0 \tag{2.3}$$

Assuming $g_m \approx g_n$, amplification requires $N_m > N_n$, i.e. more atoms in the upper level m than in the lower level n. This condition is referred to as *population inversion* and is one of the requirements necessary to achieve lasing action. In this case it is useful to define the gain as $\gamma = -\alpha$. In a semiconductor laser diode, the atomic levels m and n are replaced by the conduction and valence band. To achieve population inversion in a laser diode, we inject electrons into the conduction band and holes into the valence band. Recombination of the electron-hole pairs, both by stimulated- and spontaneous emission,

then emit radiation with center frequency ν given by the bandgap energy E_g, or difference between the conduction band energy E_c and the valence band energy E_v:

$$h\nu = E_c - E_v = E_g. \tag{2.4}$$

2.2 Waveguide: Optical confinement of light

At the interface between two media of different refractive index, n_1 and n_2, light rays are split into two; a reflected and a refracted ray. Refraction, described by Snell's Law (2.5), is illustrated for a three slab waveguide in figure 2.1.

$$\begin{aligned} n_1 \sin\theta_1' &= n_2 \sin\theta_2' \\ &\Downarrow\ \theta_{1,2} = 90^\circ - \theta_{1,2}' \\ n_1 \cos\theta_1 &= n_2 \cos\theta_2 \end{aligned} \tag{2.5}$$

When talking about waves propagating along the interfaces it is more useful to use $\theta_{1,2}$. When a wave crosses an interface with $n_2 > n_1$ we have internal reflection. A phenomenon known as total internal reflection occurs when (2.5) can not be satisfied:

$$\theta_2 < \theta_c = \cos^{-1}\left(\frac{n_2}{n_1}\right) \tag{2.6}$$

where θ_c is known as the critical angle. All incident waves travelling at an angle lower than the critical angle is reflected at the interface. By utilizing a three layer slab structure as shown in figure 2.1 the light can be trapped inside the middle layer, creating a waveguide. The middle layer is commonly referred to as the core, while the outer layers are known as the cladding. In the diode laser, this principle is used to confine the light in the active layer of the device, but also in the lateral direction, typically by etching a ridge structure in the laser diode material (see chapter 4).

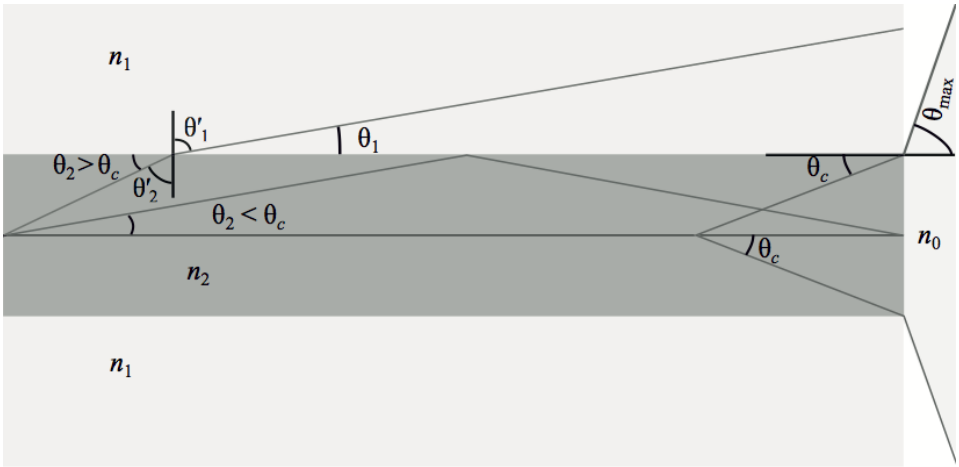

Figure 2.1: A sketch of a three layer slab waveguide with $n_2 > n_1$[8]. Total internal reflection occurs for angles $\theta_2 < \theta_c$ confining light propagating along the waveguide. A low refractive medium n_0 surrounds the waveguide, typically air, and due to the large refractive index difference $n_2 - n_0$ there is significant refraction at the interface.

2.3 Resonator: Selection of resonating wavelength

The simplest optical resonator structure is referred to as a Fabry-Perot (FP) etalon and consists of two planar mirrors facing each other. By placing the waveguide and active gain medium between these mirrors the basic Fabry-Perot laser (FPL) structure is created. Consider a plane wave propagating incident on the FP resonator with incident field amplitude of E_i, as shown in figure 2.2. By adding all the partial waves at the output we get the total output E_t.

$$\begin{aligned} E_t &= t_1 t_2 E_i e^{-j\beta^* L}\left[1 + r_1 r_2 e^{-2j\beta^* L} + r_1^2 r_2^2 e^{-4j\beta^* L} + ...\right] \\ &= E_i\left[\frac{t_1 t_2 e^{-j\beta^* L}}{1 - r_1 r_2 e^{-2j\beta^* L}}\right] \\ &= E_i\left[\frac{t_1 t_2 \cdot e^{-jk_0 n_{\text{eff}} L} \cdot e^{-j\gamma_{\text{eff}} - \alpha_i L}}{1 - r_1 r_2 \cdot e^{-2jk_0 n_{\text{eff}} L} \cdot e^{(\gamma_{\text{eff}} - \alpha_i)L}}\right] \end{aligned} \tag{2.7}$$

In the last step the complex propagation constant β^* was used given by

$$\beta^* = k_0 n_{\text{eff}} + j\left(\frac{\gamma_{\text{eff}} - \alpha_i}{2}\right) \tag{2.8}$$

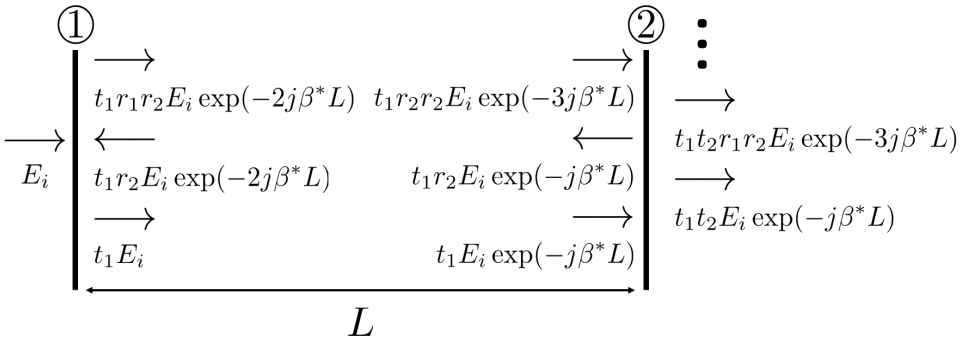

Figure 2.2: A schematic of wavecomponents in a Fabry-Perot resonator. E_i is the incoming wave, $r_{1,2}$ and $t_{1,2}$ are the amplitude reflection and transmission coefficients for mirror 1 and 2, respectively.

where $k_0 = \frac{2\pi}{\lambda}$ is the vacuum wavenumber, n_{eff} is the effective refractive index. $\gamma_{\text{eff}} = \Gamma\gamma_a$ is the effective contribution of the gain-curve in the active medium and α_i is the internal loss. Γ is the confinement factor, which measures the mode power confined within the active layer relative to the total power [9]. If we have population inversion then $\gamma_{\text{eff}} > 0$ and it is possible to have $\left|E_t/E_i\right| \gg 1$. Considering (2.7) the condition for oscillation can be deduced:

$$r_1 r_2 \cdot e^{-2jk_0 n_{\text{eff}} L} \cdot e^{(\gamma_{\text{eff}} - \alpha_i)L} = 1 \tag{2.9}$$

With (2.9) we have $\left|E_t/E_i\right| \to \infty$. The physical interpretation of this is that we have a finite E_t with zero incoming field, i.e. the laser oscillation is coming from within the laser medium. Equation (2.9) corresponds to a wave making a complete round-trip in the resonator, ending up having the same amplitude as it started with. The threshold gain γ_t can be found from solving (2.9) for the real part

$$\gamma_t = \alpha_i + \alpha_m \tag{2.10}$$

where α_m represents the mirror loss

$$\alpha_m = \frac{1}{2L} \ln\left(\frac{1}{R_1 R_2}\right) \tag{2.11}$$

and $R_i = r_i^2$ is the mirror reflactance. By solving the imaginary part of (2.9) for λ we find the longitudinal modes of the resonator

$$\lambda_N = \frac{2n_{\text{eff}}(\lambda_N)L}{N} \tag{2.12}$$

and the mode spacing, or free spectral range (FSR), can be approximated to

$$\Delta\lambda_m = \lambda_N - \lambda_{N+1} \approx \frac{\lambda_N^2}{2n_{\text{g,eff}}L} \tag{2.13}$$

$$n_{\text{g,eff}} = n_{\text{eff}}(\lambda_N) - \lambda_N \frac{dn_{\text{eff}}}{d\lambda}\bigg|_{\lambda_N} \tag{2.14}$$

where $n_{g,\text{eff}}$ is the effective group index accounting for dispersive media, in which the effective refractive index is dependent on the emission wavelength. The longitudinal modes with the initial effective gain larger than the losses will begin to grow, thereby saturating the gain by depleting the population difference. The modes closest to the central frequency of the gain-curve will grow quickest and aqcuire the highest photon-flux densities[7].

The intensity of the FP modes can be found by using (2.7) and setting $I = |E_t|^2 = E_t \cdot E_t^*$. Excluding gain and internal loss in the medium, and using trigonometric identities leads to the following expression for the resonator modes

$$I = \frac{I_{\text{max}}}{1 + (2\mathcal{F}/\pi)^2 \sin^2(k_0 n_{g,\text{eff}} L)}, \quad I_{\text{max}} = \frac{t_1^2 t_2^2 E_i^2}{(1 - r_1 r_2)^2} \tag{2.15}$$

where the finesse of the resonator is

$$\mathcal{F} = \frac{\pi\sqrt{r_1 r_2}}{(1 - r_1 r_2)} \tag{2.16}$$

The finesse is defined as the resonator FSR divided by the FWHM of the resonant modes. When the finesse is large the spectral response of the resonator is sharply peaked about the resonance frequencies. Including the gain in the laser cavity in the above derivation will result in an increase in the finesse of the resonance modes and therefore a narrowing of the FP modes [7].

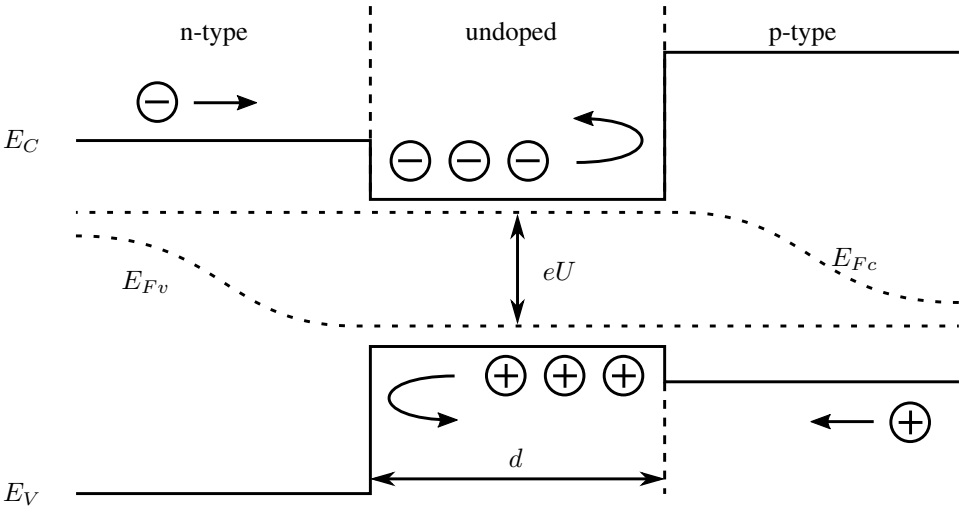

Figure 2.3: Simplified illustration of a semiconductor double heterostructure band diagram. The upper line is the conduction band energy E_C, while the lower line is the valence band energy E_V. The semiconductor heterostructure is under forward bias U, as characterized by the splitting of the quasi-Fermi levels E_{Fc} and E_{Fv} [3].

2.4 Quantum wells: Confinement of charge carriers

Transverse confinement of injected carriers overlapping the confined optical field can be achieved using a semiconductor double heterostructure, in which the active layer is surrounded by a higher-bandgap material, creating a potential well for the charge carriers[3]. A schematic illustration of a forward-biased double heterostructure is shown in figure 2.3. Electrons are injected into the small-bandgap undoped active region from the n-doped confinement layer with higher bandgap energy. Similarly, the holes enter the active region from the p-doped confinement layer on the opposite side. Due to the high-bandgap confinement layers on both sides of the active region, electrons cannot escape into the p-type confinement layer, and holes cannot escape into the n-type confinement layer. The carriers are trapped in the active region where they are forced to recombine. Additionally, since the refractive index is inversely proportional to the bandgap energy, the higher-bandgap confinement layers will have a refractive index smaller than the active region, confining the optical field to the active region.

A quantum well (QW) consists of a double heterostructure where the active layer thickness d is smaller than the de Broglie wavelength of a thermalized electron ($\approx 15\,\mathrm{nm}$[3]). Because of quantization of the available states in the conduction and valence bands of

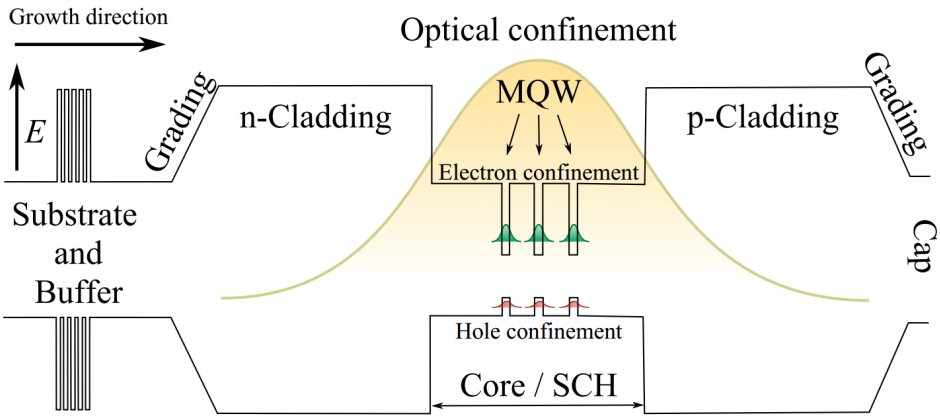

Figure 2.4: A sketch of GRINSCH-MQW laser diode band diagram. The top line is the conduction band and the lower line is the valence band. The layers are described in detail in [8]. The substrate and buffer improves the crystal quality and uniformity, while the grading layers reduce the diode voltage. The cladding layers provide both optical and electrical confinement. The core provides an increased refractive index for waveguiding and further confinement for the charge carriers. The MQW comprise of three QWs, providing gain for the stimulated emission process. Note that the band diagram does not illustrate a thermal equilibrium situation, in which band bending would occur to equalize the Fermi level across the band diagram.

the QW, the effective band gap energy is increased, and can be tailored to the desired recombination wavelength $\lambda = hc/E_g$ by engineering the QW thickness d [3]. Additionally, a quantization of the density of states in the well region will result in an increase in the height and decrease of the width of the gain-coefficient curve $\gamma(\nu)$, which lowers the threshold current I_{th}, increases the external quantum efficiency η_d and narrows the laser linewidth $\Delta\nu_\nu$ [7]. However, the improvements on the gain curve in the QW structure may entirely cancel out by the smaller confinement factor Γ, due to the thin active layer. To address this, an additional optical waveguide around the QW, called a separate confinement heterostructure (SCH), can increase the optical confinement. Additionally, this SCH can be compositionally graded, resulting in a graded refractive index separate confinement heterostructure (GRINSCH), where the optimization of optical confinement and carrier confinement are effectively decoupled so that the optical confinement factor Γ can be significantly improved. The core can also consist of multiple QWs, in which case it is referred to as a multiple quantum well (MQW) structure. The lasers fabricated in this work have a GRINSCH-MQW structure, as illustrated in figure 2.4.

2.5 Tunable lasers

Tuning of the laser wavelength can be achieved by tuning the comb-mode spectrum of the laser (2.15), by tuning the gain curve $\gamma(\lambda)$ or by a combination of these. Depending on how the tuning is performed, and which structure is used, we may distinguish between three tuning schemes: continuous, discontinuous and quasicontinuous tuning. In the continuous tuning scheme the wavelength can be tuned smoothly in arbitrarily small steps. This typically requires a combination of gain curve- and comb-mode tuning and is usually limited to a small tuning range. In the discontinous tuning scheme, the wavelength can be tuned across a larger range, but are accompanied by longitudinal mode changes (mode hopping), such that not all wavelengths in that range are accessible. An intermediate tuning behaviour can also be achieved in the quasi-continous scheme, where small overlapping continous regimes can be joined to provide access to all wavelengths in the tuning range. The mode hopping in both the discontinous and quasicontinuous scheme are related to the tuning of the comb-mode spectrum[3].

Tuning of the lasing wavelength is usually achieved by changing the effective refractive index of the core, which leads to a change in the optical path length and thus the mode wavelength (2.12). For FPLs the wavelength will be tunable across the mode spacing (2.13), at which point the neighbouring FP mode becomes the dominant mode and the wavelength jumps back to the original lasing wavelength (mode hopping). The physical mechanism that is most frequently used to change the effective refractive index is the free-carrier plasma effect (FCPE). In FCPE, the refractive index change Δn is due to the polarization of free carriers and a spectral shift of the absorption edge in the active region. The increment Δn change for the carrier injection density N in an undoped active region is[3]

$$\Delta n = -\frac{e^2\lambda^2}{8\pi^2 c^2 n \epsilon_0}\left(\frac{1}{m_e}+\frac{1}{m_h}\right)N \tag{2.17}$$

where m_e and m_h denote the effective masses of the injected electrons and holes, respectively. The shift in wavelength $\Delta\lambda$ for a FPL due to Δn is given by[3]

$$\Delta\lambda = \lambda\frac{\Gamma\Delta n}{n_{g,\text{eff}}} \propto -N \tag{2.18}$$

where $n_{g,\text{eff}}$ appears in the denominator to account for the wavelength dependence of n_{eff}.

The carrier density N is related to the current density j by the relationship

$$j = ed\left(N/\tau_s + BN^2 + CN^3\right) \tag{2.19}$$

where $1/\tau_s$, B and C are the recombination rates of impurity, band-to-band and Auger recombination, respectively[1], and d is the active layer thickness. The tuning efficiency $d\lambda/dj$ is large at small tuning currents and significantly decreases with increasing tuning current due to the square-root-like N-j relationship in (2.19). A more detailed analysis of tuning mechanisms can be found in [3].

[1] See textbook [7] or [3] for a detailed explanation of the recombination mechanisms in atomic systems.

Chapter 3

Design of Mask for Tunable Laser Fabrication and Optimization

Two 5×5 inch masks were designed with multiple patterns for ridge-waveguide (RW) etch and metallization. Each pattern size is approximately $(15\text{–}20) \times 11\mathrm{mm}$ to fit with the typical sample size. In the first mask the focus was on the design of S-bend, Y- and other types of interferometric lasers with waveguide widths $(1.5,\ 2.0$ and $2.5)\ \mu\mathrm{m}$ and with support structures placed near the ends of the waveguides. The purpose of these structures is to give mechanical support to the etched ridges during the cleaving process. In the second mask, the focus was on design of S-bend and Y-lasers without the mentioned support structures, as the additional topography was found to cause problems with the insulation layer uniformity, thereby making the insulation etchback process more complicated[10]. Previous experiments has found that unsupported waveguides tend to crack due to the stress/strain in the cleaving process. It was therefore determined to increase the waveguide width in the unsupported designs to $(2.5,\ 5.0,\ 8.0,\ 15.0$ and $25.0)\ \mu\mathrm{m}$ for the S-bend lasers. However, due to constraints on the dimensions, the waveguide width of the Y-lasers were kept below $5.0\,\mu\mathrm{m}$ and set to $(1.5,\ 2.5$ and $5.0)\ \mu\mathrm{m}$, respectively. The full schematic overview of the patterns included is given in figure 3.7, for mask 1, and figure 3.8 for mask 2. A detailed description of the design and use of the different waveguides follows.

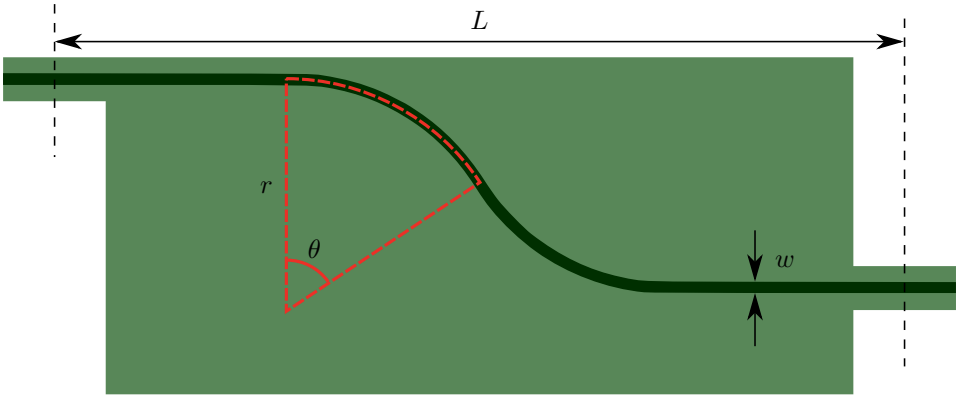

Figure 3.1: Illustration of the top-down design of the S-bend laser waveguide etch- (black), and corresponding metallization lithography pattern (green overlay). The lasers are characterized by the radius of curvature of the bend r, the waveguide width w, the straight waveguide cavity length L and the difference in cavity length dL due to the bend (in comparison to L). dL is related to the arc angle θ through the geometrical expression given in (3.1). The dashed lines at the ends of the waveguide illustrate where the laser waveguide is intended to be cleaved.

3.1 S-bend laser

The top-down design of the S-bend laser is illustrated in figure 3.1. The S-bend laser is an integral part in the interferometric lasers investigated in this work. The purpose of fabricating the S-bend laser is to investigate the optical power loss from light leaking out of the waveguide in the curved segments, and thereby optimize the design of the interferometric laser by selecting the bends best fit for waveguiding. In figure 3.2 excerpts of S-bend design in mask 1 illustrates the 5 different bend types selected for study in this work. The bends are characterized by the radius of curvature r and the difference in cavity length dL in comparison to the straight waveguide. The relationship between dL and the arc angle of the bends is given by

$$dL = 2r(\theta - \sin\theta) \tag{3.1}$$

Preceding work showed that there is a risk of damaging the laser facet during the cleaving process, if the waveguide width w is smaller than $10\,\mu\mathrm{m}$ [11]. Therefore, the lasers in mask 1 was designed with structures to give mechanical support for the etched ridge during the cleaving process, as can be seen in figure 3.2. The support structures were designed to be a minimum of $100\times100\,\mu\mathrm{m}^2$ in size and were placed $50\,\mu\mathrm{m}$ from the side-edge of the

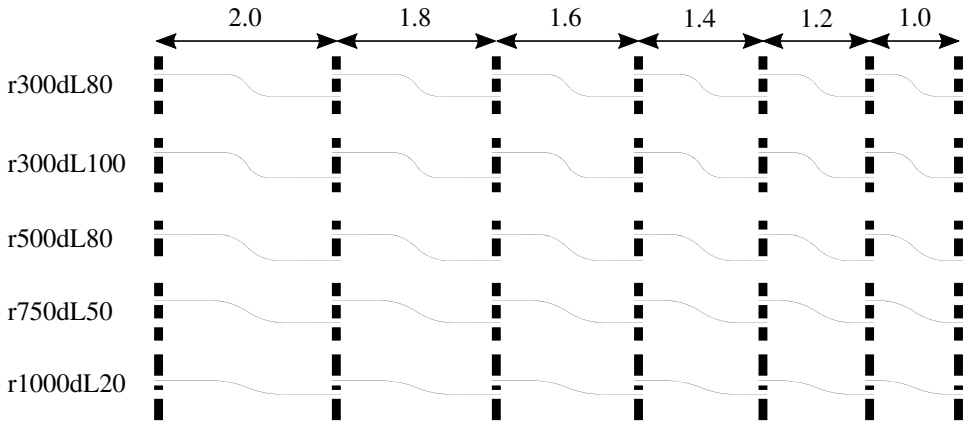

Figure 3.2: Excerpts from the S-bend mask design from mask 1 with waveguide width $2.5\,\mu\mathrm{m}$ illustrating the different bend types designed and their layout on the mask. The designed patterns each consist of 10 waveguides of two bends, with lengths $(1.0, 1.2, 1.4, 1.6, 1.8 \text{ and } 2.0)\,\mathrm{mm}$.

waveguides.

In comparison to the waveguides, the support structures are relatively large structures which contribute locally to the topography of the etched samples. It was found that this topography difference along the ends of the ridges results in an issue with the deposition uniformity of the insulation layer, as discussed later in chapter 4. Accordingly, it was decided to omit the support structures from most of the patterns in the second mask in order to avoid this problem.

3.2 Y-laser

The design of the Y-laser is shown in figure 3.3. It consists of a combination of two waveguides with a cavity length difference dL that are joined in a common branch. A metal pattern separates the contact between the common, straight and bent branch, allowing for separate electronic control of the two FP cavities. The two cavities will interfere in the common branch, creating a beating between the individual comb-mode spectra, as illustrated in figure 3.4. The beating between the two FP cavity modes gives rise to a beating wavelength spacing, or free spectral range, of

$$\Delta\lambda_Y = \frac{\lambda^2}{2n_{g,\text{eff}}dL} \tag{3.2}$$

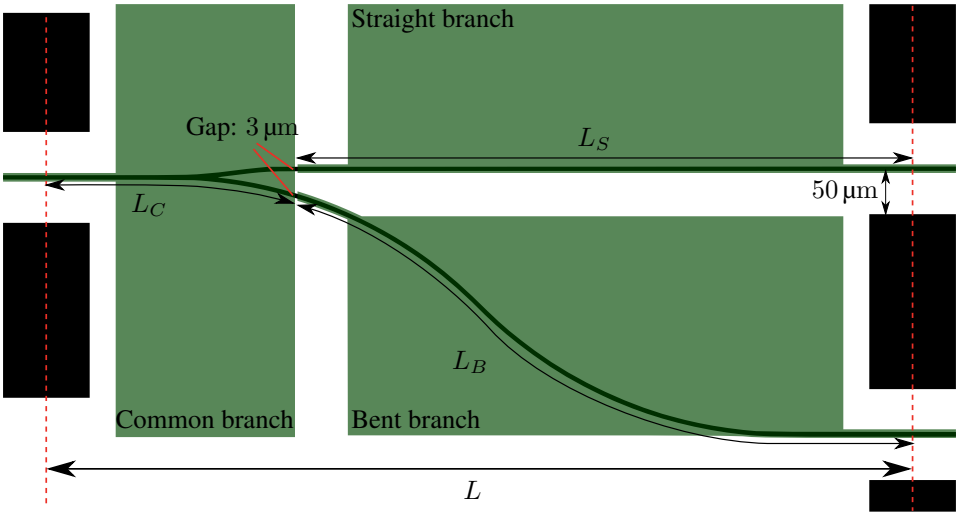

Figure 3.3: Illustration of the top-down design of the Y-laser etch- (black), and corresponding metallization lithography pattern (green overlay). To achieve 50-50 splitting of the light, the Y-junction must be symmetric. Therefore the Y-laser consists of a combination of an approximately straight waveguide $L_C + L_S \approx L$, and a curved waveguide $L_C + L_B$. The displayed Y-laser has a bend radius $r = 500\,\mu\text{m}$ and cavity length difference $dL = L_B - L_S = 80\,\mu\text{m}$. A $3\,\mu\text{m}$ gap separates the three metal contacts. The wavelength tuning mechanism is achieved by changing the effective refractive index as a result of tuning the injected current into the separate branches. The picture also illustrates the support structures along the cleaving lines (red dashed lines). The support structures were included for the Y lasers in mask 1.

which induces a modulation to the cavity gain by a factor[3]

$$C_Y(\lambda) = \cos^2\left(2\pi \frac{n_B(\lambda)L_B - n_S(\lambda)L_S}{\lambda}\right) \tag{3.3}$$

where n_S and n_B is the refractive index in the straight and bent sections, respectively. By tuning the current into these branches, a small refractive index change can be made, thereby changing the modulation gain factor and tuning the wavelength. A more detailed description of the design and tuning schemes of the Y-laser is given in [12].

Since dL is much smaller than the cavity length of either the straight or S-bend cavities in the Y-laser, the free spectral range of the Y structure (3.2) is larger than that of the FP structure (2.13). This increases the maximum wavelength tuning range from $\Delta\lambda$ ($\approx$ 1–2 nm) for the FPL to $\Delta\lambda_Y$ (up to 50 nm) for the Y-laser structure [3]. Additionally, the ratio of the intensity in the dominant mode to the neighbouring side-mode, a quantity

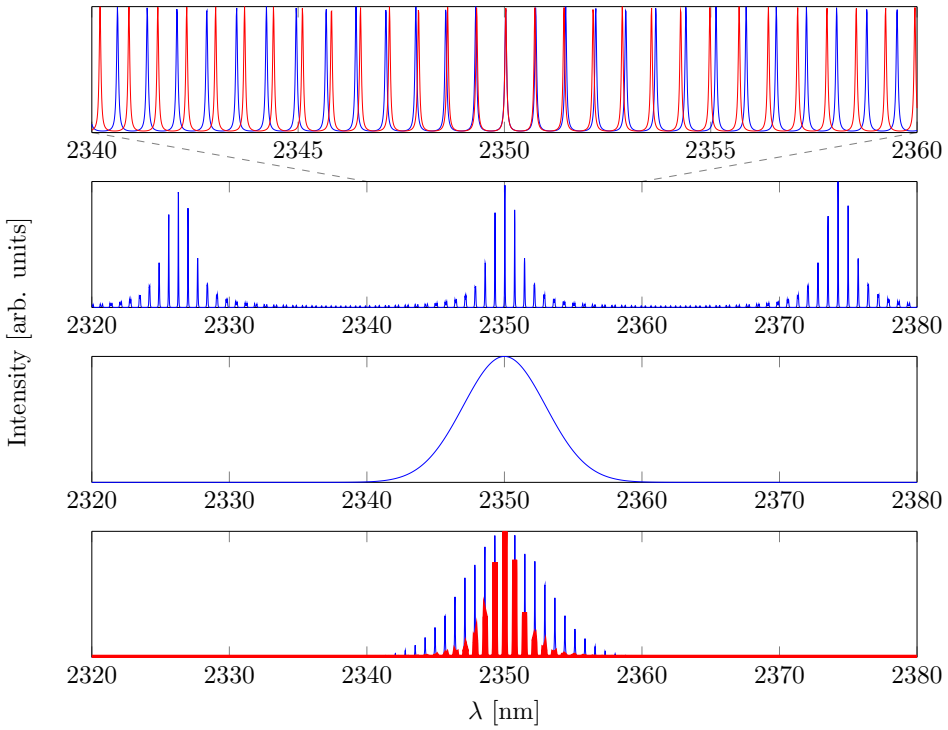

Figure 3.4: Illustration of the mode selection in the Y-laser. From the top, **1:** Comb-mode spectrum for $R = 0.8$, $n_{g,\text{eff}} = 3.8$ (blue) and 3.80112 (red), and L =1 mm and 1.03 mm. The modes were calculated using (2.15). **2:** Mode overlap, Mode 1 $\times$ Mode 2, the free spectral range due to the beating of the modes $\Delta\lambda_Y$ is improved over the free spectral range of the individual FPL modes. **3:** Gaussian gain curve. **4:** Gain for the Y-junction laser structure (red) in comparison to the gain for a single resonator cavity (blue). The SMSR is improved in the Y-laser. Note that the mirror reflectance of GaSb-based lasers is usually close to $R = 0.3$, but have been chosen higher here to reflect the narrowing of the FP modes due to the laser cavity gain.

known as the side mode suppression ratio (SMSR), is improved in the Y-laser structure, as shown in figure 3.4.

3.3 Other interferometric lasers

A combination of different types of interferometric lasers have also been designed. For the Y-laser it is possible to improve the SMSR by having a separate coarse and fine wavelength control in a cascaded Y-laser. Such a laser, called Y3-laser, was designed as illustrated in figure 3.5. The Y3-laser branches into three laser cavities from a common section,

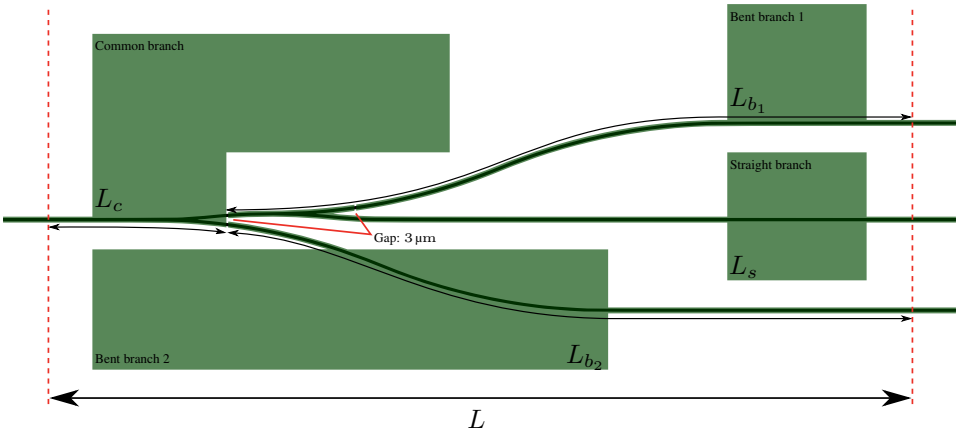

Figure 3.5: Illustration of the top-down design of the Y3-laser etch- (black), and corresponding metallization lithography pattern (green overlay). There are effectively three cavities with lengths $L_x = L_c + L_s \approx L$, $L_y = L_c + L_{b_1}$ and $L_z = L_c + L_{b_2}$. The laser structure can be viewed as forming, on roundtrip, two Mach-Zehnder interferometer filters. A fine filter is formed by the interference at Y-junction 2 (from left), which has a large length difference $(L_y - L_x)$, resulting in a small FSR. A course filter is formed by interference at Y-junction 1, which has a small length difference $(L_z - L_y)$ and therefore large FSR.

effectively creating two Y-laser interferometers. The interferometer with large FSR selects a particular wavelength region within the gain bandwidth, but does not provide sufficient discrimination between neighboring cavity modes. The second interferometer, which has a smaller FSR, then selects a particular cavity mode within the wavelength region selected by the first interferometer. An in depth analysis of the Y3-laser structure can be found in [13].

A V-coupled laser was also added to the combined interferometric laser pattern. The V-laser is essentially the same as the Y-laser, but has a shorter common branch length L_C. This improves the tuning lever of the device, slightly improving the tuning range of the device, but the drawback is a short common gain section.

The coupled-wave (CW) laser, consists of a straight FPL and S-bend laser in parallel, that is separated by a small gap g, as illustrated in figure 3.6. Due to overlap of the optical fields, the light in one waveguide can couple over into the other. The CW-laser can act as a 50-50 beamsplitter if the coupling length is selected as

$$L_C = \frac{\pi}{2\mathcal{C}} \tag{3.4}$$

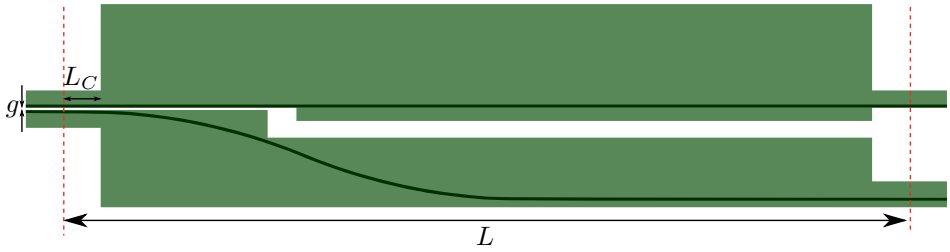

Figure 3.6: Illustration of the top-down design of the coupled wave (CW) laser etch- (black), and corresponding metallization lithography pattern (green overlay). The displayed CW-laser has a coupling gap $g = 5\,\mu\text{m}$ and coupling length $L_C = 50\,\mu\text{m}$.

where $\mathcal{C}$ is the coupling coefficient [7]. In that case, the CW-laser can be tuned similarly to the Y-laser. $\mathcal{C}$ is dependent on the coupling gap g, and was not known when the lasers were designed, so the coupling length L_C and gap g were set arbitrarily.

Y-laser Metal	Y-laser $w = 2.5\,\mu m$	Y-laser $w = 2.0\,\mu m$	Y-laser $w = 1.5\,\mu m$
Y-laser Metal	Y-laser $w = 2.5\,\mu m$	Y-laser $w = 2.0\,\mu m$	Y-laser $w = 1.5\,\mu m$
Combined 1 Metal CW/Y3/V	Combined 1 CW/Y3/V $w = 2.5\,\mu m$	Combined 1 CW/Y3/V $w = 2.5\,\mu m$	Combined 4 CV/Y3/V $w = 2.5\,\mu m$
Combined 2 Metal Y/V/CW/Y3	Combined 2 Y/V/CW/Y3 $w = 2.5\,\mu m$	Combined 2 Y/V/CW/Y3 $w = 2.5\,\mu m$	Combined 3 Y/V/CV/Y3 $w = 2.5\,\mu m$
S-bend Metal Straight x10 r300dL80 x10	S-bend w2.0 Straight x10 r300dL80 x10	S-bend w2.5 Straight x10 r300dL80 x10	Straight x20 $w = 25\,\mu m$
S-bend Metal r300dL100 x10 r500dl80 x10	S-bend w2.0 r300dL100 x10 r500dL80 x10	S-bend w2.5 r300dL100 x10 r500dL80 x10	Straight x20 $w = 50\,\mu m$
S-bend Metal r750dL50 x10 r1000dL20 x10	S-bend w2.0 r750dL50 x10 r1000dL20 x10	S-bend w2.5 r750dL50 x10 r1000dL20 x10	Straight x20 $w = 100\,\mu m$
Combined 3 Metal Y/V/CV/Y3 / Comb 4 Metal CV/Y3/V	Al Contact x20 $w = 25\,\mu m$ 40×50µm pad	Al Contact x20 $w = 25\,\mu m$ 100×100µm pad	DLTS

Figure 3.7: Schematic overview of the patterns included in mask 1. The patterns shaded in green are for metallization lithography, while the remaining patterns are for the waveguide etch. The size of the waveguide etch patterns were selected to fit with the typical sample size and can typically fit 20 lasers per row (i.e. per bar length L). Some patterns were duplicated for redundancy, in case of damage or manufacturing defects. All the waveguide etch patterns with waveguide width smaller than $25\,\mu m$ include the waveguide support structures along cleaving lines. Excerpts of some patterns can be found in appendix B.

Figure 3.8: Schematic overview of the patterns included in mask 1. The patterns shaded in green are for metallization lithography, while the remaining patterns are for the waveguide etch. The size of the waveguide etch patterns were selected to fit with the typical sample size. Some of the waveguide etch patterns are identical to those in mask 1, except that the support structures have been removed (e.g. the Y-laser patterns). For these patterns it was not necessary to redesign the metallization layer, as the existing patterns in mask 1 can be used. An error in the metallization pattern of the combined Y/V/CW/Y3 pattern was corrected and the pattern was therefore readded. The patterns with only S-bend lasers were redesigned to include two straight lasers in the middle of the pattern for reference, reducing the number of each S-bend to nine per row (i.e. per bar length L). Additionally, another pattern with a combination of all the S-bend (3 per row) and straight (2 per row) waveguides was designed. New metallization layers were included for these designs. Excerpts of some patterns can be found in appendix C.

Chapter 4

Processing of Laser Diodes

This section will explain the principles of semiconductor processing related to this work, the procedures used to fabricate the laser diode structures and the main findings regarding optimization of the final laser diode structure. The processing recipe is an iteration of the processing steps first deviced by M. Breivik for his PhD work on the topic of mid-IR lasers for gas sensing [8]. Each laser diode batch was fabricated at NTNU NanoLab over a period of 1 to 2 weeks. NTNU NanoLab is a multi-purpose micro and nano-fabrication facility with many users from different diciplines. Due to the broad usage of instruments, a lot of process variation can occur from one batch to another. During processing, most steps were first checked and investigated with a dummy sample to ensure compliance with the desired structure before moving on to process the laser samples.

In section 4.1, principles of semiconductor processing technology will be presented. Section 4.2 will describe the fabrication process used for the laser diodes in this work, and section 4.3 will present and discuss the main processing results. The full processing recipe can be found in appendix A.

4.1 Principles of semiconductor processing

Fabrication of laser diodes can be done with many of the same fabrication tools that are used for fabrication of microelectronic circuits. In this section, the main principles of

techniques and devices related to this work is presented. For a more comprehensive guide to semiconductor fabrication technology, see Quirk [14].

4.1.1 Photolithography

Photolithography is essential for most device processing. It is a process to transfer a predefined pattern on a mask onto the sample surface by using a material known as a photoresist (PR). The resist is usually deposited on the sample by spin-coater. In a spin-coater, the sample is mounted on a vacuum stage, a drop of the liquid PR is dispensed onto the sample surface, and the sample is then spun at high revolutions to reflow the resist into a uniform layer across the sample. After spin-coating, the sample is placed on a hot plate for soft-baking in order to evaporate remaining solvents in the resist, which improves adhesion and promotes resist uniformity.

When the PR is exposed to waves at a particular wavelength range (e.g. the i-line $365\,\mathrm{nm}$ UV light used in this work), the resist undergoes a photochemical reaction and becomes either soluble (positive PR) or insoluble (negative PR) in a chemical developer. The sample is placed in a mask aligner, where a photolithographic mask is aligned to the sample surface coated with PR, and exposed to the UV radiation. In positive lithography the pattern in the mask is transferred to the wafer, while in negative lithography the opposite of the pattern is transferred. A third type of resist, known as image-reversal resist, is a positive resist that can be reversed to function like a negative resist. After exposure, an additional image-reversal bake will passivate the exposed resist making it insoluble in developer and unaffected by any additional exposure. Performing a flood exposure after the image reversal bake, the remaining resist becomes soluble[15].

Edge-bead removal (EBR) is the removal of the resist near the edges of the sample. During the PR spin-coating, the resist is pulled off the sample by centrifugal forces creating a thin even layer spread over most of the sample. However, at the edges of the sample the PR accumulates into a bead. This is problematic for contact lithography, as the mask will be resting on top of the edge bead, creating a gap between the mask and PR at the center of the sample. Due to diffraction of light, the resolution is reduced, decreasing the sidewall profile angle. The sidewall profile of the resist is important for good etch profiles and metallization.

4.1.2 Dry Etching: ICP-RIE

Dry etching is a common process to reproduce the image of a mask on the wafer surface. Etchant gases are introduced to a chamber and dissociated by an electric field forming ions that can either chemically react with the wafer forming volatile products (chemical etching) or bombard the surface to sputter away atoms (physical etching). In inductively coupled plasma reactive ion etching (ICP-RIE), two RF power sources are used to independently control the ion density and energy in the plasma. In the ICP, an inductive coil decoupled from the chamber by a quartz plate is used to strike and control the density of the plasma. The RIE RF source powers two parallel electrodes, creating a self-biased negative potential on the cathode attracting the ionic species towards the sample. This provides both high etch rates and anisotropy to the etch, while limiting the effects of physical sputtering and thus increasing the attainable selectivity.

Etch rates, uniformity, selectivity and anisotropy are dependent on many parameters, including: ICP-RF power, RIE-RF power, chamber pressure, substrate temperature and gas flow rates. The etch selectivity is the ratio of the etch rate of a target material to the etch rate of the etch resistant mask (typically PR) and can be found experimentally by

$$s = \frac{r_t}{r_m} = \frac{d}{h_1 - H + d} \tag{4.1}$$

where h_1 is the mask thickness (PR thickness) before etching, d is the etch depth, $H = d + h_2$ is the etch depth plus the thickness of the remaining resist h_2. H and d can be found by measuring the height of the etched structure (e.g. by profilometer) before and after stripping the resist, respectively. The etch selectivity can be determined more accurately by scanning electron microscopy (SEM) imaging (without stripping the resist). However, this requires cleaving the device, limiting any further processing.

Another mechanism which can increase the anisotropy of the etch profile is polymer formation. During the directional etching, an etch-resistant polymer can deposit along the sidewall, thus preventing further lateral etching and increasing the etch anisotropy. The polymers are created from the carbon in the PR combining with the etch chemistry or volatile by-products. The side-wall profile of the etched material is typically similar to the profile of the PR mask. Optimizing the photolithographic process to achieve a near-vertical resist profile is therefore necessary for near-vertical etching.

4.1.3 E-beam evaporation

E-beam evaporation is a technique well suited for deposition of metals. The material to be deposited is placed in a crucible and heated by an electron beam. The e-beam gun typically sits beneath the target, and magnetic deflector coils are used to steer the electron beam towards the target. The mean free path of the evaporated molecules is increased by maintaining a high vacuum in the e-beam chamber, allowing the particles to travel in a straight line until it strikes a surface in the chamber. By keeping a sample in the line of sight of the target material, some of the evaporated material will get deposited on the sample surface. The high directionality of the vapor typically results in non-conformal step coverage, i.e. lower deposition rates on steep sidewalls and in high aspect ratio holes. This has led evaporation to become mostly replaced by other deposition techniques [14]. However, when patterning the metal using the lift-off technique, minimizing sidewall deposition is an advantage.

4.1.4 Lift-off

There are two main methods for patterning a deposited material. We can deposit the material first, then define the pattern by lithography and use an etch step to transfer a copy of the mask to the material. Another approach, called lift off, consists of doing the lithography step first, then depositing the material and using a solvent to remove any material that is not attached to the underlying substrate. If we want the pattern on the mask to be our final pattern in the deposited material, we must use a negative photolithography process.

Lift-off is a patterning technique that is particularly important for deposition of materials which does not create volatile products with any known etch chemistries. In order to etch such materials, we must use physical etching, which has poor etch selectivity and creates a rough surface[14]. In order for lift-off to create the desired pattern, we need to ensure that the resist sidewalls does not get coated in the metal deposition step. This will cause 'fencing' in the patterned layer or if the sidewalls are covered with enough metal, not allow the lift off to work at all. Having a pronounced undercut will avoid sidewall coverage. Undercut is defined by the lateral distance from the bottom edge of the resist to the top edge. The lift-off process is illustrated in figure 4.1.

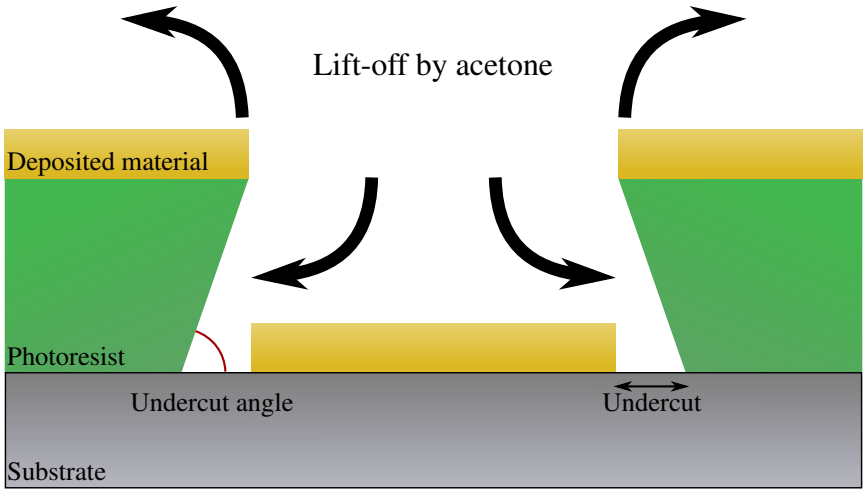

Figure 4.1: Illustration of the lift-off process. After depositing a material on the PR mask, acetone is introduced and starts attacking the resist. Deposited material that is not attached to the substrate is removed when the resist dissolves. An undercut resist profile improves the solvents access to dissolve the resist. The image-reversal resist is ideal for this purpose, since it acts as a positive resist during exposure, which typically leaves a sloped resist profile. After performing the reversal bake and flood exposure, the sloped profile becomes the desired undercut profile.

4.1.5 Characterization

Characterization of the shape, dimensions and defects of the processed structures is important to check for process variations as well as to optimize a given process. The structure of the device will influence its functionality.

Microscope is useful for low resolution imaging (diffraction limited to about $0.25\,\mu\mathrm{m}$[16]) to inspect the top surface of the sample during processing.

Scanning electron microscopy (SEM) is used for high resolution, high magnification imaging. An electron beam is scanned across the sample surface by magnetic scanning coils. Scattered electrons from the sample are detected and determine the contrast in the generated picture. Images in this work are taken by detecting secondary electrons, which only emits from the top surface layer (1–$2\,\mathrm{nm}$) of the sample and therefore gives good depth resolution and surface topography contrast[17]. The mechanism of SEM is illustrated in figure 4.2.

Profilometer measures the surface profile of the wafer by moving a needle across it. The needle detects small height differences as a function of the position across the surface of the wafer. The measurement can be destructive for small structures, since the needle applies a small force on the sample as it moves across the surface.

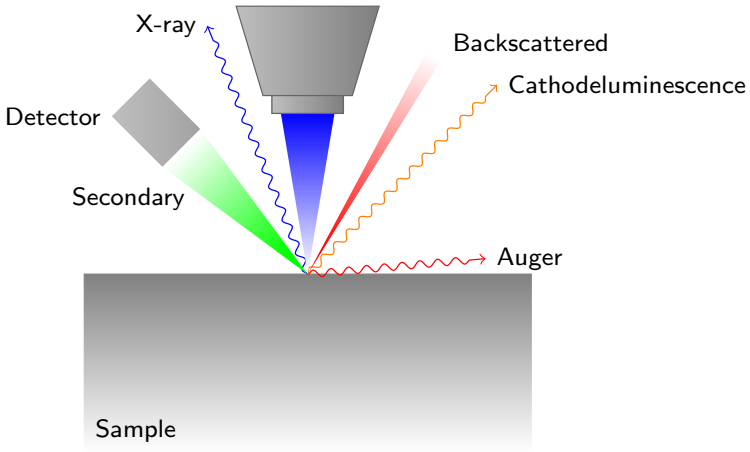

Figure 4.2: Schematic of the scanning electron microscopy. An electron beam is focused at a point on the sample and the resulting scattered electrons are measured by a detector. By doing this in a raster across the sample surface an image is formed, one pixel at a time.

4.2 Fabrication of mid-IR lasers

The lasers are fabricated as edge-emitting ridge-waveguide (RW) lasers using a GaSb-based MQW laser material structure, illustrated in figure 2.4. The laser diode growth has been described by Breivik [8]. The lasers were mostly fabricated on the laser material Sb158/Sb159, designed to lase at center wavelength $\lambda \approx 2.2\,\mu\mathrm{m}$, but some were also fabricated on Sb191, lasing at 2.3–2.4 µm. In this section the experimental procedure used for the laser processing will be described. Processing results and suggestions for improvement will be given in section 4.3.

Lasers have been processed with both deep-etch index guided (IG) RWs and shallow-etch quasi-index guided (QIG) RWs. The cross-sectional structure of the processed lasers can be seen in figure 4.3. For every laser batch, two or more samples were prepared for processing; one from the laser material (laser sample), one from a GaSb wafer (dummy sample) and in the case of the shallow-etch laser batches, a sample from a cladding wafer (cladding sample), which includes only the growth of the buffer, upper cladding and cap layer. The latter was used for endpoint detection during the RW etch. Laser batches were processed with S-bend waveguides of varying widths both with and without supporting structures (see chapter 3), and with interferometric waveguide designs like the Y-laser.

For the purpose of edge bead removal, a Si piece was cleaved to fit on top of the sam-

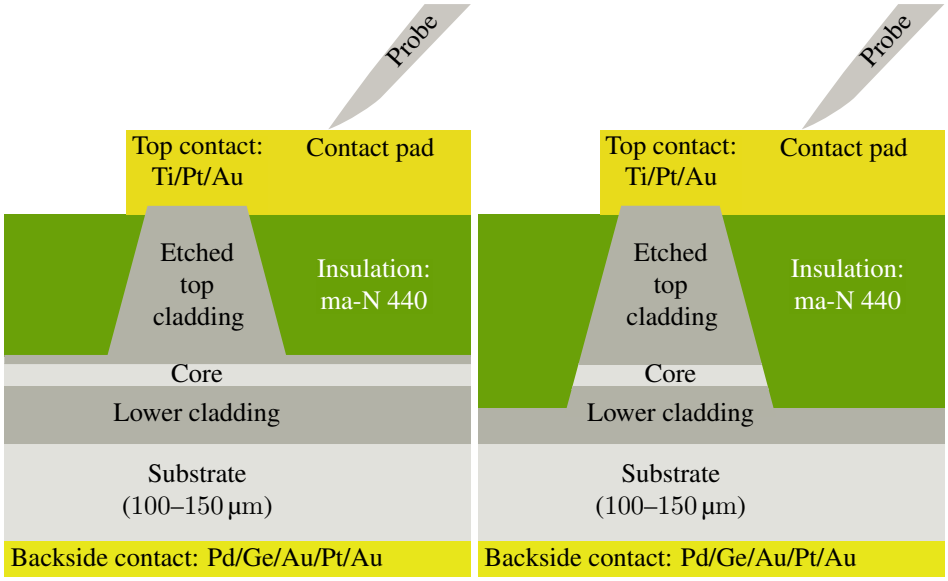

(a) Shallow-etch QIG-RW structure.

(b) Deep-etch IG-RW structure.

Figure 4.3: A cross sectional sketch of the processed lasers displaying the most important parts. The core consists of three GaInAsSb quantum wells separated by AlGaAsSb barriers for optical gain, as well as seperate confinement heterostructure for additional confinement of charge carriers. The purpose of the processing is to provide lateral confinement for charge carriers injected into the structure as well as for the optical field through index guiding. (a) For the shallowly-etched RW, lateral waveguiding is due to the effective refractive index contrast in the core layer, as a result of the etched top cladding[3]. The index contrast Δn_{eff} increases with etch depth into the upper cladding layer, improving the optical confinement[8]. Due to current spreading in the core, the active region volume can be larger than defined by the RW, so the carriers are only weakly confined. (b) For the deeply-etched RW, lateral confinement of the optical field is due to the relatively large refractive index contrast between the core material and the insulation layer. The carriers are fully confined to the active region by the etched RW.

ples leaving about $1\,\text{mm}$ of the sample edges exposed. All samples were cleaned using a standard acetone, ethanol and isopropanol (IPA) immersion for $5\,\text{min}$ and dehydrated at $150\,^{\circ}\text{C}$ on a hot plate for $10\,\text{min}$.

4.2.1 Ridge etch

The first part of the fabrication consists of defining the ridge-waveguide structure of the device. For the QIG-RW lasers it is desirable to etch as close to the core layer of the laser as possible to maximize the lateral effective refractive index contrast Δn_{eff} in the active region. This leads to an improvement of the index guiding characterstics of the waveg-

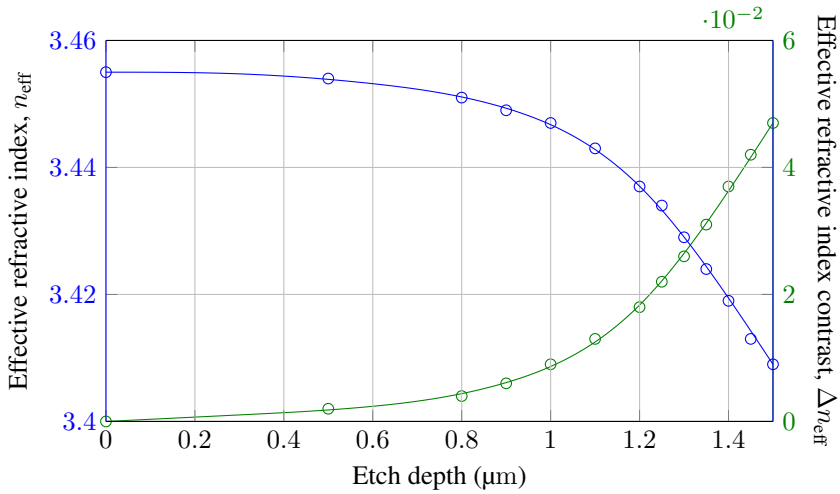

Figure 4.4: Simulated values for the effective refractive index n_{eff} versus etch depth, calculated by the infinite 1D slab waveguide approach, and the lateral effective refractive index contrast Δn_{eff} in the 2D etched waveguide[8, app. B]. Curves are fitted to the simulated data points. Δn_{eff} is the contrast between the unetched waveguide region and the etched region, i.e. $\Delta n_{\text{eff}}(d) = n_{\text{eff}}(0) - n_{\text{eff}}(d)$.

uide, which in turn decreases the guiding-loss. Minimizing the guiding-loss is particularly important for the curved waveguide structures. Simulations for the lateral effective refractive index contrast as a result of the etch depth into the upper cladding were performed by Breivik [8, app. B] and are plotted figure 4.4.

For the IG-RW lasers, the lasers were etched through the core and half-way into the lower cladding. This results in a considerable improvement in the index contrast which is now equal to the difference in effective refractive index between the core layer and the insulation layer. However, exposing the core can introduce unwanted effects in the long term, such as oxidation, which will degrade the laser performance over time. Additionally, the etch roughness in the sidewall of the active region introduces scattering loss.

For the ridge-etch lithography, image-reversal resist AZ5214E from Clariant [15] was used as a positive resist, and AZ 726 MIF as the developer base. The parameters used for spin-coating and exposure are listed in table 4.1. To remove the egde bead, the EBR Si piece was placed carefully on top of the sample and aligned such that the sample edge was uncovered. Flood exposure with a high exposure dose was then performed to ensure all of the edge bead would be removed in the developing process. The cleaved edges (which follows the $\{110\}$ planes for $\{100\}$ GaSb) of the sample were aligned to the horizontal

and/or vertical frame of the mask design (the support structures could also be used for alignment). Good alignment is necessary to get flat facet surfaces when cleaving the laser sample to minimize scattering loss in the resonator mirrors.

Table 4.1: Parameters for waveguide-etch lithography.

Parameter	Value
Spin coating	4000 RPM for $46\,\mathrm{s}$ (4000 RPM/s)
Soft bake	$110\,^{\circ}\mathrm{C}$ for $50\,\mathrm{s}$
EB exposure dose	$800\,\mathrm{mJ\,cm^{-2}}$
EB development time	$15\,\mathrm{s}$
Post EB bake	$95\,^{\circ}\mathrm{C}$ for $30\,\mathrm{s}$
Exposure dose	$150\,\mathrm{mJ\,cm^{-2}}$
Development time	20–30 s

The only variable parameter in the etch-lithography which was difficult to control was the development time. The sample is lowered into the development base and held there until the exposed resist appears to have been removed. The typical development time for a well developed ridge in the resist was $25\,\mathrm{s}$, but this could vary from batch-to-batch and even sample-to-sample in a given batch, even though the other parameters were kept the same. Inspection by microscope after the development was necessary to confirm a good profile. The profile was checked by slightly under- and overfocusing the top image of a waveguide and inspecting the change in thickness. For a well defined ridge with steep sidewalls, the change in thickness should be nearly unidentifiable.

End point detection by interferometry was used during etching, by applying a $675\,\mathrm{nm}$ laser mounted on top of the ICP-RIE etching system and monitoring the intensity of the reflected light from the sample, as illustrated in figure 4.5. Because of reflection at the interfaces between the different optical layers, it is expected to see a periodic signal during etching, as the reflected waves will interchange between constructive and destructive interference. For the simple case in figure 4.5, constructive interference of the reflected light from the first and second interface requires that

$$2n_1 d_N = N\lambda \tag{4.2}$$

and the etch depth per cycle of the reflected intensity is $d_{\text{per cycle}} = d_N - d_{N-1} = \lambda/2n_1$. If the refractive index (which is wavelength dependent) is unknown, $d_{\text{per cycle}}$ can be found experimentally by etching through a layer of known thickness d_{init} and dividing by the number of cycles in the corresponding reflected intensity plot. Assuming the etch rate is

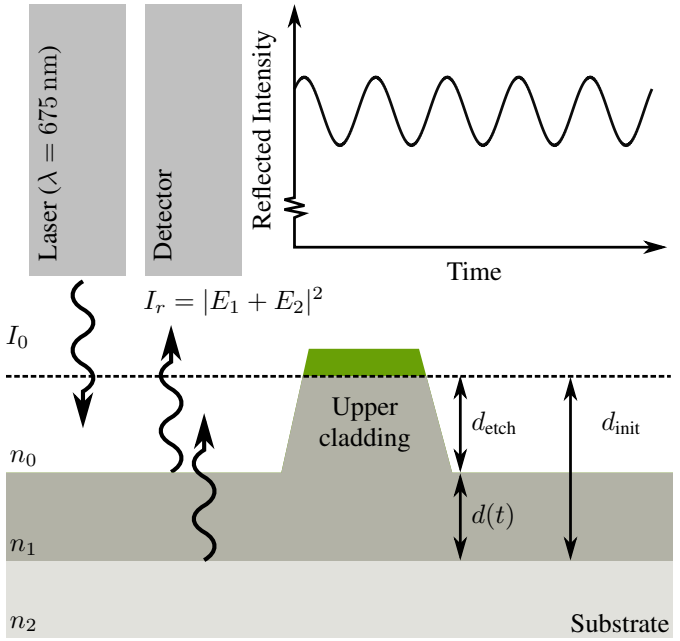

Figure 4.5: Schematic of the endpoint detection method used in the ICP-RIE.

constant throughout the etch, it can be found by $r_{\text{etch}} = d_{\text{per cycle}}/T$, where T is the wave period of the reflected signal.

The reflected signal from the lasers themselves can be difficult to interpret due to reflection from many optical layers[18]. For the shallow-etch lasers, a cladding sample with only the upper cladding and cap layer was used to monitor the etch depth. For the deep-etch lasers, the etch depth target is not critical, as long as the core has been etched through. However, a large etch depth complicates further processing, so the endpoint was selected as halfway through the lower cladding, determined as approximately ten cycles in the reflected signal. Since the lasers are etched through the core, the endpoint detection was done directly on the laser sample.

The chlorine based dry etching was performed with an Oxford Instruments Plasmalab System 100 ICP-RIE with cryogenic cooling. The etch parameters are summarized in table 4.2. After etching the laser sample, it was immediately put in a beaker of acetone for 30 minutes to remove the remaining resist on top of the ridges. Due to resist hardening during the etching process, it was necessary to use pressurized acetone from an acetone gun to completely remove the resist.

Table 4.2: Dry etching parameters and gas flows for the waveguide etch.

Parameter	Value
Ar	23.0 sccm
BCl_3	6.0 sccm
Pressure	4.0 mTorr
Strike Pressure	10.0 mTorr
RIE power	150 W
ICP power	1000 W
Temperature	60 °C

4.2.2 Passivation of the waveguide

The passivation (or insulation) layer is added to protect the ridge-structure both from chemical and mechanical damage. It must also prevent the top contact metal from contacting anything but the top of the laser ridge. The laser material should be coated with the passivation material immediately after etching to avoid the rapid oxidation of Al, Ga and Sb in the cladding- and core layer (the latter only for the deep-etch lasers), which will degrade the laser performance. The photoresist ma-N 440 from Micro Resist Technology was found to be a good choice for passivation material[8]. A thick layer of the resist is deposited by spin-coating and subsequently etched back to uncover the top of the ridges. The spin-speed was set relatively high (7000RPM for 30 s) to promote surface flatness. However, the resist was found to slightly follow the etched profile of the samples. This was particularly a problem around the supporting structures, complicating the etch-back process[10].

To increase thermal, chemical and mechanical stability, a passivation bake was performed on a ceramic hot plate. The samples were placed on the hot plate preheated to 100°. The temperature was then set to 160°, at which point the samples were left for 5 min, before again increasing the temperature to 260°. After 3 min, the samples were removed and cooled. Note that the hot plate temperatures were not well calibrated. EBR was not done by exposure and development prior to the passivation bake, as it was previously found that this results in bubbling [8], rendering the insulation layer useless. It was instead performed inside the ICP-RIE chamber using a 10 min fast rate O_2/CF_4 etch (see table 4.3), by masking the sample with the EBR Si piece. An Oxford Instruments Plasmalab System 100 ICP-RIE with water-cooling was used for the PR etching.

Without sacrificing the sample and investigating by SEM, there is no easy way to determine the etch depth necessary to uncover the top of the ridges. The PR etch-back therefore

Table 4.3: PR etch-back (slow rate) and EBR (fast rate) parameters used for PR etch-back.

Parameter	Slow rate	Fast rate
O_2	10.0 sccm	15.0 sccm
CF_4	2.0 mTorr	3.0 sccm
Pressure	3.0 mTorr	5.0 mTorr
RIE power	50 W	100 W
ICP power	100 W	200 W
Temperature	20 °C	20 °C

has to be carried out by trial and error, i.e. by etching for short amounts of time followed by inspection. Inspection by microscope reveals if the top of the waveguide is clean, at which point the profilometer can be used to determine if the sample has been overetched, exposing the ridge sidewalls. To minimize contact resistance, the top contact must be deposited on top of a clean cap layer, but should preferably not be in contact with exposed ridge sidewalls. Exposing the sidewalls have the additional undesirable effect of enabling sidewall oxidation, which further degrades the electrical performance of the device. If the resist is overetched, it is necessary to strip the resist and redo the process. However, because the small amounts of CF_4 in the gas mixture slightly attack the laser material, this will degrade the profile of the RW. To prevent this from happening to the lasers, the dummy sample was used to optimize the etch-time.

4.2.3 Top contact layer

The lift-off process was used to pattern the top contact metal layer. Lithography was performed according to the parameters summarized in table 4.4. To get a good undercut resist profile, the photoresist AZ5214E was used in image-reversal mode, which typically gives a 70–85° undercut angle (see figure 4.1). Figure 4.6 shows an excerpt of the metallization pattern and demonstrates how it was aligned to the etched structures. The alignment of the waveguide etch- and metallization layer can also be seen for some of the designed patterns in appendix B and C.

For metal deposition an AJA International Inc. Custom ATC-2200V was used in e-beam evaporation mode. The AJA have 6 installed e-beam pockets (Au, Ti, Pt, Ge, Pd and Si). The choice of metallization scheme for the top contact is Ti/Pt/Au (50/25/325nm), which forms a good ohmic contact with the top cap layer [19]. The Ti acts as an adhesion layer and Pt as a diffusion barrier for the top Au layer, which is easily contacted externally by probing and does not oxidize. Before depositing the metal, 16W Ar plasma sputtering was

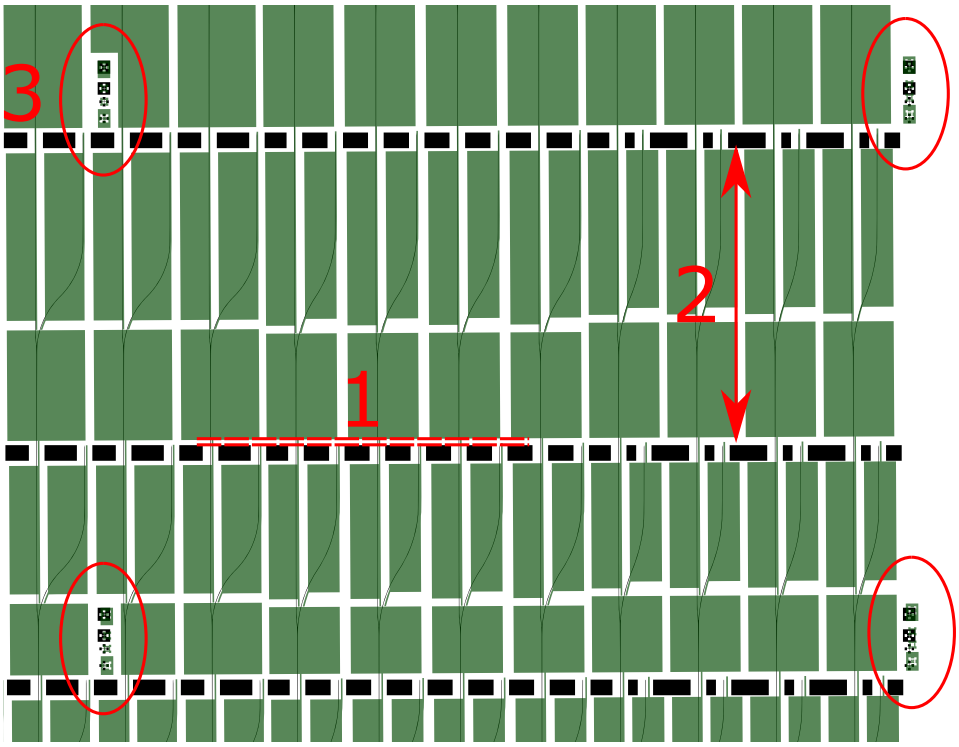

Figure 4.6: An excerpt of the top contact metallization mask (green) overlayed on the waveguide-etch mask (black) for the Y-laser pattern on mask 1 (the full pattern can be seen in appendix B. A misalignment between the two layers of $0.3°$ has been added to highlight the requirement of accurate alignment. Although the alignment can be seen to be good in the top left corner, the metallization layer is off mark in the bottom right. For quick and effective alignment the following procedure was used: **1:** the horizontal edges of the metallization mask was aligned parallel to the support structures for an initial rotational alignment. **2:** The length of the metallization pattern was aligned to match that of the waveguides. **3:** Two diagonal groups of alignment marks were used for the precise alignment, and a third to do a final check. Choosing alignment marks that are further apart, improves the alignment.

Table 4.4: Parameters for top-contact lithography.

Parameter	Value
Spin coating	4000 RPM for 46 s (4000 RPM/s)
Soft bake	110 °C for 50 s
EB exposure dose	800 mJ cm^{-2}
EB development time	25 s
Post EB bake	95 °C for 60 s
Exposure dose	18 mJ cm^{-2}
Image reversal bake	112 °C for 2 min
Flood exposure dose	200 mJ cm^{-2}
Development time	40 s

used in-situ for 1 min, to remove the native oxide on top of the RWs.

4.2.4 Lapping

The lapping station at NTNU NanoLab supporting lab was used to thin down the samples. The lapping process consists of using a grinding tool with a height-adjustable outer ring. The ring has high mechanical toughness and can withstand and stop the grinding at the desired height. Wax is melted on top of the centerpiece of the grinding tool and the sample is attached to the wax with the waveguide structure facing down. Additional wax is added around the sides of the sample to protect its edges during lapping. SiC paper from Struers was used for the grinding. The approximate thickness at the start is 500 µm and the target thickness is 100-150µm. For coarse (fast) grinding SiC 1000 paper was used. The SiC paper was soaked with de-ionized water during the grinding. The lapping was done in multiple steps, and approximately halfway the use of a finer SiC 2400 paper prevents build up of deep scratches in the sample backside, which could end up destroying the sample during the cleaving step. Once the sample thickness had been reduced to within 30 nm of the target, SiC 2400 was first used, then an even finer SiC 4000 together with colloidal silica suspension polish from Struers to get a smooth surface for the bottom contact deposition.

4.2.5 Bottom contact layer and annealing

After lapping, the samples are fragile and can easily break. Using a typical mounting technique, such as double sided adhesive tape or thermal paste, makes it difficult to remove the samples from the AJA sample holder without damaging them. To prevent this from

happening, the samples are 'glued' backside-up onto a 2 inch Si wafer using photoresist. The PR ma-N 440 serves the purpose, and spinning at 1000RPM for $30\,\mathrm{s}$ coats the wafer with a thick PR layer. The samples are mounted on the Si wafer which is then soft baked at $110\,^{\circ}\mathrm{C}$ for $10\,\mathrm{min}$ to promote adhesion.

For the back contact to the n-doped GaSb substrate, the metallization scheme Pd/Ge/Au/Pt/Au (8.7/56.0/23.3/47.6/200nm)[20] was chosen and deposited by e-beam evaporation. Before deposition, oxide removal was performed by Ar sputtering, in the same manner as for the top contact. To get an ohmic contact, the sample was annealed at $290\,^{\circ}\mathrm{C}$ for $45\,\mathrm{s}$[20] using a Jipelec Jetfirst $200\,\mathrm{mm}$ rapid thermal processing oven.

4.2.6 Scribing and cleaving

The zinc blende crystal structure of GaSb break along the $\{110\}$ planes. In this work $\{100\}$ wafers were used, so the samples could easily be cleaved into squares with atomically flat sidewalls. At the waveguide, these sidewall facets function as mirrors for the optical resonator. The quality of the cleaved facet must be excellent, or the lasers may be non-functioning due to the additional scattering loss in the mirrors. To promote a cleave along a specific line, a process known as scribe-and-tension was performed. First a scriber is used to create a small indent in the sample surface along the specific cleave-line. When applying force to the backside of the wafer, above the location of the indent, the tension will cause the sample to preferentially cleave along the $\{110\}$ planes starting from the indent location. The samples were edge-scribed, i.e. scribed only a small distance ($0.7\,\mathrm{mm}$ to $1.0\,\mathrm{mm}$) from the edge into the sample, since scribing across the RWs will damage the laser facets. It was previously found that the quality of the cleave was better with shorter cleave length[11], so the samples were also scribed and cleaved in two along the length of the cavities. The scribing was performed with a Dynatex DX-III Scriber.

After scribing the samples were put backside up on a thick layer of cleanroom wipes. A small cylinder shaped object was rolled carefully along the backside of the samples while gently applying force. Once the cylinder was rolled on top of a scribe-mark and enough force was applied the sample would cleave at the designated cleave-lines, creating bars consisting of approximately 10 laser cavities. For each bar, the cleaved sidewall was inspected by microscope to look for visual defects which would be detrimental to laser operation. Figure 4.7 illustrates the final inspection of the laser bars.

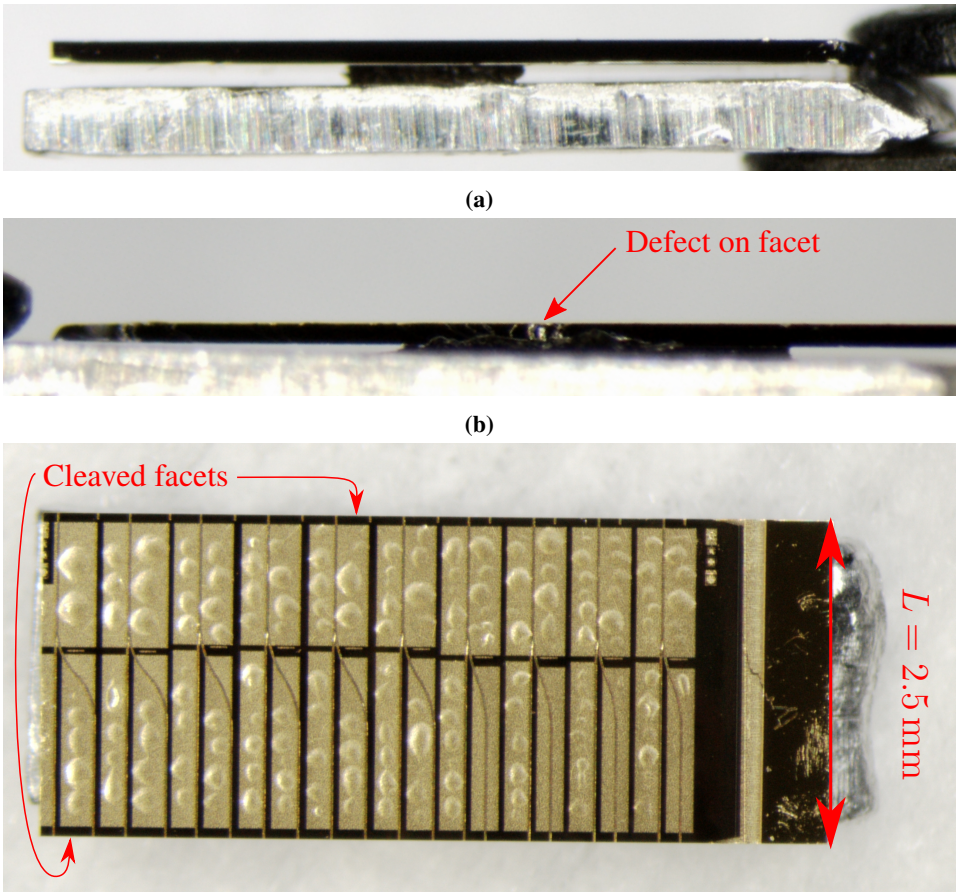

Figure 4.7: Microscope images of processed laser bars from laser batch LR7 and LR8. (a) After laser samples are cleaved into laser bars the sidewall facet is inspected for visual defects. Shown here is inspection of S-bend laser bar from laser batch LR8. The sidewall facet does not appear to contain any visible damage. The laser bar has been attached to a spacer for mounting into a cross-sectional holder in order to image the processed waveguide-structure with SEM. (b) Inspection of S-bend laser bar from laser batch LR7. This particular bar was miscleaved, and defects can be seen on the facet. Such defects indicate that the laser facets are broken. (c) Top inspection of the Y-lasers fabricated in batch LR8. The metal contact layer has a poor surface topography. After performing the metallization lithography the $3\,\mu\mathrm{m}$ separation between the metal contacts was found to be poorly defined. The sample was then stripped of the PR used for the lithography by immersing it in acetone. The acetone attacked the passivation resist and created a poor surface for consequent lithography and metallization.

4.3 Results and discussion

Several batches of lasers were processed using a variation of mask patterns. An overview of the processed lasers are given in table 4.5. Both S-bend and straight FP lasers as well as interferometric lasers, like the Y-laser were processed. Many laser batch runs ended with lasers which did not achieve lasing. In this section the major findings regarding optimization of the laser processing recipe will be presented.

The first two batches LR1 and LR2 were processed on Sb158 using an older mask which also included Z-bend lasers. It was found that the Z-bend lasers did not achieve lasing, and it was therefore decided to design a new mask excluding these designs to optimize the floor plan and thereby increase amount of lasers processed in each batch. The findings from the first batch LR1 have been discussed in [10], but will also be included here for comparison.

4.3.1 Ridge-etch

The thickness of the upper cladding in the laser material is $1.4\,\mu\mathrm{m}$. Furthermore, the cap and grading layer adds an additional $142\,\mathrm{nm}$. The target etch depth in the shallow-etch QIG-RW lasers is to get within $100\,\mathrm{nm}$ of the core layer, i.e. the etch depth should be in the range 1.44–$1.54\,\mu\mathrm{m}$. Figure 4.8 shows the endpoint detection data from a deep-etch laser. The number of cycles to etch through the upper cladding layer is approximately 14.5, such that etch depth per cycle can be calculated as $d_{\text{per cycle}} = 1.4\,\mu\mathrm{m}/14.5 \approx 97\,\mathrm{nm}$. If we want to etch to $50\,\mathrm{nm}$ above the core, the etch should be stopped about half a cycle before the core layer, i.e. 14 cycles into the upper cladding.

Endpoint detection data from several shallow-etch laser batches have been plotted in figure 4.11, together with corresponding SEM images of the respective lasers. For these lasers, the endpoint detection was done on a cladding sample, which based on an etch test showed a total of 15.5 cycles in the upper cladding. Although the composition of the upper layers in the cladding material is the same as those of the laser material, a small change in effective refractive index due to the additional optical layers in the lasers account for the change in $d_{\text{per cycle}}$. Initially, the endpoint was selected as 15 cycles into the upper cladding layer, which gave good etch depth results in LR1 S1 ($120\,\mathrm{nm}$ above the core). This etch strategy was continued for batches LR2–LR6, some of which obtained approximately the same etch depth, while others were considerably shallower (e.g. LR3 shown in figure 4.11 (c)-(d)). Upon closer inspection of the SEM images, it could be seen that the etch depth is

Table 4.5: Overview of the lasers processed in this work.

Laser batch	Sample	Material	Waveguide Pattern	Etch	Lasing / Comment
LR1	S1	Sb158	(old mask) w2.5 S-bend Combined	Shallow (1.42 µm)	Yes. Single-mode.
LR2	S1	Sb158	(old mask) w2.0 S-bend Combined	Shallow (1.37 µm)	No. Poor I-V.
LR3	S1	Sb158	(mask1) w2.0 S-bend r300dL100 & r500dL80	Shallow (1.24 µm)	No. Low Δn_{eff}. Good I-V.
	C1	Sb159	(mask1) w2.5 Combined 2 (Y/V/CW/Y3)	Shallow (1.09 µm)	No. Poor etch profile. Low Δn_{eff}.
LR4	S1	Sb159	(mask1) w2.5 Straight & S-bend r300dL80	Shallow (1.37 µm)	No. Poor I-V.
	Y1	Sb159	(mask1) w2.5 Y-laser	Shallow (1.31 µm)	No. Low Δn_{eff}.
LR6	S1	Sb159	(mask2) w25.0 S-bend r300dL100 & r500dL80	Shallow (1.32 µm)	Only straight lasers OK. Poor etch profile. Low Δn_{eff}. Good I-V.
	S2	Sb159	(mask2) w25.0 S-bend r300dL100 & r500dL80	Shallow (1.4 µm)	Only straight lasers OK. Good I-V.
LR7	S1	Sb159	(mask2) w25.0 S-bend r750dL50 & r1000dL20	Shallow (1.4 µm)	Yes, for r1000dL20 and straight lasers. r750dL50 lasers did not lase. Good I-V.
	S2	Sb159	(mask2) w25.0 S-bend r750dL50 & r1000dL20	Deep (2.55 µm)	Yes. Multi-mode. Good I-V.
	S3	Sb159	(mask2) w8.0 S-bend r750dL50 & r1000dL20	Deep (2.75 µm)	Yes. Multi-mode. Good I-V.
LR8	S1	Sb191	(mask2) w5.0 S-bend r300dL100 & r500dL80	Deep (2.68 µm)	No. Poor I-V.
	S2	Sb191	(mask2) w5.0 Straight & S-bend r300dL80	Deep (2.96 µm)	Yes. Single-mode. Low output power, poor I-V.
	S3	Sb191	(mask2) w5.0 S-bend r750dL50 & r1000dL20	Deep (2.89 µm)	No. Poor I-V.
	Y1	Sb191	(mask2) w5.0 Y-laser	Deep (2.84 µm)	Yes. Single-mode. Poor I-V and unstable contacts.

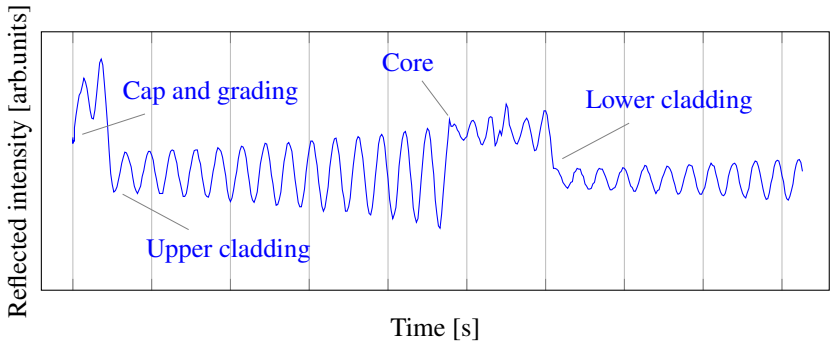

Figure 4.8: Endpoint detection data from the laser sample LR7 S3. This sample was etched into the lower cladding and illustrates the reflected intensity pattern in the lasers. The starting point of the different layers in the laser structure have been marked. Both the upper- and lower cladding exhibit nice periodic patterns that are easy to recognize. Typically for the laser samples, the upper cladding does not get a nice periodic pattern like this, because of the additional reflections from the lower optical layers[18]. Therefore, a cladding sample has been used in conjunction with the lasers for the shallow-etch lasers.

slightly shallower near the waveguides, which is well illustrated in figure 4.9.

The typical ICP-RIE sample mounting is sketched in figure 4.10. When aligning the endpoint detection laser spot to the sample, it is typically placed midway between two waveguides. The measured endpoint data is therefore an average measure of the etch depth inside the laser spot size which is relatively far from the waveguides. The measured etch depth is thus typically the etch depth in the bottom of the etch valley, which can be more than $100\,\mathrm{nm}$ deeper than near the waveguides. Avoiding exposure of the core layer is only important near the active region, where lasing will occur. Therefore, the shallow-etch lasers in batch LR7 were slightly overetched according to the endpoint detection data. The result from a test on the cladding sample can be seen in figure 4.9b and for the laser in figure 4.11f. The etch depth of the lasers in LR7 S1 were still $100\,\mathrm{nm}$ shallower than for the cladding test sample, even though both samples were over-etched for the same amount of time. This could either mean that ICP-RIE is experiencing loading effects due to the additional etch surface area, i.e. the etch rate is limited by the byproduct removal rate, or it could suggest that the etch rate is not uniform across the surface of the carrier stage. Upon further inspection of the etch depth of the cladding sample that was etched together with the laser sample (from which the endpoint detection in figure 4.11e stems), it was found to be consistently $1.48\,\mu\mathrm{m}$ across the sample, which is reasonably close to the test sample etch depth ($1.5\,\mu\mathrm{m}$). The finding strengthens the hypothesis that there are indeed some considerable etch non-uniformity across the carrier, which would particularly affect

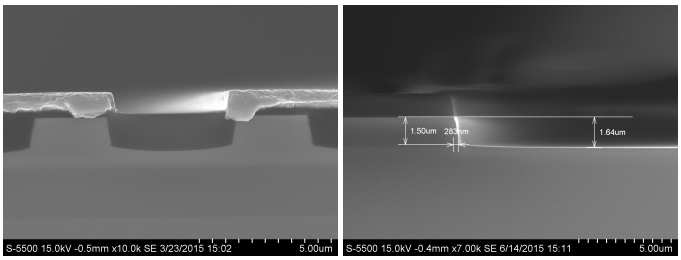

(a) **(b)**

Figure 4.9: SEM images revealing etch non-uniformity near the waveguide structures. (a) Facets of a CW-laser from sample LR3 C1. The etch valley between the waveguides is $220\,\mathrm{nm}$ deep. ((b)) Facet of cladding sample used in over-etch test before etching LR7 S1. This sample was delibarately over-etched for $11\,\mathrm{s}$ to optimize the etch-depth of the waveguides. The etch depth far away from the waveguide is $1.64\,\mu\mathrm{m}$, i.e. $100\,\mathrm{nm}$ beyond the target. However, near the waveguide the etch depth is $1.5\,\mu\mathrm{m}$, i.e. $40\,\mathrm{nm}$ above the maximum etch depth for the QIG-RW lasers.

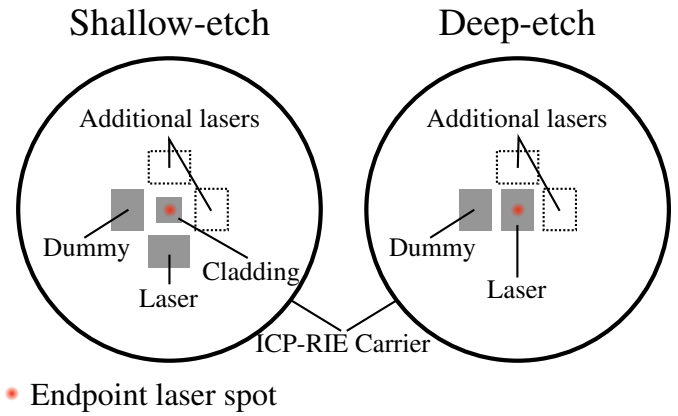

Figure 4.10: Top view sketch of sample mounting on a 4 inch Al_2O_3 wafer carrier for etching in ICP-RIE. The endpoint laser spot is centered on the ICP-RIE carrier. The spot size is about $25\,\mu\mathrm{m}$, considerably smaller than illustrated here, and can easily be aligned between two waveguides in the PR etch pattern by micro manipulators.

the laser batches where the lasers were not centered on the carrier stage.

Comparing the etch depths for the S-bend samples in LR8, which were all etched simultaneously, agrees with the observation of etch non-uniformity across the carrier, which in this particular batch is $\pm 5\%$ of the average etch depth. In order to get controllable and reproducible etch-depth, it is therefore necessary to etch each laser sample individually. However, the dummy sample can not be etched separately, so some etch depth difference between the dummy and laser sample must be expected. This will influence the PR etch-back.

Due to the need for overetching to get an appropriate etch depth for the RWs, the nice periodic pattern in the upper cladding is not needed, since the etch stop should be somewhere in the easily recognizable core pattern. A better approach for the shallow-etch lasers is then to exclude the cladding sample, and run the endpoint detection directly on the lasers. One laser sample was sacrificed to optimize the exact point in the endpoint detection data suitable for a target etch depth of $1.54\,\mu\mathrm{m}$. It was found that the etch-depth was controllable to within $\pm 10\,\mathrm{nm}$ using this method [11].

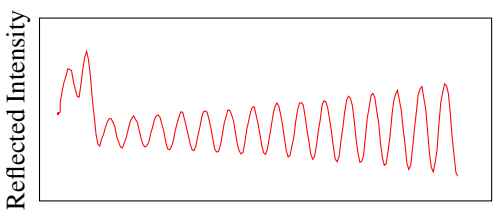

(a) Endpoint signal from etching sample LR1 S1.

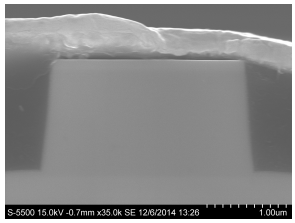

(b) Etch depth $= 1.42\,\mu\mathrm{m}$

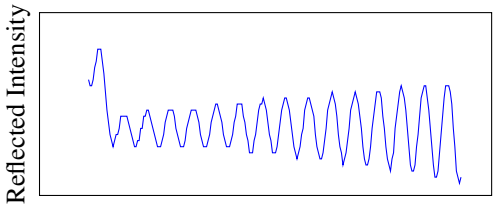

(c) Endpoint signal from etching sample LR3 S1 and C1.

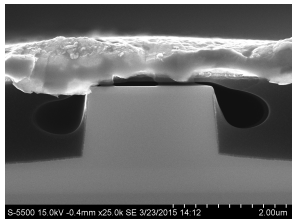

(d) Etch depth $= 1.24\,\mu\mathrm{m}$

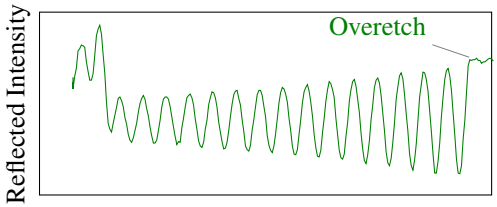

(e) Endpoint signal from etching sample LR7 S1.

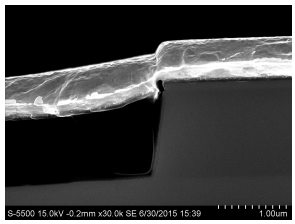

(f) Etch depth $= 1.40\,\mu\mathrm{m}$

Figure 4.11: Comparison of endpoint detection data and corresponding SEM images of shallow-etch lasers. For the shallow-etch lasers, the endpoint data was measured on the cladding sample. (a)-(b) The target endpoint was determined as 15 cycles in the upper cladding layer from etching through a cladding test sample. The etch was stopped exactly at target and the etch depth was found to be sufficient for lasing, although shallower than the expected $1.5\,\mu\mathrm{m}$. (c)-(d) The lasers in batch LR3 were etched exactly like the lasers from batch LR1, however the etch depth was found to be shallower. These lasers did not achieve lasing, likely due to a poor lateral waveguiding due to the low Δn_{eff}. (e)-(f) Before etching the shallow-etch sample in batch LR7, a cladding sample was deliberately overetched for $11\,\mathrm{s}$ to attempt to optimize the etch depth near the waveguides. The etch depth in the cladding sample was found to be $1.50\,\mu\mathrm{m}$, very close to the core. The same endpoint was used while etching the lasers, but nevertheless resulted in a shallower etch depth.

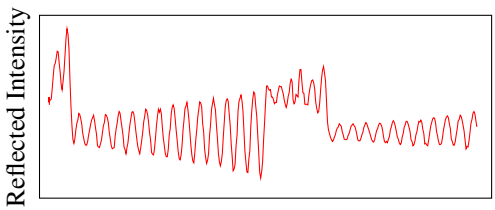

(a) Endpoint signal from etching sample LR7 S2.

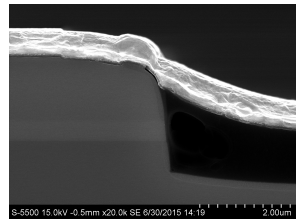

(b) Etch depth $= 2.55\,\mu\text{m}$

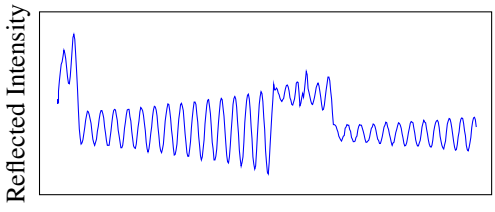

(c) Endpoint signal from etching sample LR7 S3.

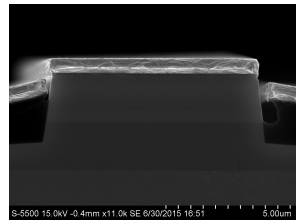

(d) Etch depth $= 2.75\,\mu\text{m}$

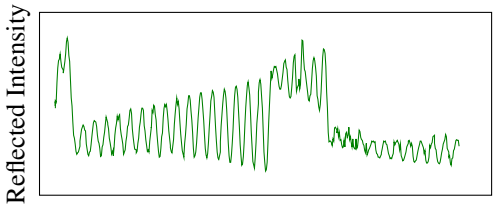

(e) Endpoint signal from etching sample LR8 S1, S2 and S3.

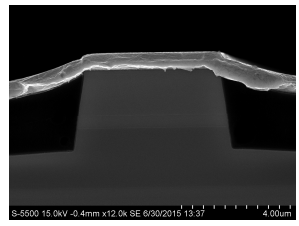

(f) Etch depth $= 2.96\,\mu\text{m}$

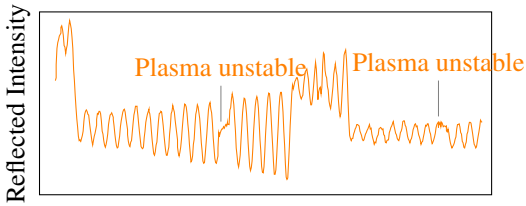

(g) Endpoint signal from etching sample LR8 Y.

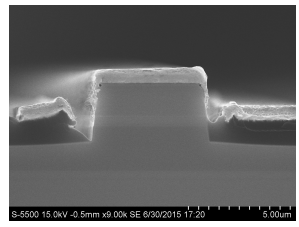

(h) Etch depth $= 2.84\,\mu\text{m}$

Figure 4.12: Comparison of endpoint data and corresponding SEM images of deep-etch lasers. The endpoint detection was measured directly on the lasers, however in some batches more than one laser sample was loaded in the chamber simultaneously. (a)-(b) The etch target was chosen as approximately halfway through the lower cladding (thickness $2.0\,\mu\text{m}$). Since the lower- and upper cladding have the same composition, the endpoint was determined at approximately 10 cycles. (c)-(d) The same endpoint as for sample LR7 S2 were used, but resulted in a deeper etch. (e)-(f) In batch LR8, the S-bend laser samples (S1–3) were etched together. The endpoint detection data was measured on S2, which was therefore centered on the ICP-RIE carrier and got the deepest etch depth. (g)-(h) During the etch of the Y-lasers in batch LR8, unstable plasma issues were encountered twice, causing the plasma to short such that the etch step had to be restarted. From inspection of the laser facets, this did not appear to affect the etch profile.

4.3.2 Passivation of the waveguide

When etching back the passivation layer, there is no easy way to determine that the top of the ridges have been uncovered. A typical inspection of the passivation etch-back process is shown in figure 4.13, together with a comparison of the profilometer and SEM measurement. The ething is done in consecutively shorter steps, in order to clean the top of the ridge, but minimize the sidewall exposure. The sidewall exposure can be measured non-destrutively by profilometer when the top of the ridge is clean. However, by comparing the profilometer plot with that of SEM images of the cross-sectional structure of the waveguide in figure 4.13g and 4.13h, the sidewall exposure appear to be two to three times larger in the profilometer measurement. On the other hand, the measurement can not be done in SEM for the laser samples because that would require cleaving the sample, limiting any further processing.

Getting the passivation layer right, has proved to be a major issue in the lasers processed for this work. In the laser batches LR1–LR4, lasers were fabricated on masks with structures placed along the cleave-lines of the laser waveguides, in near vicinity ($50\,\mu\mathrm{m}$, see figure 3.3) to the waveguide sidewalls. It has been found that these structures produce local topography difference for the deposited passivation layer[10]. Because of the additional passivation layer thickness on top of the waveguides in the vicinity of the supporting structures, it is not possible to uncover the entire length of the waveguide without risking exposure of the sidewall where the passivation layer is thinner (i.e. the middle section of the waveguides). For these lasers it was often decided to etch-back the passivation layer until most of the waveguide was clean. However, leaving resist on the top of the ridges has the negative effect of limiting the current injection into that part of the waveguide, which in turn will decrease the optical gain in the lasers. This phenomenon is illustrated in figure 4.14 for laser sample S1 from batch LR3. Since the lasers fabricated with support structures performed poorly (other than those from batch LR1), a new mask omitting them was designed.

In SEM inspection of laser facets, many lasers exhibited signs of disconnect of the metal layer across the waveguide, as can be seen in figure 4.15. At first, this was attributed to a poor PR etch-back, exposing a large part of the waveguide sidewall and creating a gap too large for the metal to deposit across. For this reason, it was decided to increase the thickness of the Au layer in the top contact from $325\,\mathrm{nm}$ to $650\,\mathrm{nm}$. However, additional problems observed in the SEM images, such as voids forming in the passivation layer around the waveguides as illustrated in figure 4.16, suggested that the issue lies in

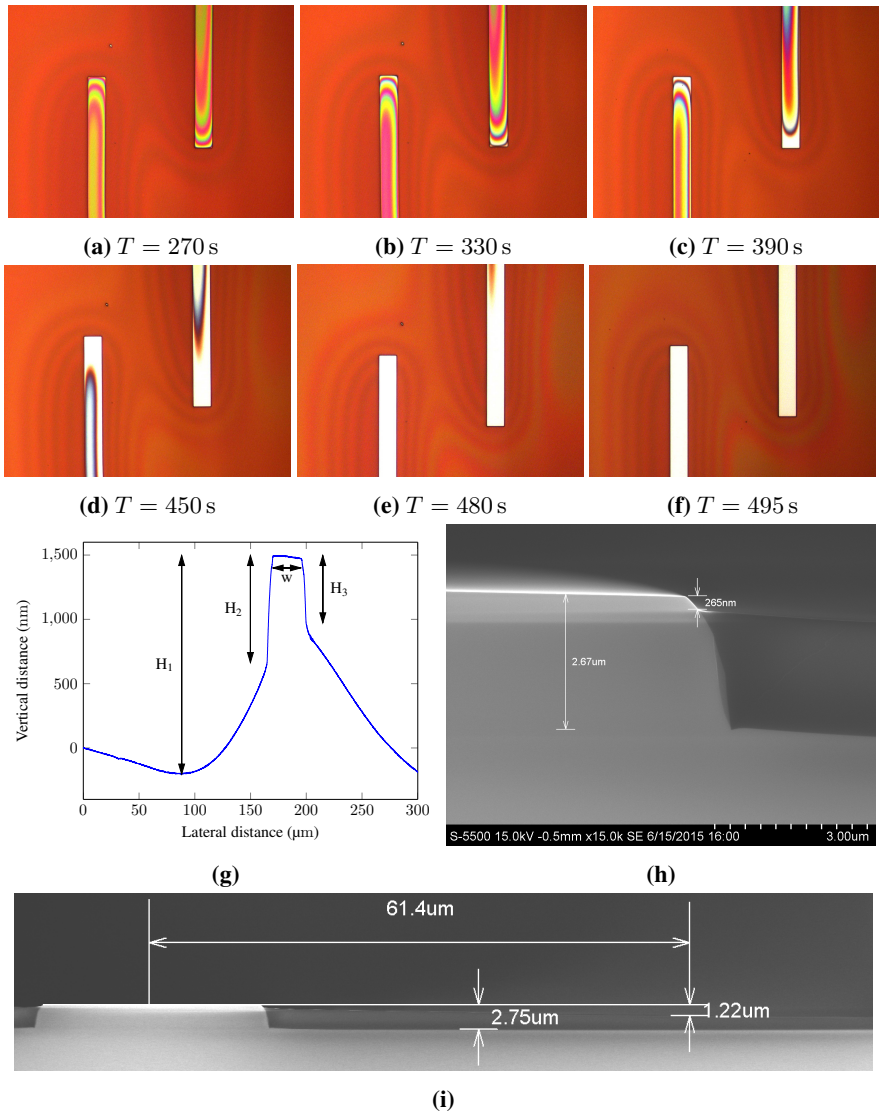

Figure 4.13: Demonstration of the PR etch-back experimental procedure of dummy sample in batch LR7 S2. (a)-(f) Microscope inspection of top of ridges after etch-time T. For each consecutive step, the etch time is shortened, until the ridge is clean. (g) Profilometer measurement across the clean waveguide. The values of the highlighted dimensions are: $H_1 = 1.7\,\mu\mathrm{m}$, $H_2 = 830\,\mathrm{nm}$, $H_3 = 520\,\mathrm{nm}$ and $w = 25\,\mu\mathrm{m}$. (h) High-magnification SEM image of the waveguide cross section reveals that only about $300\,\mathrm{nm}$ of the sidewall is exposed, far less than suggested by the profilometer measurement. (i) Low-magnification image of the same waveguide cross section highlights the sloped profile of the resist.

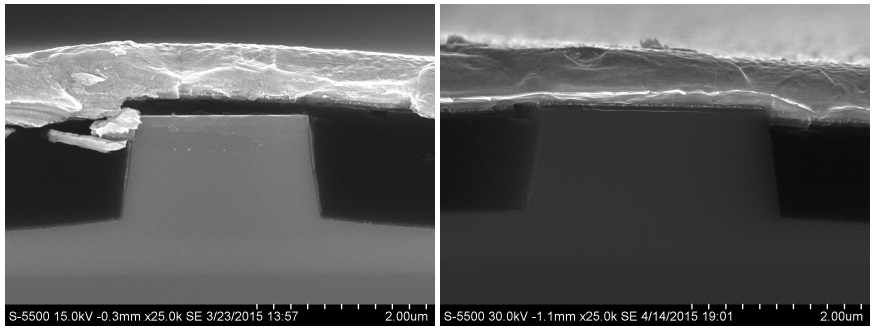

(a) **(b)**

Figure 4.14: Cross-sectional SEM images of sample LR3 S1, illustrating the non-uniform passivation layer due to support structures. (a) Image of the laser facet, i.e. at the end of the waveguide. A $200\,\mathrm{nm}$ layer of photoresist is sandwiched between the ridge and the top contact metal layer, prohibiting current injection into the laser. (b) Image of the same laser sample, but the laser has been cleaved across the middle of the cavity. Here the metal is in contact with the top of the ridge an the resist has been etched back enough to expose $150\,\mathrm{nm}$ of the sidewall. The difference in passivation layer thickness near the end of the lasers and in the middle of the lasers is about $350\,\mathrm{nm}$ due to the topography difference induced by the support structures.

a chemical instability in the passivation layer during the annealing step. The voids could be attributed to an outgasing process in the resist, where the gases can not escape due to the deposited top metal contact layer. One of the purposes of the passivation layer bake, is to prevent this from occurring, but the sample is exposed to larger temperatures in the annealing chamber ($290\,^{\circ}\mathrm{C}$ as opposed to $260\,^{\circ}\mathrm{C}$ on the hot plate). As mentioned in section 4.2.2, the real temperature on the hot plate during the passivation bake was not calibrated, so the actual temperature is likely much lower than the set temperature.

To further investigate the passivation layer profile after PR etch-back the dummy samples in batch LR7 were cleaved and inspected in SEM. A comparison between the passivation profile before (dummy) and after (laser) annealing is shown in figure 4.17. The height difference between the top of the RW and the top of the passivation layer is about $300\,\mathrm{nm}$ in figure 4.17a. In comparison, the height difference between the top of the metal contact on the ridge and the top of the metal contact on the passivation layer is about $900\,\mathrm{nm}$ in figure 4.17b. It is clear that the passivation layer both outgasses and shrinks during the annealing step. Due to the thermal expansion mismatch between the passivation layer and the top contact, the metal layer experiences compressive forces causing it to break from the contact layer adhered to the top of the ridge.

A new procedure was suggested involving doing an additional annealing step after the

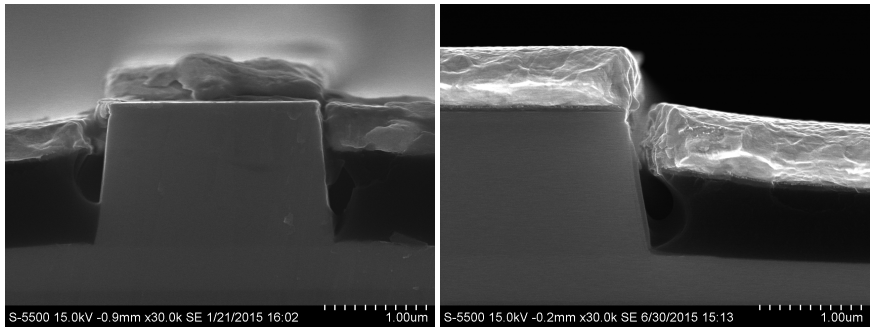

(a) **(b)**

Figure 4.15: Cross-sectional SEM images displaying the crack in the metal layer disconnecting the metal pad from the top of the waveguides, increasing resistance and reducing the carrier injection efficiency in the devices resulting in poor performance or non-lasing devices. (a) Sample LR2 S1. In this sample the disconnect was attributed to a poor PR etch-back, resulting in a too large gap for the metal contact to deposit across. The thickness of the Au layer is $325\,\mathrm{nm}$ in these lasers and was correspondingly increased to $650\,\mathrm{nm}$ in the processing of the subsequent lasers, to limit this issue. (b) Sample LR7 S1. Upon further inspection it appears that the passivation layer has been pulled back off the waveguide sidewall resulting in the disconnect of the metal layer.

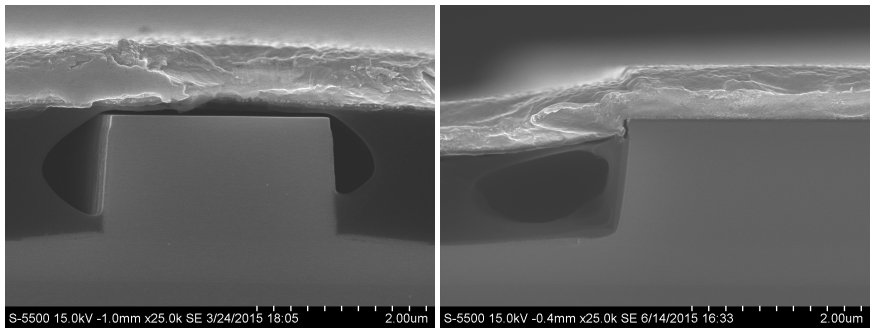

(a) **(b)**

Figure 4.16: Cross-sectional SEM images of laser samples illustrating the void formation in the passivation layer.

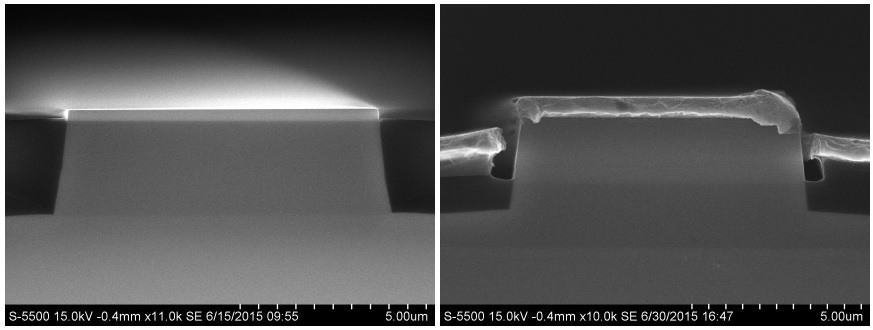

(a) **(b)**

Figure 4.17: Comparison of the passivation layer profile in batch LR7 S3 (a) before and (b) after undergoing the annealing process. The PR etch-back process was done comparibly for the dummy- and laser sample, shown in (a) and (b), respectively.

passivation bake, before doing the etch-back. This would ensure that the resist had already undergone the outgassing and shrinking, and could improve the final result for the lasers. A processing test including the additional annealing step was performed on a dummy sample and the results are shown in figure 4.18[11]. Due to time-constraint, no lasers were processed including this latest development of the processing recipe.

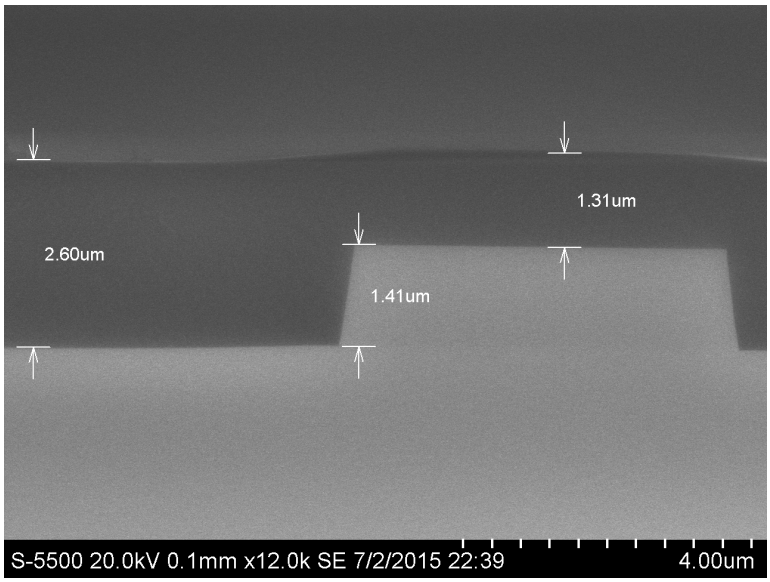

(a)

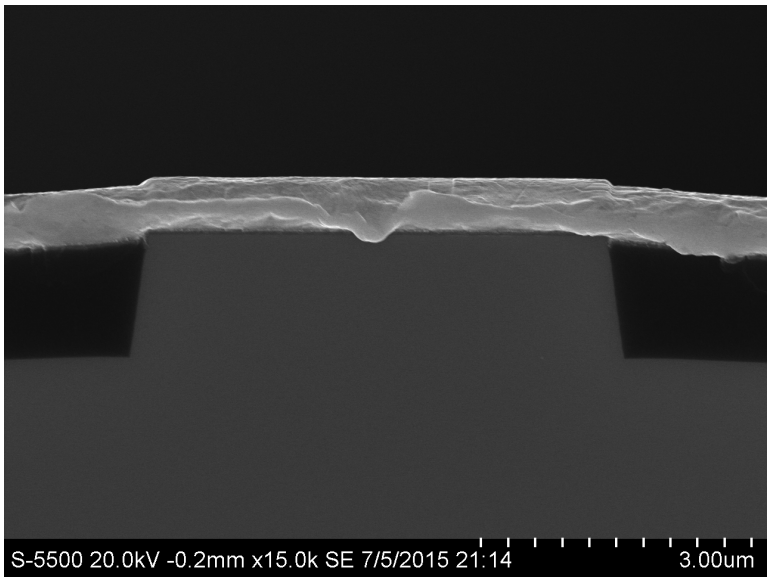

(b)

Figure 4.18: PR etch-back optimization. (a) Dummy sample after passivation resist coating and first anneal. No voids in the passivation layer can be seen, and the layer is reasonably uniform across the ridge. (b) Dummy sample after undergoing the remaining processing steps, including the PR etch-back, top metal contact deposition, lapping and second anneal. No voids are seen in the resist, the sidewall exposure is small and the metal layer is continuous. These results were seen for two dummy samples, suggesting that they are repeatable.

Chapter 5

Testing of Laser Diodes

In this chapter the laser testing theory, experimental setup and results will be presented. The focus will be on the S-bend laser diodes and the optimization of the curved laser structures.

5.1 Characterization of laser diodes

The light-output power vs. injected current (L-I) curve is an essential measurement for laser diodes. A typical L-I curve is shown in figure 5.1. To quantitatively assess the quality, performance and characteristics of lasers, a series of experiments can be performed to obtain the following significant parameters[21]:

Slope of L-I curve: The slope of the L-I curve measures the rate of change of output power per change of input current, which gives an indication of the energy conversion efficiency in the device.

Threshold current density: The current density necessary to produce stimulated emission in the laser. The threshold current can be found by investigating the curvature of the L-I plot. To find the current density, the area of current injection is needed. The shallow-etch lasers in this work have a buried active layer, in which the free carriers are only weakly confined in the lateral direction by the etched RW. Due to current spreading in the active region the actual width of the channel through which current is flowing is difficult to determine[3]. However, for simplicity the area was

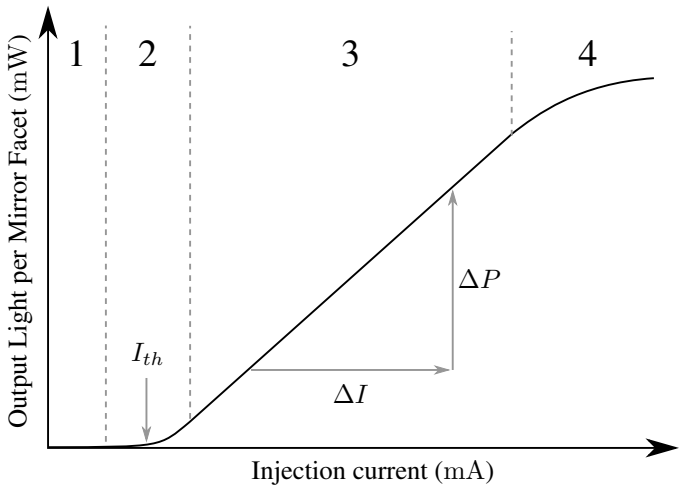

Figure 5.1: Illustration of a typical L-I curve: **1:** Off region. The injected carrier density is too small for population inversion, required for lasing. **2:** Turn-on region. Spontanous emission gradually increasing until the point where the injected carrier density reaches the threshold carrier density achieving population inversion. Stimulated emission processes start dominating. In this region we find the threshold current I_{th}. **3:** Linear region. Stimulated emission processes are dominating. From this region we can extract the slope of the L-I curve $\Delta P/\Delta I$. **4:** Saturation region. Injection of additional charge carriers is contributing mainly to non-radiative recombination mechanisms, resulting in heating of the device.

calculated by "Area = Waveguide Width×Cavity Length" and the threshold current values for the shallow-etch lasers are therefore slightly overestimated.

Transparency current density: The threshold current density of a theoretical device which has infinitely long cavity length and therefore no loss in the mirror facets. This parameter is independent of geometry and more useful in comparisons with other semiconductor lasers. It can be found by plotting the threshold current density against inverse cavity length. The vertical axis intercept of a linear fit line with these data points is the transparency current density.

External differential quantum efficiency (DQE): (η_d) is a figure of merit, usually measured in percentage, which indicates the efficiency of the laser diode in converting injected electron-hole pairs (input electric charges) to photons emitted from the device (output light). In an ideal laser diode, the recombination of each electron-hole pair results in the generation of one photon which survives the travel through the laser waveguide structure and is emitted from the device, contributing to the output light power. In a real laser, not every recombination event result in the generation of photons, but could result in the generation of other undesirable forms of energy, like heat. Additionally, some of the photons will get reabsorbed in the structure, or escape the waveguide along the cavity sidewalls.

Internal quantum efficiency (IQE): (η_i) is a parameter that measures the efficiency of a laser in converting electron-hole pairs into photons within the laser diode structure. In contrast to DQE this quantity is independent on geometrical properties of the laser device, such as the cavity length or the waveguide width, and therefore more useful for comparison with other laser diodes.

Internal loss (α_i) is the logarithmic loss pr. unit length for an optical wave propagating in the laser cavity. Especially the loss in the curved sections of the waveguides fabricated in this work is of interest.

Peak wavelength (λ) can be determined from spectrum measurements. Above threshold current, ridge-lasers with linewidths in the order of the emission wavelength are typically single-mode. This parameter is of particular interest in determining what gases may be analyzed by the TDLAS technique.

Side mode suppression ratio (SMSR) is the ratio between the strongest peak and the largest neighboring peak of the emission spectrum, usually given in logarithmic unit dB.

Turn-on voltage: The voltage at threshold current is a measure of the electrical diode performance of the device. A lower turn-on voltage generally means a reduction of ohmic losses resulting in generation of heat in the device.

Dynamic series resistance: Found by differentiating the V-I curve. Determines the quality of the metal contacts. Low values indicate ohmic behaviour.

A perfect hypothetical laser diode that converts a 100% of the injected current into photons emitting from the device (output light) without any form of loss would have $\eta_d = 100\%$. However, not all electron-hole pairs recombine to create light, and some of the photons are absorbed in the resonator before they are emitted. η_d is therefore dependent on the distance traveled inside the resonator, in other words dependent on the resonator length L. η_d can be found by comparing the slope of the L-I curve $(\Delta P/\Delta I)$ to that of a 100% efficient theoretical device $(hc/q\lambda)$ using (5.1)[21]. For a laser diode that emits equally from both cleaved mirror facets, a factor of 2 corresponds to the output light only being measured at one end.

$$\eta_d = 2\frac{\Delta P}{\Delta I}\left[\frac{q\lambda}{hc}\right] \tag{5.1}$$

In this equation $h = 6.63 \times 10^{-34}\,\mathrm{J\,s}$ is Planck's constant, $q = 1.60 \times 10^{-19}\,\mathrm{C}$ is the elemental charge, $c = 2.99 \times 10^{8}\,\mathrm{m\,s^{-1}}$ is the speed of light in vacuum and λ is the wavelength of emission.

Optical power loss calculation

For a straight laser diode, the total round trip optical loss can be described by (5.2) from where the total loss coefficient α_r can be derived, as in (5.3) [7], [22]. The loss coefficient α_r consists of the mirror loss coefficient α_m, given by (2.11) and α_i, representing all other internal losses due to scattering and absorption. $R_{(1,2)}$ are the power reflectance of the two Fabry-Perot laser (FPL) resonator mirrors and L the cavity length.

$$\exp(-2\alpha_r L) = R_1 R_2 \exp(-2\alpha_i L) \tag{5.2}$$

$$\alpha_r = \alpha_m + \alpha_i \tag{5.3}$$

The power lost in the mirrors represent the emitted light power. Consequently, it can be used to relate the DQE with the IQE of the device through (5.4) [22].

$$\eta_d = \frac{\alpha_m}{\alpha_r} \cdot \eta_i = \frac{\alpha_m}{\alpha_m + \alpha_i} \cdot \eta_i = \frac{\eta_i}{1 + \frac{\alpha_i}{\alpha_m}} \tag{5.4}$$

Taking the inverse of (5.4), we can find that there is a linear relationship between the

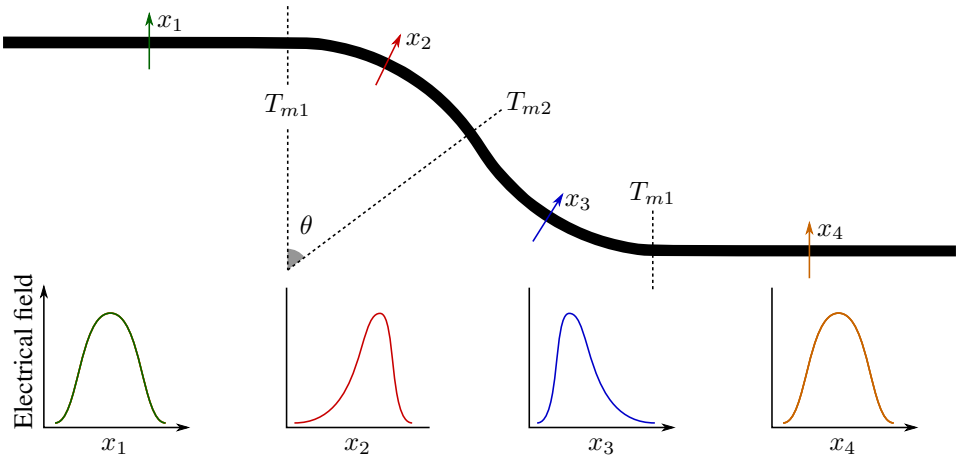

Figure 5.2: Sketch of the optical field in the different segments of the S-bend laser structure. In the curved segments the light circulates by reflecting at near grazing incidence, similarly to a whispering-gallery mode in a circular resonator[23], effectively skewing the shape of the electrical field towards the outer edge of the bend. The mode mismatch transition loss factor $T_{m1,2}$ represents the transition loss due to the optical field mismatch at the specified intersects. The skewing of the electrical field is inversely proportional to the bend radius r, thereby increasing the transition loss for smaller bend radi[22]. By visualizing the overlap between the modes it is clear that $T_{m2} > T_{m1}$. Note that the shape skewing of the optical field in the curved segments is here exaggerated.

inverse DQE and inverse IQE with respect to the cavity length L. When laser efficiency data is plotted according to the format of (5.5), the y-axis intercept gives $1/\eta_i$ and the internal loss α_i can be determined from analyzing the slope.

$$\frac{1}{\eta_d} = \frac{1}{\eta_i}\left(1 + \frac{2L \cdot \alpha_i}{\ln(1/R_1R_2)}\right) \tag{5.5}$$

A similar expression for the total roundtrip loss can be found for the S-bend laser in (5.6), adding a factor for the round trip loss $\exp(-4\theta \cdot \alpha_{\text{bend}})$ through the curved sections, where α_{bend} is the radiation bend loss coefficient (loss per radian) and θ is the arc angle of the curved segments shown in figure 5.2. The factor T_{m1}^4 represents the mode mismatch transition loss between straight and curved waveguide segments (4 passes per round-trip) and T_{m2}^2 the mode mismatch transition loss between oppositely curved waveguide segments (2 passes per round-trip)[22], as illustrated in figure 5.2.

$$\exp(-2\alpha_r L) = R_1R_2 \exp(-2\alpha_i L) \exp(-4\theta \cdot \alpha_{\text{bend}}) T_{m1}^4 T_{m2}^2 \tag{5.6}$$

Manipulating (5.6) similarly to the above derivation of the inverse DQE for the straight waveguide ends in (5.7). Comparing (5.7) with (5.5) it can be seen that the additional loss factors affects the intercept point of the characteristic inverse DQE plot. The new intercept term $1/\eta_i'$ is defined in (5.8).

$$\frac{1}{\eta_d} = \frac{1}{\eta_i'} + \frac{1}{\eta_i} \cdot \frac{2L \cdot \alpha_i}{\ln(1/R_1R_2)} \tag{5.7}$$

$$\frac{1}{\eta_i'} = \frac{1}{\eta_i}\left(1 + \frac{4\theta \cdot \alpha_{\text{bend}} + 4\ln\left(\frac{1}{T_{m1}}\right) + 2\ln\left(\frac{1}{T_{m2}}\right)}{\ln\left(1/R_1R_2\right)}\right) \tag{5.8}$$

5.2 Measurement setup

There are many parameters that can deduced from a few measurements of laser diodes. In this work, only some of the most common measurements have been done to illustrate that lasing operation is achievable for the devices. These measurements include: light-output vs. injection current (L-I), diode voltage vs. injection current (V-I) and spectral measurement using fourier transform infra-red spectroscopy (FTIR).

5.2.1 Measuring the L-I and I-V curves

The laser bars were mounted on top of copper plates using a colloidal silver glue. The backside of the copper plate was actively cooled by a Peltier element connected to a Newport Model 350B temperature controller set to $16\,^{\circ}\mathrm{C}$. The temperature was monitored by a thermistor element taped to the top of the copper plate. The top contact (anode) of the individual lasers were then probed using r-θ-z micro manipulators, and the back contact (cathode) was contacted externally through the copper plate. Although it was previously observed that collecting the emitted light by a collimating aspheric lens ($f = 1.8\,\mathrm{mm}$) could significantly increase the power readings [10], the additional alignment step involved made it unpractical for measuring a large amount of lasers. The addition of the collimating lens, did not appear to change the trends in the observed data, and therefore the light-output was measured by placing a Melles Griot Broadband Power Meter (model 13PEM001) directly in front of the lasers.

The measurement setup is illustrated in figure 5.3. The current was controlled with a Newport model 560 Laser Diode Driver and the voltage simultanously measured by multime-

ter. The current source was automatically controlled by an input voltage from a National Instruments NI9263 digital-to-analog converter (DAC) connected by USB to a PC. The DAC was set up to output voltage values from a list of voltages corresponding to the desired injection current (e.g. for Newport model 560 set up for $5\,\mathrm{A}$ range, $1\,\mathrm{V}$ input voltage corresponds to $500\,\mathrm{mA}$ output current), and to periodically switch to the next value in the list. Whenever the current source adjusted the current, multimeter and power meter readings were taken manually. The lasers were only tested in the continous wave (CW) regime, i.e. by injecting a non-modulated direct current.

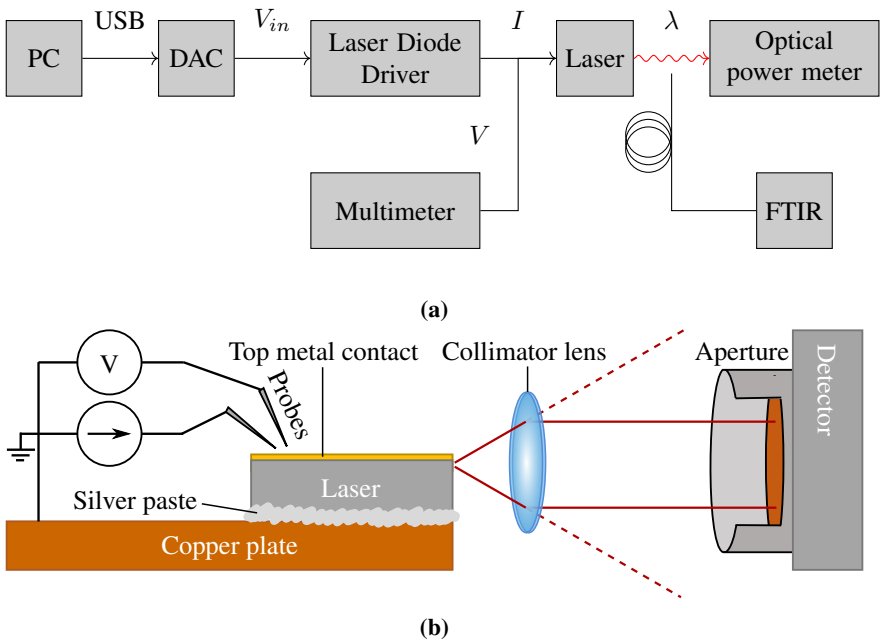

Figure 5.3: The test setup for measuring the L-I, V-I and spectral characteristics of the laser diodes. (a) Measurement setup connection diagram. The voltage output of NI9263 DAC was controlled by a PC and used as input for the laser diode driver to control the current injection I. The output power was measured by a power meter and the laser spectrum by coupling the laser light to a multimode fiber and guiding the light to the FTIR spectrometer. (b) Side view of the measurement setup. The laser bar is mounted on top of a copper sink using a colloidal silver glue. The top contact is connected to both a multimeter and the laser injection current source by probing. Due to a large beam divergence angle, ideally the optical power should be collected by a collimator lens. However, due to the additional alignment step involved in this, the detector was placed directly in front of the laser diodes.

5.2.2 Measuring the laser spectrum

For spectral measurements the laser light was coupled to a multimode fiber and guided to the FTIR spectrometer (see figure 5.3a) from Nicolet, located in the FTIR lab in the basement of IET at NTNU. The peak wavelength, side-mode suppression ratio, and full-width at half maximum (FWHM) are parameters of interest, withdrawn from this data. A comprehensive guide detailing the inner workings of FTIR spectroscopy is given by Smith [24].

5.3 Results and discussion

Characterization results for the fabricated laser batches will be presented here. The focus will be on the laser batches that achieved lasing action. In total 12 S-bend laser samples, 2 Y-laser samples and 1 combined interferometric laser sample were fabricated during 7 laser batch runs. In each laser sample there are typically about 12 laser bars, and for each bar there are up to 10 lasers. During the inspection of the cleaved laser bars, some have been found to be miscleaved, or have defects on the laser facets, in which case they were not tested as they presumably would not work well. All the lasers on one laser bar was assumed non-working if after testing three lasers on that particular bar, non achieved lasing action. Similarly all lasers on a sample were assumed non-working if after testing three laser bars, lasing was not achieved. The purpose of fabricating a large amount of S-bend lasers was to get good statistics in the optical loss calculations. In the fabrication of interferometric lasers, such as the Y-laser, the goal was to demonstrate the principle of laser wavelength tunability.

5.3.1 S-bend laser performance

An overview of the S-bend laser performance is given in table 5.1. Several interesting observations can be drawn from the table. For the shallow-etch laser batches (LR1–LR7 S1) it is necessary to etch close to the core (etch depth $1.542\,\mu\mathrm{m}$) to improve the lateral effective refractive index contrast Δn_{eff} to minimize the amount of laser light escaping the waveguide. For smaller bend radius this is increasingly important. In batch LR1, S-bend lasers with bend radi $(300,\ 500$ and $1000)\,\mu\mathrm{m}$ were lasing, even though these lasers exhibited an unusually poor diode characteristic. For lasers with good contacts, the typical

Table 5.1: Overview of the S-bend laser performance displaying which lasers achieved lasing. The turn-on voltage V_{on} is given when lasers achieved lasing. The maximum voltage were measured at the highest injected current, which varied from batch to batch, but was typically either $300\,\mathrm{mA}$ or $500\,\mathrm{mA}$. For lasers with a good diode performance, the slope of the V-I curve above the threshold current should be small, which is reflected in the maximum voltage. The contacts of the lasers in batch LR8 S1 and S3 were too unstable to measure the V-I characteristics.

Processing result			Lasing (✓) / Not lasing (✗)					Diode Performance	
Laser sample	Width (µm)	Etch depth (µm)	r300	r500	r750	r1000	straight	V_{on} (V)	V_{max} (V)
LR1 S1	2.5	1.41	✓	✓	-	✓	✓	1.0–1.9	1.6–2.1
LR2 S1	2.0	1.37	✗	✗	-	✗	✗	-	1.4
LR3 S1	2.0	1.24	✗	✗	-	-	-	-	1.2
LR4 S1	2.5	1.37	✗	-	-	-	✗	-	1.3–1.6
LR6 S1	27	1.32	✗	✗	-	-	✓	0.9–1.0	1.0–1.2
LR6 S2	25	1.40	✗	✗	-	-	✓	0.9	1.0–1.1
LR7 S1	25	1.40	-	-	✗	✓	✓	0.9	1.0
LR7 S2	30	2.55	-	-	✓	✓	✓	1.0	1.1
LR7 S3	8	2.75	-	-	✓	✓	-	1.1	1.2–1.4
LR8 S1	5	2.68	✗	✗	-	-	✗	-	-
LR8 S2	5	2.96	✓	-	-	-	✓	1.9–2.8	2.3–3.1
LR8 S3	5	2.89	-	-	-	✗	✗	-	-

V_{on} should be around 0.9–$1.0\,\mathrm{V}$ and the maximum voltage only slightly higher than this reflecting a very low dynamic diode resistance in the linear region.

Shallow-etch lasers: Etch-depth vs. lasing

Table 5.2 displays results for shallow-etch lasers extracted from table 5.1, sorted on the etch depth and including values for the lateral effective refractive index contrast from figure 4.4. As the etch depth increases, so does the index contrast, improving the lateral optical field confinement to the waveguide, allowing an increasing amount of the curved lasers to achieve lasing action. For sample LR3 S1, the etch depth was much shallower than anticipated (etching performed similarly to LR1 S1) and thus the S-bend lasers were not able to achieve lasing. In sample LR6 S1 and S2, the etch depth was improved, but still not deep enough to achieve lasing for S-bends with radius of curvature $(300$ and $500)\,\mu\mathrm{m}$. However, on the pattern used for these lasers, two straight waveguides were included (see figure C.2), in which the confinement requirements are not as strict, thus these lasers achieved lasing action.

Table 5.2: Overview of shallow-etch laser performance sorted by etch depth. Δn_{eff} values are from the fitted curve in figure 4.4. As the Δn_{eff} increases, the optical field confinement in the lateral direction is improved, thus reducing the optical loss in the curves. In order for the smaller radi S-bend waveguides to lase, index contrast exceeding 0.038 is needed, i.e. the remaining upper cladding thickness should be less than $130\,\text{nm}$. Using the optimized technique for controlling the etch depth, it should be possible to control the etch depth to within $\pm 10\,\text{nm}$ around the waveguides.

Processing result			Lasing (✓) / Not lasing (✗)				
Laser sample	Etch depth (μm)	Lateral Δn_{eff}	r300	r500	r750	r1000	straight
LR3 S1	1.24	0.021	✗	✗	-	-	-
LR6 S1	1.32	0.028	✗	✗	-	-	✓
LR6 S2	1.40	0.037	✗	✗	-	-	✓
LR7 S1	1.40	0.037	-	-	✗	✓	✓
LR1 S1	1.41	0.038	✓	✓	-	✓	✓

For sample LR7 S1 (which was intentionally slightly overetched), the etch depth was shallower than the anticipated $1.5\,\mu\text{m}$, but still achieved lasing action for the largest S-bend radius $1000\,\mu\text{m}$, but not for the smaller bend radius $750\,\mu\text{m}$. Sample LR1 S1 at $1.41\,\mu\text{m}$ etch depth achieved lasing for bend radi down to $300\,\mu\text{m}$. Comparing samples, LR6 S1, LR7 S1 and LR1 S1, the etch depth, and correspondingly Δn_{eff} is nearly identical, thus raising a question why the lasers with smaller bend radi in the prior two did not lase. In sample LR6 S2, SEM images showed a poor waveguide etch profile and correspondingly larger waveguide width of $27\,\mu\text{m}$, likely due to underdeveloped resist in the waveguide etch lithography. A near-vertical etch profile is necessary for good lateral confinement of both injected carriers and the optical field. Sample LR7 S1 also had a large waveguide width ($25\,\mu\text{m}$), but showed a good etch profile. However, the lasers in sample LR1 S1 were found to be single mode, due to the narrow waveguide width, which would not be the case for LR7 S1. Having a single-mode behaviour will increase the probability of the dominant mode to succeed in overcoming the optical losses in the curved section, since it will not experience as much competition for the available gain in the active region. A larger waveguide width will introduce higher order transversal modes that can spatially overlap with the dominant mode and compete for the available population inversion in those regions [7].

Comparisons of L-I and V-I curves.

Due to the large number of lasers fabricated in this work, the measured light output power- and diode voltage data was analyzed by a MATLAB program that is described in appendix

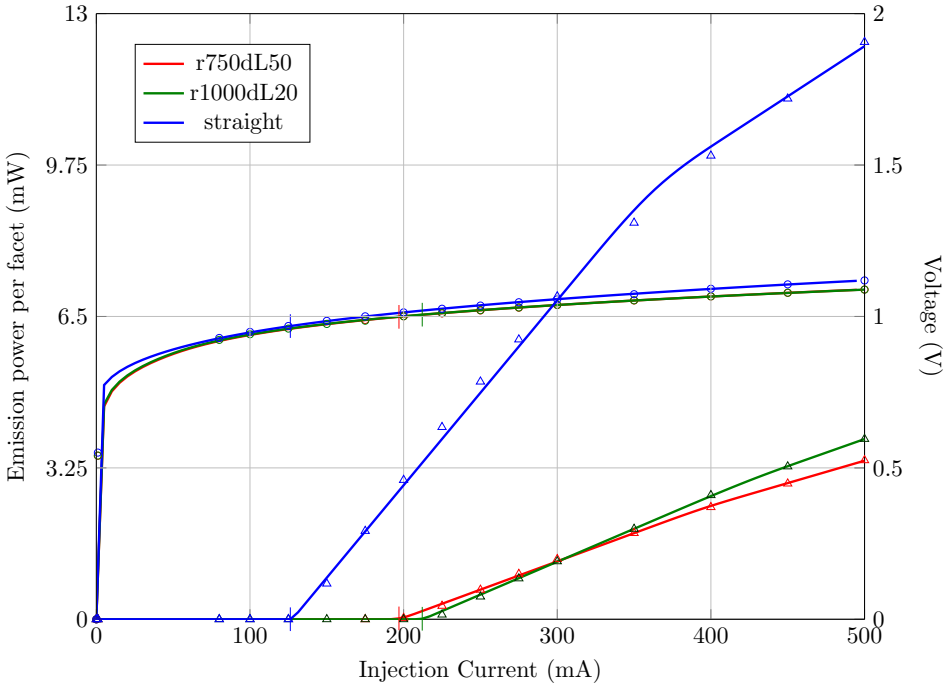

Figure 5.4: Comparison of L-I and V-I characteristics for different waveguides fabricated on sample LR7 S2 (deep-etch). The data is averaged over multiple lasers on bar with length $L = 1600\,\mu m$. The losses are substantially larger in the curved S-bend lasers, which can be seen from both the larger threshold current (marked by a vertical line) and the decreased slopes. The slope of the S-bend with radius $r = 1000\,\mu m$ are slightly larger than for the S-bends with $r = 750\,\mu m$, suggesting that the losses increase with reduction of bend radius as expected. The V-I curves of the lasers are overlapping and the diode performance is good for these lasers, indicating ohmic contacts.

D.

A comparison of the amount of light emitted as a function of diode injection current for the different types of waveguides in sample LR7 S2 can be seen in figure 5.4. The figure clearly shows a higher attainable optical power output from the straight FPL. Since these lasers were etched through the core, they are expected to have better waveguiding performance than the shallow-etch lasers, and the S-bend lasers should in theory perform similarly to the straight lasers. It is likely that the large additional losses in the S-bend lasers stem from sidewall scattering, as a result of the etch-roughness in the sidewalls, in contrast to the optical field leaking out of the waveguide in the shallow-etch lasers due to a small lateral refractive index contrast.

In figure 5.5, L-I and V-I curves for lasers with shallow- and deep-etched waveguide struc-

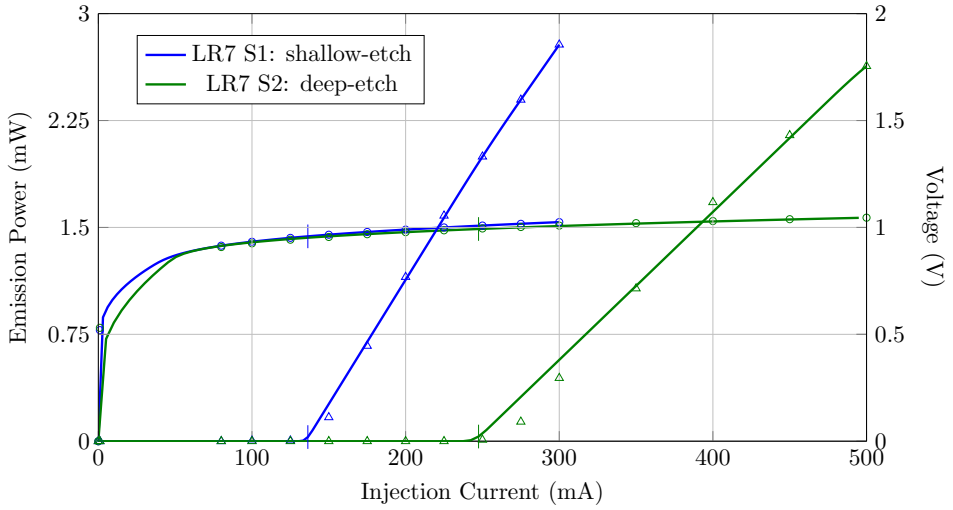

Figure 5.5: Comparison of L-I and V-I characteristics for shallow- and deep-etch r1000dL20 lasers in samples LR7 S1 and S2. The data is averaged over multiple lasers on bar with length $L = 1800\,\mu\text{m}$. Both lasers were fabricated with the same $25\,\mu\text{m}$ waveguide width pattern. The lasers in sample LR7 S1 were only tested up to $300\,\text{mA}$ injection current. The V-I curves are overlapping and lasers on both samples are exhibiting a good carrier injection characteristic. The shallow-etch lasers are performing much better than the deep-etch lasers at this bar length, as can be seen from the lower threshold current (marked by a vertical line) and the steeper slope in the linear region.

tures are compared. The shallow-etch lasers have improved lasing characteristics with a lower threshold current density and improved slope efficiency.

The L-I and V-I characteristics of lasers with different waveguide widths have been compared in figure 5.6 for laser samples S2 and S3 from batch LR7. The slope effiency appears to be improved in the narrower waveguide structures for the deep-etch laser. This trend could not be seen for the shallow-etch lasers, by comparing laser batch LR1 S1 with LR7 S1, however more data points are needed.

Threshold current density

Threshold current density values from the S-bend lasers are presented in table 5.3. The threshold current density is expected to be inversely proportional to the laser cavity length, and should therefore be seen to decrease with increasing bar length L. The overall behaviour of the different lasers display this trend. This can be seen by comparing the threshold current density of the shortest lasers with those of the longest lasers. All laser types from all samples exhibit this trend, except the lasers with bend r1000dL20 in sample LR7

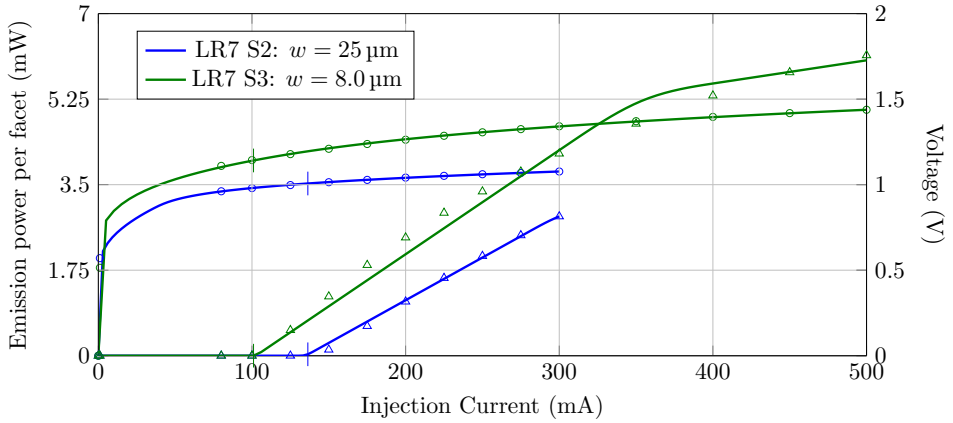

Figure 5.6: Comparison of L-I and V-I characteristics r1000dL20 lasers in samples LR7 S2 and S3 with waveguide width $8.0\,\mu m$ and $25.0\,\mu m$, respectively. The data is averaged over multiple laser on bar with length $L = 1000\,\mu m$. The lasers in sample LR7 S2 were only tested with injection current up to $300\,mA$. The diode characteristics for sample LR7 S3 appear to be worse than for sample LR7 S2, likely due to an increased problem with the passivation layer around the narrower waveguide. However, the slope efficiency for these lasers is larger than for the wider $25\,\mu m$ lasers, although the threshold density current is larger (due to the smaller waveguide area).

S2.

The threshold current density dependence on the cavity length is investigated in figure 5.7 for two selected laser types. The expected linear relationship between the threshold current density and the inverse of the cavity length is typically not clear, as illustrated in figure 5.7a. Only the data from bends r1000dL20 on sample LR7 S3 actually displayed a reasonable trend line, shown in figure 5.7b. It is not given that this exact relationship should be valid for the S-bend lasers, as it is derived for the straight FPL type lasers[21]. However, the relationship was not seen for the straight lasers either.

Quantum efficiency

External differential quantum efficiency was calculated from the slopes measured in the L-I data, as described by (5.1). The calculated DQE is presented in table 5.4. As presented in section 5.1, we expect the inverse DQE to be linearly increasing with the cavity length, which means we should see a decrease in DQE as the cavity length increases. It makes intuitive sense that the longer the wave propagates in the structure, the more optical loss it will experience due to scattering and absorption. However, this trend is not obvious in the data points in table 5.4. Again, the overall trend seems to suggest that the DQE is

Table 5.3: Threshold current density in the S-bend lasers. Each data point is an average value from lasers on that particular bar. Some laser bars did not demonstrate lasing action, typically due to a poorly cleaved mirror facet, and data points from these bars are omitted. The threshold current density is expected to be inversely proportional to the bar length L.

Processing result			Threshold current density ($\mathrm{A\,cm^{-2}}$)					
Laser sample	Bend	Width (μm)	L1000	L1200	L1400	L1600	L1800	L2000
LR1 S1	r300dL80	2.5	-	-	-	-	-	591
	r500dL80	2.5	1010	-	-	-	-	496
	r1000dL20	2.5	1802	-	-	-	-	846
	straight	2.5	-	-	-	-	-	538
LR6 S1	straight	25.0	-	271	289	-	337	222
LR6 S2	straight	25.0	-	-	242	212	236	212
LR7 S1	r1000dL20	25.0	-	-	382	-	289	316
	straight	25.0	-	-	-	-	229	-
LR7 S2	r750dL50	25.0	500	489	468	499	-	462
	r1000dL20	25.0	539	-	430	532	579	-
	straight	25.0	412	337	289	322	337	354
LR7 S3	r750dL50	8.0	1243	-	914	995	1032	1098
	r1000dL20	8.0	1279	1072	919	831	798	792
	straight	8.0	-	884	-	-	-	-
LR8 S2	r300dL80	5.0	-	3472	-	3427	2364	3059
	straight	5.0	-	-	-	-	1459	-

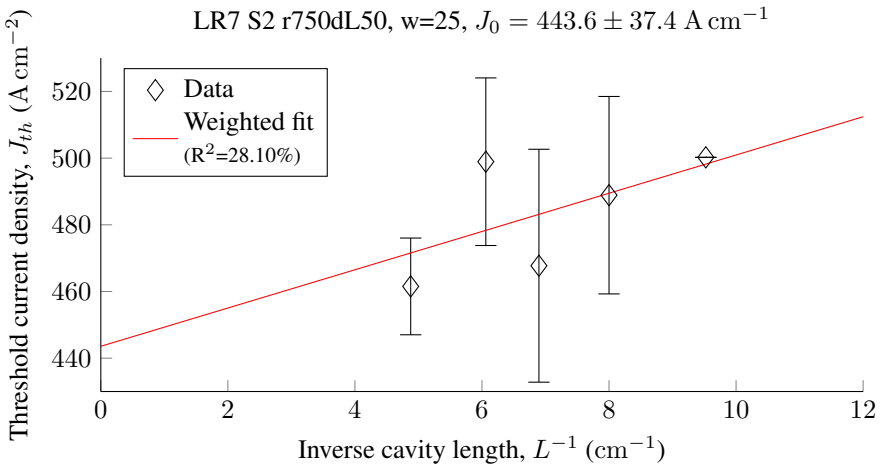

(a)

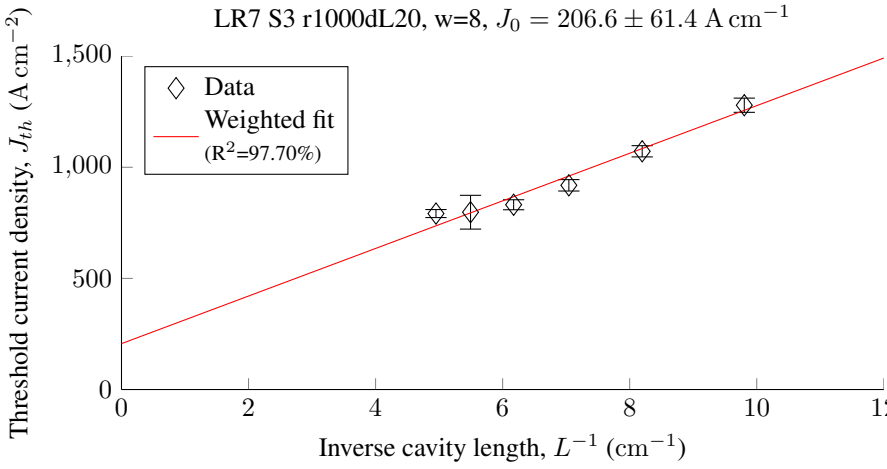

(b)

Figure 5.7: Threshold current density plotted against inverse cavity length for selected lasers. The length of the error bars represent the standard deviation in the measurement. The average values are fitted using a weighted linear fit algorithm, where the weight was selected as the number of lasers measured in each data point. The transparency current density J_0, based on the intercept point of the linear regression line, is given in the title, and the goodness of fit, expressed by the R^2 factor, is displayed in the legend. (a) Example of a typical plot. The overall trend appears to be increasing as expected, however the data points do not line up well with the linear fit. Considering the standard deviation, all data points are within one standard devation of the linear fit line. However, due to the poor fit, the model does not explain the data well, and the calculated J_0 should not be considered a good estimate. (b) Example of a plot with good fit. The data points appear to be following a linear trend, thus the estimate of J_0 is reasonable. However, due to the fact that the predicted value is relatively far from the data points measured, the standard deviation is large.

decreasing, by considering the DQE for the shortest cavity length vs. the longest cavity length. However, the trend is not monotonically decreasing.

By fitting the data according to the format of (5.5) we can find the IQE in the straight lasers and use this to estimate the additional loss factor represented in the upwards shift of the intercept point in the data from the S-bends, according to (5.8). Some results of using this procedure for the measured DQE is demonstrated in figure 5.8. The data does not appear to follow the expected linear trend, and the goodness of fit, represented by the R^2, is quite low, and thus the predicted intercept points giving the inverse IQE are not well estimated. Additionally, the slope of the linear fit lines are not equal for the straight and S-bend lasers, as suggested by (5.5) and (5.7). Without better estimates of the intercept points and slope of the linear fit, the loss in the curved sections can not be calculated. A recurring pattern in the dependence of the DQE on the cavity length is not evident from the data in table 5.4, thus attempting to fit it with a different model has not been done. The most likely reason for the varying behaviour of the lasers is the chemically unstable passivation layer, which causes the metal layer crack along parts of the waveguides, such that the carrier injection is non-uniform along the cavity of one laser, and non-uniform from one laser to another. This explains the highly varying performance of the lasers on the same laser bar.

Spectrum measurement

Laser spectra is plotted in figure 5.9. Lasers have been fabricated that lase around center wavelength $2.2\,\mu\mathrm{m}$ and $2.4\,\mu\mathrm{m}$, i.e. in the atmospheric window suitable for gas detection (see figure 1.2). Side-mode suppression ratio is presented in table 5.5. A comparison of the laser spectra from laser diodes with different waveguide widths is shown in figure 5.10. For use in TDLAS, it is a requirement that the lasers are single-mode, which occur for these lasers at a waveguide width $w \leq 5.0\,\mu\mathrm{m}$. For the single-mode lasers, the FPL structures achieve a SMSR of about $13\,\mathrm{dB}$. However, in some of the lasers, the largest side mode was not the neighboring mode. These modes may be caused by interference fringes from FP etalons in the fiber optic setup used[10], [25]. Additionally, for some lasers, only a small fraction of the light could actually be guided to the FTIR spectrometer. The noise floor for these lasers is relatively high, compared to the lasers where a high intensity could be guided through the fiber, which can affect the measured side-mode suppression ratio. A more suitable test setup will require the use of a single-mode fiber, however, this puts even larger requirements on the alignment, and the current setup in the laboratory is not well suited for this. Another approach is to mount the lasers directly in the FTIR stage, however this requires that the lasers are wire-bonded, rather than probed. Due to deposition of

Table 5.4: External differential quantum efficiency (DQE) in the S-bend lasers. Each data point is an average value from lasers on that particular bar. Some laser bars did not demonstrate lasing action, typically due to a poorly cleaved mirror facet, and data points from these bars are omitted. Note that there was considerable standard deviation in the DQE for many of the laser bars that is not reflected here, but illustrated in the inverse DQE plots. This large deviation likely stems from the issue with the passivation layer stability during the back-contact annealing (see section 4.3). The DQE is expected to be inversely proportional to the bar length L.

Processing result			External differential quantum efficiency (DQE) (%)					
Laser sample	Type	Width (μm)	L1000	L1200	L1400	L1600	L1800	L2000
LR1 S1	r300dL80	2.5	-	-	-	-	-	6.12
	r500dL80	2.5	3.81	-	-	-	-	7.37
	r1000dL20	2.5	3.53	-	-	-	-	3.88
	straight	2.5	-	-	-	-	-	10.27
LR6 S1	straight	25.0	-	11.52	13.96	-	11.04	9.11
LR6 S2	straight	25.0	-	-	12.89	13.64	9.95	11.2
LR7 S1	r1000dL20	25.0	-	-	5.26	-	6.28	4.95
	straight	25.0	-	-	-	-	12.56	-
LR7 S2	r750dL50	25.0	5.76	6.38	5.73	4.57	-	5.65
	r1000dL20	25.0	6.43	-	6.45	5.19	4.41	-
	straight	25.0	15.23	19.00	16.56	14.38	12.74	13.46
LR7 S3	r750dL50	8.0	5.95	-	6.18	5.2	6.1	3.74
	r1000dL20	8.0	7.71	6.88	7.29	6.34	6.86	7.62
	straight	8.0	-	5.16	-	-	-	-
LR8 S2	r300dL80	5.0	-	3.04	-	2.42	3.04	2.99
	straight	5.0	-	-	-	-	5.42	-

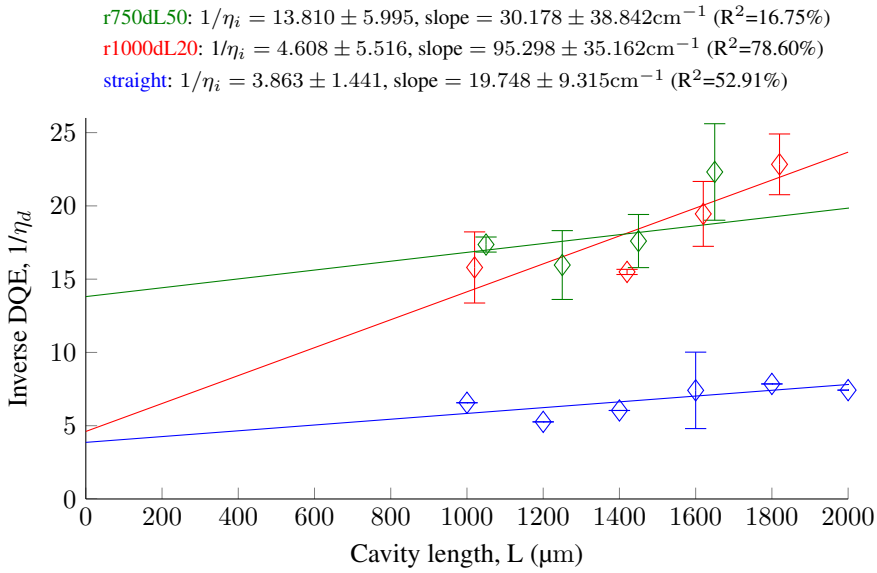

Figure 5.8: Inverse external differential quantum efficiency plotted against cavity length for lasers in sample LR7 S2. The length of the error bars represent the standard deviation in the measurement. The average values are fitted using a weighted linear fit algorithm, where the weight was selected as the number of lasers measured in each data point. The inverse IQE η_i and slope, based on the coefficients of the linear fit, is given in the title. The goodness of fit, expressed by the R^2 factor, is also displayed in the title.

Table 5.5: Extracted parameters from spectral measurements of lasers: The dominant lasing mode wavelength λ, the FWHM (σ) and the side mode suppression ratio (SMSR) of the largest side mode, marked by a red circle in figure 5.9.

Laser sample	Type	Width (µm)	Length (mm)	λ (nm)	FWHM (pm)	SMSR (dB)
LR1 S1	r1000dL20	2.5	2.0	2157.5	43.7	13.4
LR1 S1	straight	2.5	2.0	2178.9	58.6	14.2
LR7 S3	r1000dL20	8.0	1.4	2285.3	92.3	0.6
LR8 S2	straight	5.0	1.8	2396.1	71.9	13.0

the top-metal contact on a relatively soft passivation layer (passivated photo resist), wire-bonding the lasers to the contact pads can be difficult, and is another processing step which can introduce process variation.

5.3.2 Y-laser

Two Y-laser samples (LR4 Y1 and LR8 Y1) and one combined interferometric sample (LR3 C1) was fabricated. The lasers on LR3 C1 and LR4 Y1 did not achieve lasing, likely due to the very shallow etch depth, $(1.09 \text{ and } 1.31)\,\mu\text{m}$, respectively. In laser batch LR8 Y1, the resist from the metallization lithography was stripped with acetone once, because the small $3\,\mu\text{m}$ gap between the contact pads did not appear to be well defined. However, the acetone reacted with the passivation layer (which should have been resistant after the passivation bake) creating a very poor surface for subsequent processing. Thus the top contact layer was of poor quality, which resulted in trouble contacting it with probes during laser testing. However, a spectrum measurement was obtained from a Y-laser with bend radius $300\,\mu\text{m}$. The results are shown in figure 5.11. Both the increase in SMSR and large wavelength shift was demonstrated.

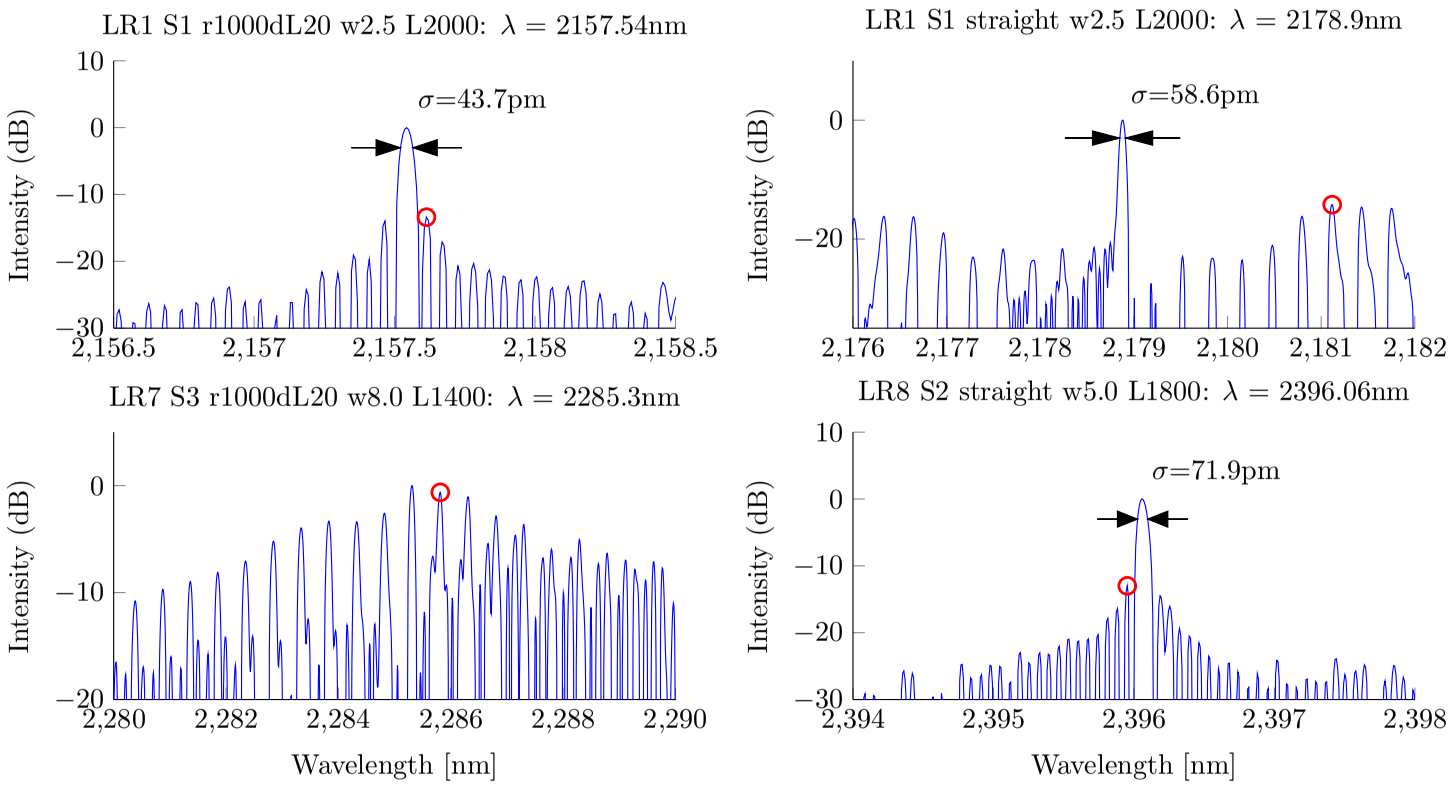

Figure 5.9: Comparison of measured spectra for some of the lasers, plotted on a logarithmic y-axis normalized on the intensity of the dominant mode. Single mode behaviour is observed in lasers with waveguide width smaller than or equal to 5 µm. The largest side-mode in the spectra has been marked with a red circle, and the full width at half-maximum (-3 dB in the log-plot) of the single mode lasers is shown.

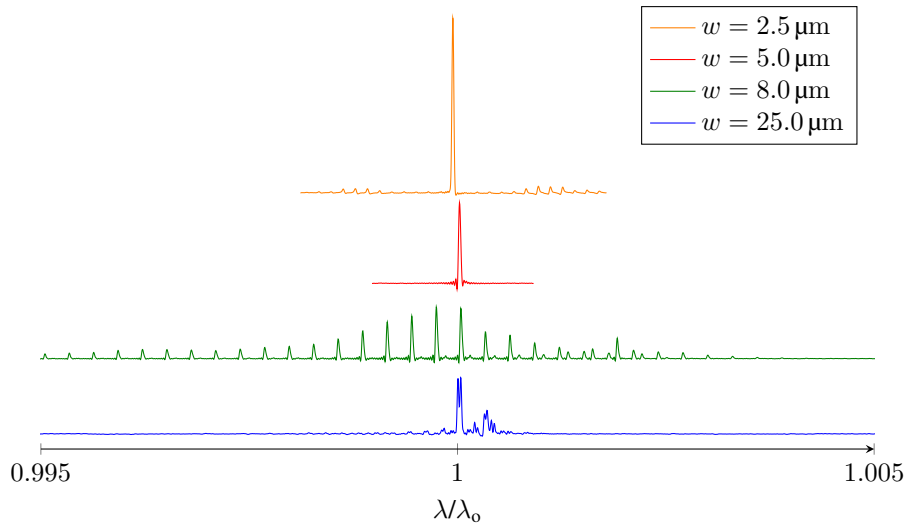

Figure 5.10: Spectrum vs. waveguide width w for some of the processed lasers. The spectra is plotted relative to the dominant mode wavelength (λ_0) of each individual laser. Lasers exhibit single mode behaviour for waveguide widths $w \leq 5.0\,\mu m$.

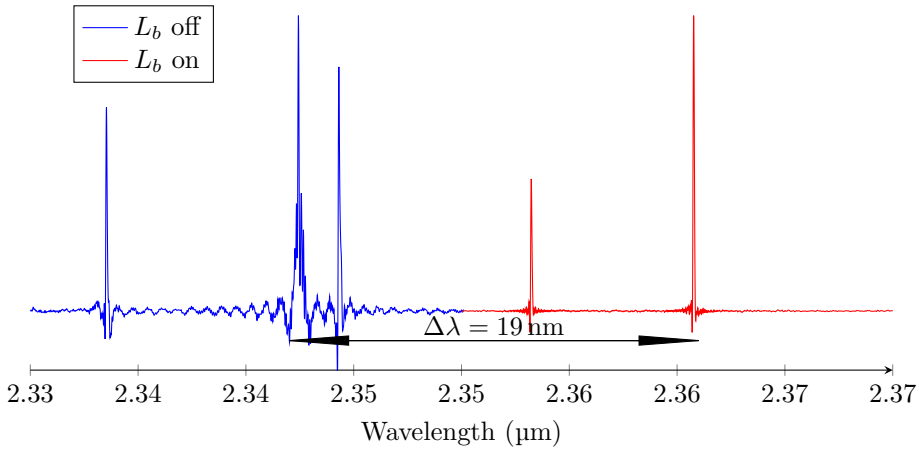

Figure 5.11: Spectrum of the Y laser with bend radius $r = 300\,\mu\mathrm{m}$ from sample LR8 Y1. The blue spectrum was measured when injecting $200\,\mathrm{mA}$ into only the common section L_c and straight section L_s (see figure 3.3). The red spectrum was measured injecting current also into the bent branch. The measurements illustrate two principles of the Y-laser; 1: the interference between the two cavities kills side modes improving the SMSR in the lasers. 2: When current is injected into the bent branch L_b, the emission wavelength of the dominant mode is shifted. In this test, a wavelength shift of $\Delta\lambda = 19\,\mathrm{nm}$ is observed, much larger than attainable by a FPL laser structure. A large side mode is observed in both the spectra before and after turning on the bent branch. The exact reason for this side-mode is not well explained by the theory[12] and could be subject for further investigation. It appears that the Y-laser acts as two separate resonators with two gain curves, each carrying a large dominant mode from the mode-comb spectra of the individual resonator.

Chapter 6

Conclusion and further work

To summarize, this work has presented the processing and characterization of mid-IR laser diodes related to the optimization and demonstration of junction structures as a potential candidate for largely wavelength tunable monochromatic light sources in gas sensing applications. In particular, the Y-junction laser structure and the related S-bend laser structure has been investigated.

Laser diodes with both shallowly-etched QIG-RW- and deeply-etched IG-RW structure have been fabricated and investigated. For the QIG-RW structure, it was found that a minimum lateral effective refractive index contrast of $\Delta n_{\text{eff}} = 0.037$ was needed for the curved waveguides to achieve lasing. In our laser structure this relates to a minimum etch depth of $1.4\,\mu\text{m}$. A new approach for controlling the etch depth was suggested, and initial tests showed that using this approach the etch depth was controllable to within $\pm 10\,\text{nm}$ of desired target. Using this approach, Δn_{eff} larger than 0.04 should be attainable in the current material system. Alternatively, lasers etched through the core have demonstrated lasing also for the waveguides with the largest curvature, due to the improved lateral waveguiding.

For the S-bend lasers, the shallow-etch QIG-RW lasers were found to have better lasing characteristics than the deep-etch IG-RW, including a lower threshold current density and increased slope effiency. The S-bend lasers with larger radius of curvature in the bend displayed better DQE, suggesting that optical loss increase for smaller bend radius.

The threshold current density in the laser samples were not found to fit well with an inverse

proportionality on the laser cavity length, thus the transparancy current density values could not be estimated. Similarly, the inverse quantum efficiency, did not appear to be linearly dependent on the cavity length, thus estimation of optical loss in the S-bend and straight waveguides could not be performed. The highly varying performance of the lasers on each bar was attributed to the chemical instability in the passivation layer during the back-contact annealing step. To combat this recurring problem in the passivation layer, an additional annealing step immediately after deposition of the passivation resist was suggested. Initial tests showed promising results, however lasers were not fabricated with this additional step due to time-constraints.

Lasers were found to emit in single-mode with approximately $13\,\mathrm{dB}$ SMSR for the S-bend structures with waveguide widths $5\,\mu\mathrm{m}$ and below. The lasers were found to emit around wavelength $2.2\,\mu\mathrm{m}$ and $2.4\,\mu\mathrm{m}$. Y-junction lasers were fabricated and the principle of large wavelength tunability ($19\,\mathrm{nm}$) and improved SMSR in the interferometric structure was demonstrated. However, due to poor metal contacts in the Y-junction laser sample, a more complete investigation into the tuning dynamics and behaviour of the Y-laser diodes was not possible.

Further work

Including the optimized steps in the fabrication process, fabrication of new S-bend lasers might give an improved insight into the loss mechanisms of the curved waveguide structure. Based on the current design of the mask, the total loss factor for the curved waveguides can be calculated. The radiation loss in the bend α_{bend} can be separated from the mode mismatch factors $T_{m1,2}$ to investigate which factor contributes more to the optical loss in the curved sections of the S-bend and related interferometric structures. Such an analysis could be of particular interest in the shallow-etch lasers, where α_{bend} can not be assumed to be small due to good confinement of the optical field. For such an analysis, a new mask containing S-bend waveguide designs, where the radius of curvature is kept constant while varying the arc angle θ, is needed.

Fabrication of Y-lasers using the optimized fabrication steps should result in lasers with stable operation. A more complete investigation into tuning behaviour and attainable tuning characteristics is needed before investigating the use of such lasers for gas detection systems. Additionally, fabrication of the other types of interferometric structures can be of interest to improve SMSR and tunability of the lasers.

Appendix A

Laser processing recipe

The following pages contain the recipe used for the laser processing. The recipe is constantly evolving and new steps are added to optimize the final result. The recipe here, reflects the latest changes, and not all steps were used in the processing of all the laser batches. The process typically takes one to two weeks depending on equipment availability, down-time, changes made to the equipment, number of samples in the batch etc.

Processing Run card, Y-junction laser nanolab

Sample:

Sample nr: _____
Sketch of sample:

Last update: July 12, 2015 by Kjetil Haddeland

Ridge Etch

Sample Clean 1. 5 min in Acetone 2. 5 min in Ethanol 3. 5 min in IPA 4. IPA rinse 5. DIW rinse + immediate N2 dry 6. Dehydration bake 150 C / 10 min	Comments:
Photolitography 1. Spin AZ5214E @ 4000 rpm / 46s / 4000 rpm/s 2. Clean backside of sample carefully with a swab moisted with acetone if resist is present 3. Soft bake 110 C / 50 s 4. Edge bead removal exposure 700-800 mJ/cm^2 5. Develop until edge bead is gone (approx 25s) + N2 dry 6. Softbake 95C / 30-60s 7. Hard Contact Exposure - 150 mJ/cm2 8. Develop in AZ 726 MIF 25-30 s (Varies from run to run, keep an eye on it, always use a test) 9. Spin dry @ 1000 rpm / 45 s 10. Inspection: Get waveguide in focus, then over and underfocus to check profile. Redo if the profile is not nearly vertical.	Comments:

ICP-RIE etch
 	
1. Check that it has been used for Cl-gases
    1. Run cleaning and conditioning recipe.
    2. Or, conditioning recipe (15min).
2. Recipe: Anisotropic GaSb etch.
3. Do test run with test sample (preferably cladding sample, or alternatively GaSb)
4. Check etch rate from test sample and correlate to endpoint detection data.
	Comments:

5. Etch to desired etch depth (typically 100 nm above core)
    1. Endpoint detection (control etch depth with high accuracy)
6. PR removal
    1. Remove PR by putting sample in acetone (5-15 min)
        1. If not removed - use acetone gun ~~or swabs~~
    2. Rinse immediately in IPA + N2 dry
7. Rinse sample in running DIW for 5 min (Cl-removal)
8. (Optional) Check ridge clean with SEM (Table-top)	

Passivation, Resist

Do for all samples

Sample Clean
 	
~~1. 5 min plasma clean~~
~~2. Acetone + IPA rinse + N2 dry~~
~~3. Dehydration bake 150 C / 10 min~~
    ~~1. (disadvantage) Oxidation of sidewall~~
    2. ~~(advantage) Better adhesion for passivation resist~~
	Comments:

Resist 1. Spin ma-N 440 @ 7000 rpm / 37 s / 1000 rpm/s 2. Clean backside of sample carefully with a swab moistened with acetone if resist is present 3. Soft bake: 60 s @ 95C 4. Place sample on 3" Si wafer on black ceramic hot plate @ 100 C (TC) 5. Ramp to 160 C, bake at 160 C for 5 minutes 6. Start timer for 2 minutes, ramp to 260 C (TC) 7. Take off sample after 3 minutes (including ramp time, so approx 1 min at 260C) 8. (new) Run the annealing recipe for the back contact to fully passivate the resist and avoid issue with resist shrinking and void generation later on.	Comments:
Etch Back, RIE 1. Do condition run, recipe: "(Nam) PR etchback ***" for 10-30 minutes (plasma should be yellow not blue) 2. Edge bead removal etch 1. Put Si piece on top of sample and etch with O2/CF4 fast rate for about 10 mins. 3. Etch sample(s), recipe: "(Nam) PR etchback slow rate" for 5.5-6 minutes until ridge is clean	Comments:

1. Do many etches, e.g. 2-3-1 minutes, and check result every time (microscope / profilometer) 4. Inspect in microscope and SEM to ensure ridge is clean. 5. When ridge is clean, check sidewall exposure with profilometer.	

Top contact layer

Sample Clean 1. Acetone + IPA rinse + N2 dry 2. 10 min dehydration bake 150 C	Comments:
Photolitograhy - Spin AZ5214E @ 4000rpm / 46s / 4000rpm/s - Softbake @110^{0}C / 50s - Edge bead removal exposure 700-800 mJ/cm^2 - Develop EB (30-60s) + Softbake 95^{0}C / 30-60s - Exposure 18 mJ/cm^2 - Image-reversal bake 112^{0}C for 120s - Flood exposure 200 mJ/cm^2 - Develop in AZ726 MIF for 40s - DIW rinse - Dry with N_2	Comments:
Metallization ~~1. Do a 1 minute 50 W, 30 % O2 plasma clean~~ 2. Oxide removal by Ar sputter: 16W / 1 min. 3. Metallization: Ti/Pt/Au 50/25/325 nm (for bonding) Increase Au layer to avoid disconnect due to passivation resist valleys, e.g. 650nm	Comments:

Lift-off.	Comments:

1. Put sample in closed container for 15-30 minutes
2. If lift-off is not successfull, try following
    1. Spray sample with acetone gun (1-2 minutes)
    2. Ultrasonic in plastic beaker (max 20 minutes)
3. Clean sample in ethanol + IPA + N2 rinse
4. Inspect sample	

Bottom contact, Lapping

Done at Supporting lab

Sample mount	Comments:
1. Find "slipeklokke" for mounting sample on 2. Take off metal piece in center and put on hot plate, 150 C 3. Check sample thickness, and write it down 4. Put crystalbond 509 on metal piece, and make it flat and thin 5. Place sample, backside up on waxed metal piece and cover sample in more wax (to protect the edges during lapping) 6. Mount sample on "slipeklokke" and set it to 170-200 µm 1. sample should be 100-150 µm thick when done, 120-150 µm is probably safer with regards to breakage. Remember that you must account for the wax thickness	

Lapping	Comments:
1. Find some lapping sheets, the ones marked 4000 2. Either lap it in a fume cupboard or using a spinner with suction, avoid breathing in the antimony particles. Use plenty of water. 3. Remember to throw the lapping sheet and particles into toxic waste, e.g. use the box in the MBE lab. 4. Clean off the sample and remove it from the metal piece using the hot plate again. Slide it off carefully 5. Put it in acetone for 1-2 hours to dissolve the remaining wax 6. Clean sample in acetone+IPA+N2 blow (never let acetone dry on sample) 7. Inspection	

Bottom contact, Metallization

Done at nanolab.

Mounting 1. Clean and dehydrate a piece of silicon large enough to fit all samples 2. Spin ma-N 440 @ 1000 rpm / 30 s 3. Place all samples, backside up, on the photoresist *BEFORE* baking 4. Soft bake 110 C / 8-10 minutes	Comments:
Metallization 1. Oxide removal: Argon Sputter 16W, 1min 2. Do n-type contact deposition 1. Pd/Ge/Au/Pt/Au 87Å/560Å/233Å/476Å/2000Å (Vogt et al.)	
De-mount 1. Place samples in acetone for 1 hour in closed beaker (as always) 2. Remove and clean acetone + ipa + n2 dry 3. Inspect	

Bottom contact, Annealing

Done at Nanolab.

Rapid thermal annealer 1. Use annealing recipe in the RTP (Nam/Kjetil) 2. Use Susceptor for III-V annealing 3. Run recipe w/o sample 1. Check annealing temperature stays within 290 +/- 10C for 45s (critical for good contact) 4. Run recipe w/ sample. 5. Inspect	Comments:

Scribing

Supporting lab, nanolab.

1. Mount sample on blue tape 2. Make a recipe based on the length of the laser 3. Make sure you hit the laser at the end - will be difficult!! Machine not calibrated 1. **DO NOT** scribe across the ridge - the laser will not work (just cleave)	Comments:

2. Use edge scribes for scribing perpendicular to the ridge 1. Recipe by Kjetil, use interactive mode.	

Mounting and bonding

Either nanolab or basement at IET

1. Glue laser to a laser copper plate using silver epoxy or silver glue
2. Tape the bonding pads to the copper with kapton tape (double sided)
    1. Bonding pads must have soldered on wires BEFORE taping them to the copper
3. Wirebond the laser contacts to the laser bonding pads.

1. Bonding settings, nanolab:

T = 118 C

Ultrasonic:	180	280
Time:	100	55
Force:	85	65

Tail: 300
Feed +/- 12

1. Should be ready for testing! (If test setup in FTIR lab is operational)

Appendix B

Excerpts from mask 1

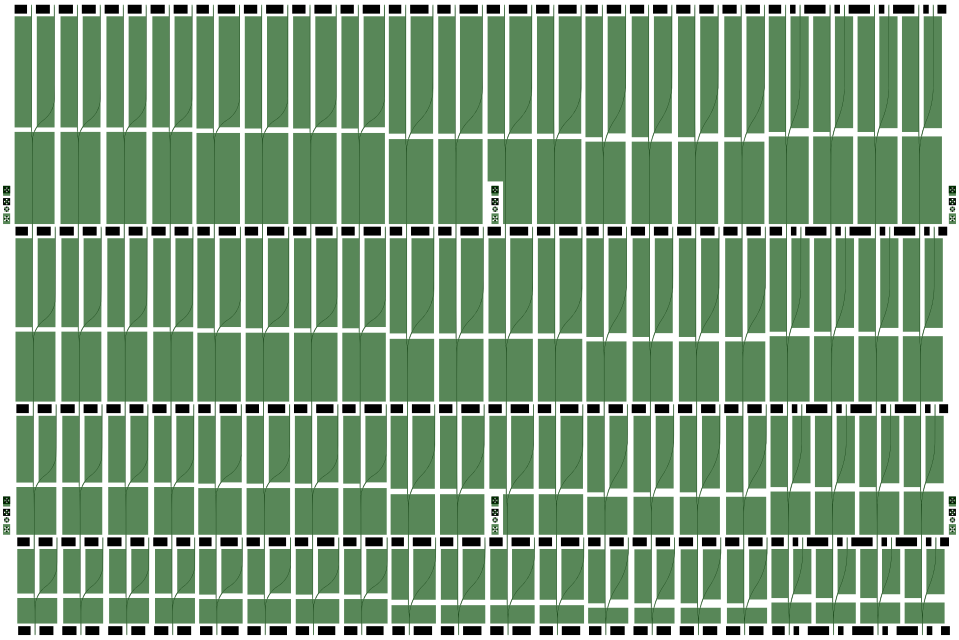

Figure B.1: Excerpt from mask 1: Y-laser waveguide etch pattern (black) and corresponding metallization pattern (green overlay). Design parameters: $L = (1.0, 1.5, 2.0 \text{ and } 2.5)\,\mathrm{mm}$, $w = (1.5, 2.0 \text{ and } 2.5)\,\mu\mathrm{m}$, bends (from left): $4\times$(r300dL80, r300dL100, r500dL80, r750dL50 and r1000dL20).

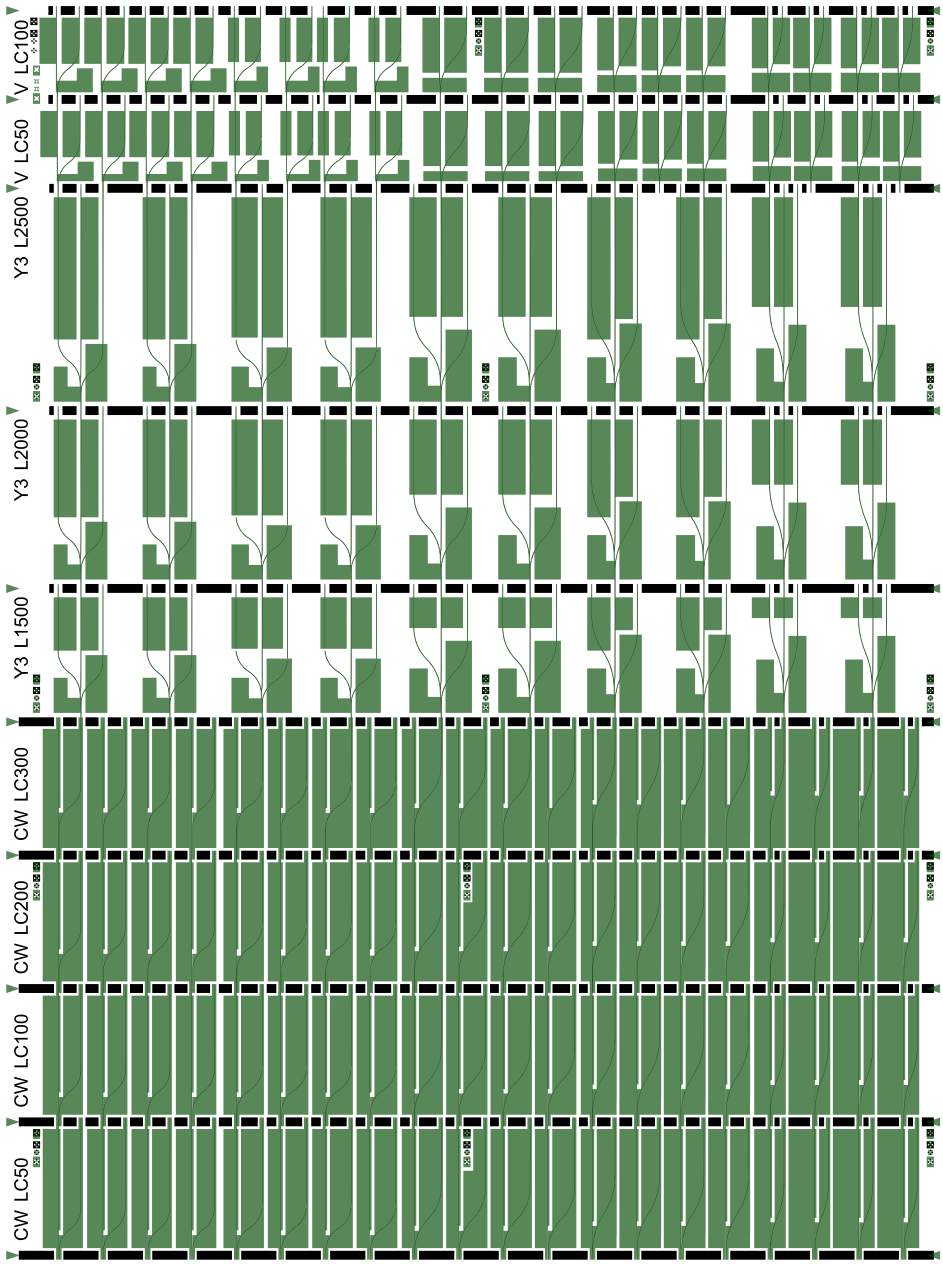

Figure B.2: Excerpt from mask 1: Combined 1 (CW/Y3/V) waveguide etch pattern (black) and corresponding metallization pattern (green overlay). Design parameters: $L = (1.0,\ 1.5,\ 2.0$ and $2.5)\,\mathrm{mm}$ for CW lasers, $L = (1.5,\ 2.0$ and $2.5)\,\mathrm{mm}$ for Y3 lasers, $L = 1.0\,\mathrm{mm}$ for V. $w = 2.5\,\mu\mathrm{m}$. Bends: (r300dL80, r300dL100, r500dL80, r750dL50 and r1000dL20). Coupling gap for CW: $(2,\ 3,\ 4$ and $5)\,\mu\mathrm{m}$. Coupling length for CW: $(50,\ 100,\ 200$ and $300)\,\mu\mathrm{m}$. Combined branch length L_C for V: $(50$ and $100)\,\mu\mathrm{m}$.

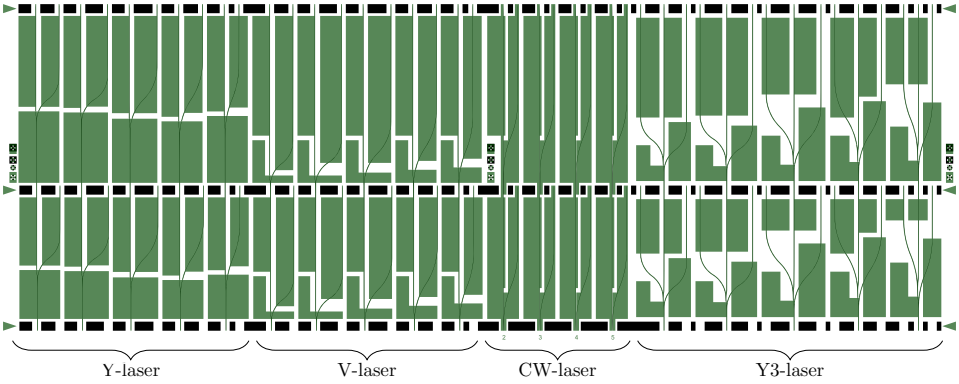

Figure B.3: Excerpt from mask 1: Combined 2 (Y/V/CW/Y3) waveguide etch pattern (black) and corresponding metallization pattern (green overlay). Design parameters: $L = (1.5 \text{ and } 2.0)\,\mathrm{mm}$, $w = 2.5\,\mu\mathrm{m}$, bends for Y, V and Y3: (r300dL80, r300dL100, r500dL80, r750dL50 and r1000dL20), bends for CW: r1000dL20. Coupling width for CW: $(2,\ 3,\ 4 \text{ and } 5)\,\mu\mathrm{m}$. Coupling length for CW: $(50 \text{ and } 200)\,\mu\mathrm{m}$. Combined branch length L_C for V: $50\,\mu\mathrm{m}$.

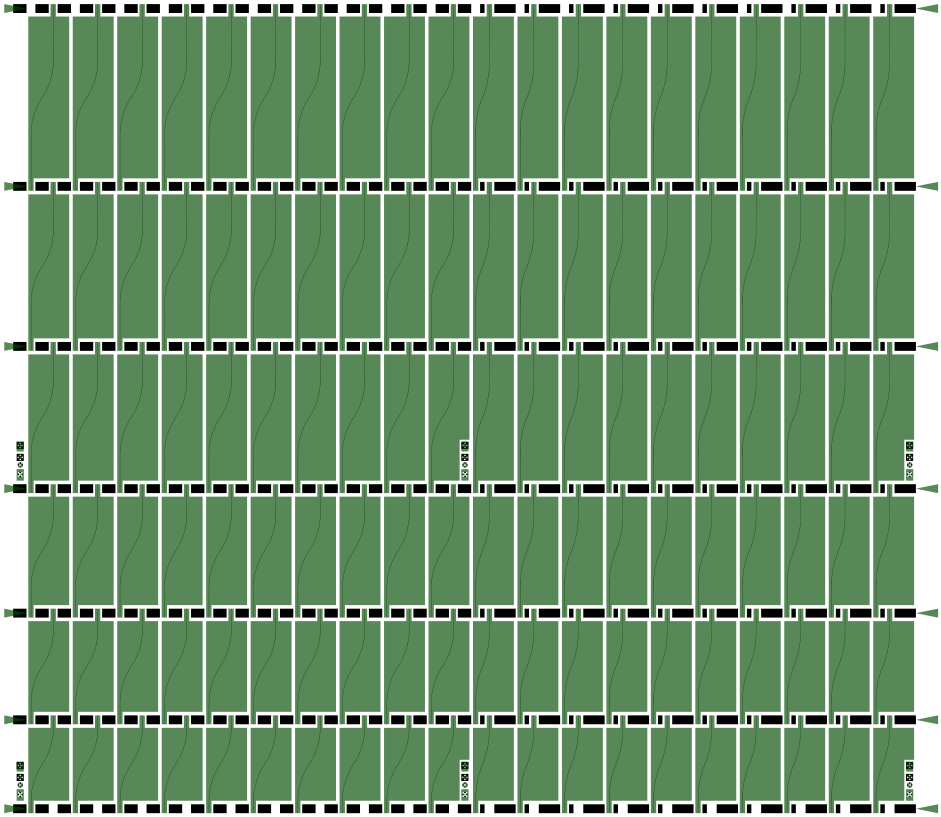

Figure B.4: Excerpt from mask 1: S-bend r750dL50 & r1000dL20 waveguide etch pattern (black) and corresponding metallization pattern (green overlay). Design parameters: $L = (1.0,\ 1.2,\ 1.4,\ 1.6,\ 1.8 \text{ and } 2.0)\,\mathrm{mm}$. $w = (2.0 \text{ and } 2.5)\,\mu\mathrm{m}$.

Appendix C

Excerpts from mask 2

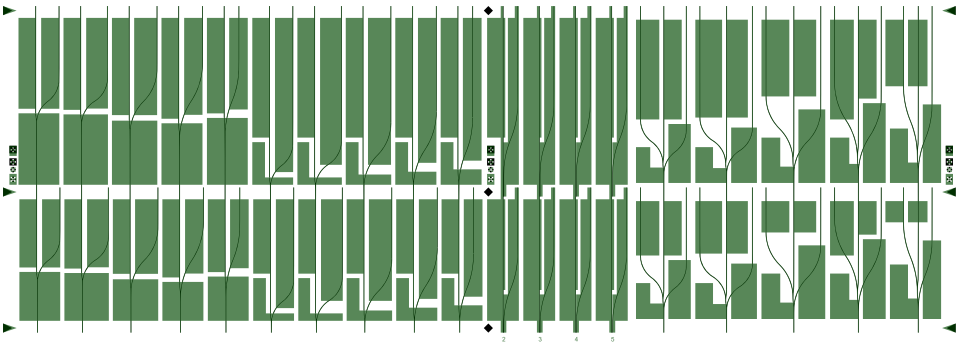

Figure C.1: Excerpt from mask 2: Combined 2 (Y/V/CW/Y3) waveguide etch pattern (black) and corresponding metallization pattern (green overlay). The distribution of the lasers is as in figure B.3, but the support structures have been omitted. The critical dimension of the pattern is $1\,\mu\mathrm{m}$ in the separation of the metal contacts for the CW-lasers, and due to a flaw in the order of the first mask, it was fabricated with a larger critical dimension, thus the gap between the metal contacts were not well defined. Therefore, the metallization pattern was readded to mask 2, although identical to that in mask 1. Design parameters: $L = (1.5 \text{ and } 2.0)\,\mathrm{mm}$, $w = (2.5 \text{ and } 5.0)\,\mu\mathrm{m}$, bends for Y, V and Y3: (r300dL80, r300dL100, r500dL80, r750dL50 and r1000dL20), bends for CW: r1000dL20. Coupling width for CW: $(2, 3, 4 \text{ and } 5)\,\mu\mathrm{m}$. Coupling length for CW: $(50 \text{ and } 200)\,\mu\mathrm{m}$. Combined branch length L_C for V: $50\,\mu\mathrm{m}$.

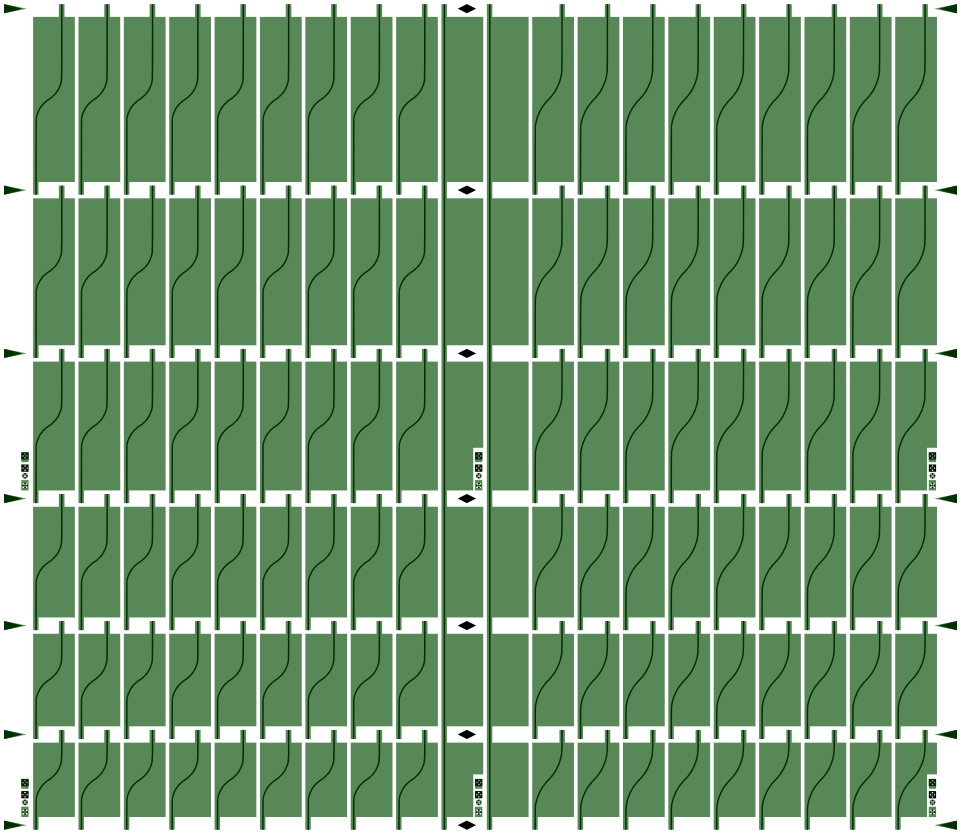

Figure C.2: Excerpt from mask 2: S-bend r300dL100 & r500dL80 waveguide etch pattern (black) and corresponding metallization pattern (green overlay). The design is as in mask1 omitting the support structures, except two S-bend waveguides in the middle of the pattern were swapped with straight waveguides, such that every batch of lasers has a reference straight laser waveguide. Due to this change in the waveguide etch pattern, the metallization pattern needed to be changed accordingly. Design parameters: $L = (1.0, 1.2, 1.4, 1.6, 1.8 \text{ and } 2.0)\,\mathrm{mm}$. $w = (2.5, 5.0, 8.0, 15.0 \text{ and } 25.0)\,\mu\mathrm{m}$. S-bend lasers with support structures and $w = 5.0\,\mu\mathrm{m}$ were also added to the mask.

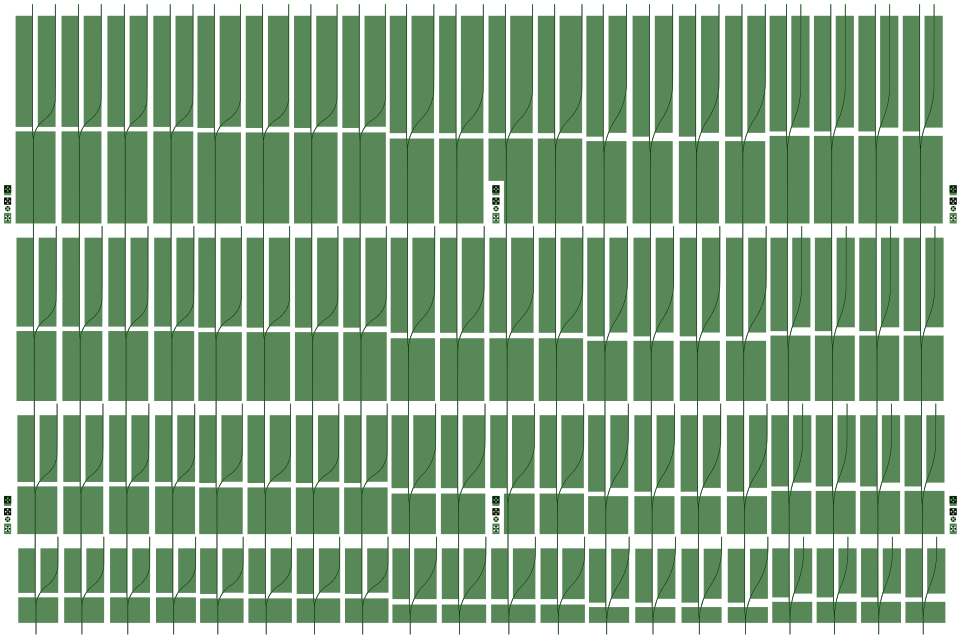

Figure C.3: Excerpt from mask 2: Y-laser waveguide etch pattern (black) and corresponding metallization pattern (green overlay). The design is identical to that in mask 1, omitting the support structures. Design parameters: $L = (1.0, 1.5, 2.0 \text{ and } 2.5)\,\mathrm{mm}$, $w = (1.5, 2.5 \text{ and } 5.0)\,\mu\mathrm{m}$, bends (from left): $4\times$(r300dL80, r300dL100, r500dL80, r750dL50 and r1000dL20).

Appendix D

Analyzing FPL results

Due to the large number of lasers processed, a MATLAB program was made to stream-line the plotting of L-I and V-I curves, from which to analyze the average DQE and threshold current density, plot inverse DQE vs. cavity length, and threshold current vs. inverse cavity length. A screenshot of the program is shown in figure D.1. Data can be selected from an excel file which should contain laser data from one laser bar with the same bend type in the column format (I-P1-V1-P2-V2-P3-V3...), where I is the injection current data, P the light output power, V the diode voltage and (1,2,3...) refers to the laser sample on the particular bar.

The correct parameters for the current laser bar must be inserted, including waveguide type (straight, r300dL80 etc.), waveguide width, cavity length and central lasing wavelength (necessary to calculate the DQE). The range of the data in the excel file can be selected manually, in which case the excel file will open and the range must be selected by the mouse before continuing. If only light power (P) or voltage data (V) is available, check-boxes can be marked including what data should be plotted. Obviously, calculations of the DQE or threshold current density, can not be performed without the light power data. The plots can be plotted with only the mean curve, which simply takes the mean of all P or V values in each row of the data, with each sample curve or with both. The mean curve is plotted as a dashed thicker curve, to distinguish itself.

It was found that it was not simple to extract the slope of the curves directly from the data points. Therefore, an algorithm was made to fit a curve to the data using shape language

modeling (SLM)[26]. The principle of this method consists of using cubic splines and to set requirements for these splines in specific regions of the plot. The typical L-I plot is shown in figure 5.1. For this plot we know there will be a certain region in the data that is zero, the so-called off-region, for which we can force the splines in that region to be constantly zero. In the turn-on region, we expect the light-output to gradually increase, so we can force the splines in this region to have an upwards curvature, or positive double derivative. The threshold current density was defined as the point with the largest curvature in this region, at which point the lasers go from a gradually increasing spontaneous emission process, to a linearly increasing stimulated emission process. In the linear region, the splines are forced to have a constant slope, while in the saturation region, we expect to see a decline in the slope, i.e. negative curvature, thus the double derivative can be forced negative here. The trick is to find where in the data the different regions start. Finding the off-region is as simple as looking for the data points that are zero. The end of the turn-on region, in which spontaneous emission processes are dominating, was selected by a power threshold, set to $0.25\,\mathrm{mW}$ based on inspection of the data. Finding the point where the linear region ends is tricker, thus this was decided by trial and error, i.e. by selecting a specific ratio of the total injection current range in the data, attempting to fit the data and checking if a good fit was obtained. A similar method was used to fit a curve to the V-I data. Typical plots of the L-I and V-I curves using the option to include plots for all samples are shown in figure D.2 and D.3.

For each laser bar plotted, the results will accumulate in the results table, and the corresponding inverse DQE and threshold current density values of each bar will be plotted in their respective plots. When data from three or more bars have been added, a linear regression line will be plotted for both the inverse DQE and threshold current density plots, in order to analyze the intercept point and slope, from which the internal quantum efficiency, internal loss and transparancy current density can be calculated (see section 5.1). The linear fit lines are weighted on the amount of laser samples in a given bar. In addition, a 95% confidence limit can be plotted. The confidence limits are only based on the statistics of the mean data points and the weights given, and does not take into consideration the standard deviation (shown by error bars).

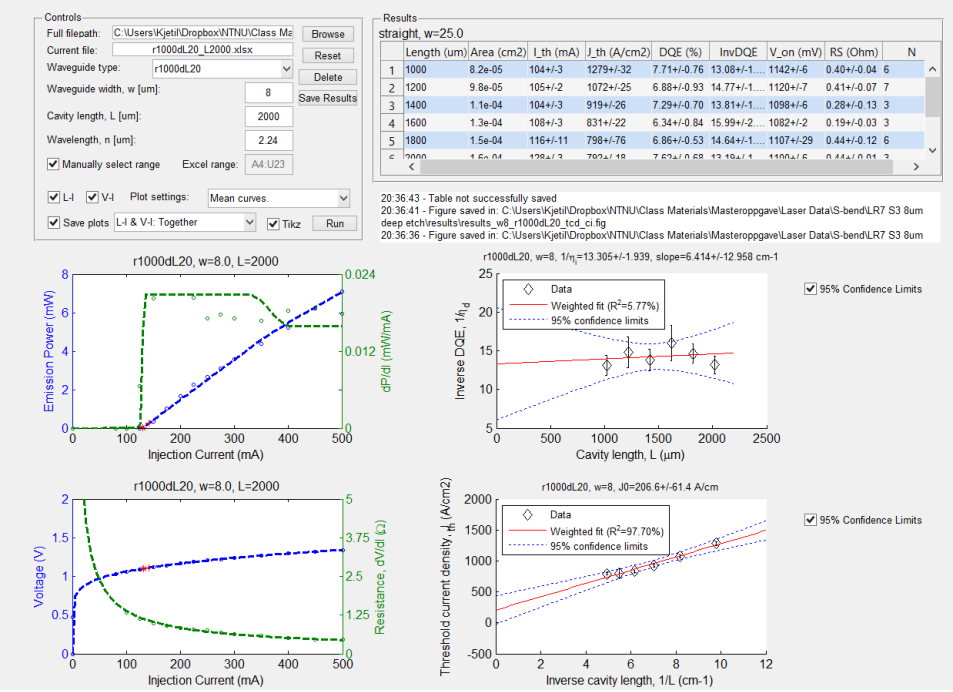

Figure D.1: A screenshot of the MATLAB program created to analyze the results of the FPL. The screenshot shows the test results from lasers with bend r1000dL20 in sample LR7 S3.

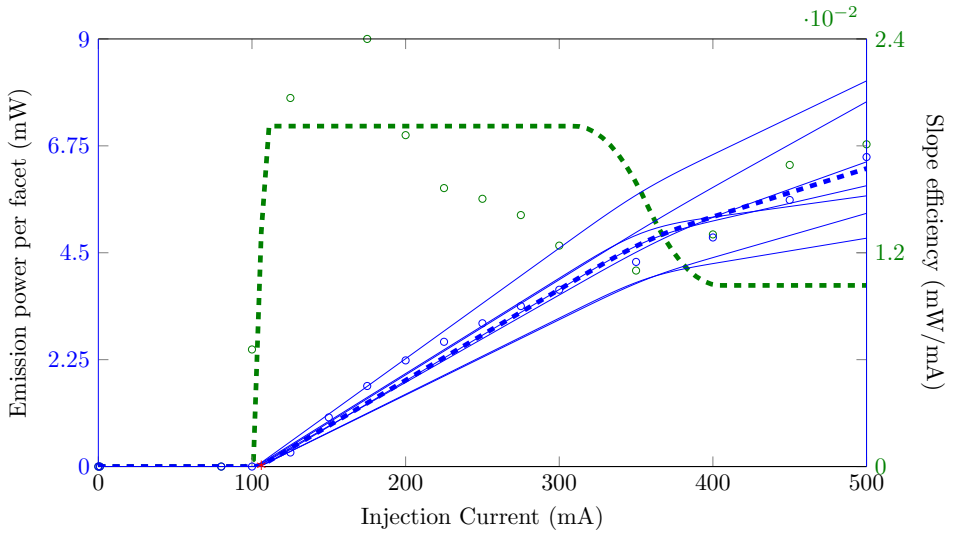

Figure D.2: L-I plot of laser bar r1000dL20 L1200 on sample LR7 S3. The thicker dashed line is the average curve. The slope of the average L-I curve is also plotted. The plateau in the slope is where the slope efficiency used for calculations of DQE is drawn from. The actual slope gradient calculated numerically by the central difference theorem are plotted as small green circles. The L-I curves for the different samples can be seen to vary alot. This is reflected in the standard deviation of the inverse DQE as shown by error bars (see figure D.1). The mean DQE is calculated by taking the mean of the DQE from each laser sample, rather than calculating the DQE of the mean curve. The mean threshold current density is calculated similarly.

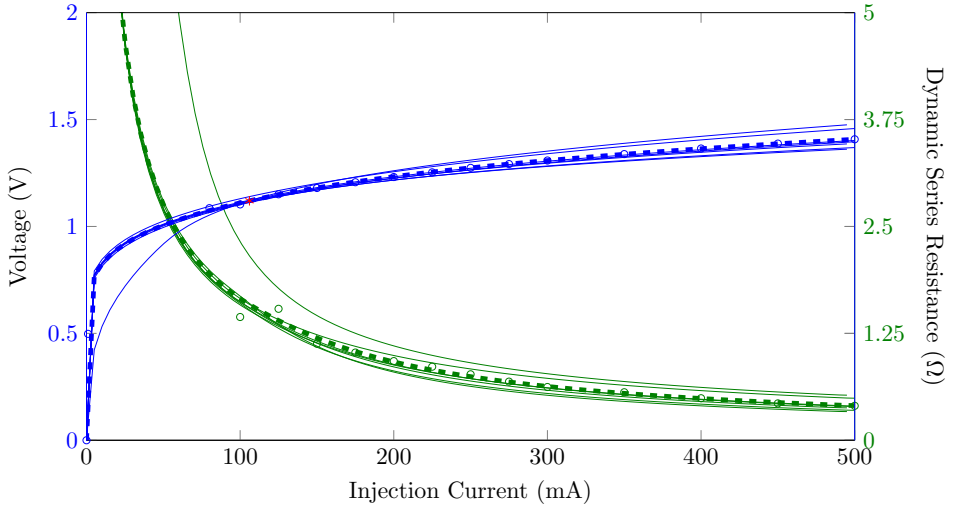

Figure D.3: V-I plot of laser bar r1000dL20 L1200 on sample LR7 S3. Again, the thicker dashed line corresponds to the average curves. The dynamic series resistance, i.e. the slope of the V-I curve, is plotted in green. The lasers on each bar typically exhibit very similar diode characteristics.

Acronyms

CW coupled wave. 46

DQE external differential quantum efficiency. 59–62, 69, 72–74, 79, 97, 98, 100

EBR edge-bead removal. 28, 37

FCPE free-carrier plasma effect. 15
FP Fabry-Perot. 3, 10, 12, 15, 19–21, 43, 72
FPL Fabry-Perot laser. vi, 10, 15, 20–22, 60, 67, 69, 72, 78, 97, 99
FSR free spectral range. 12, 22
FTIR fourier transform infra-red spectroscopy. 62, 64, 72

GRINSCH graded refractive index separate confinement heterostructure. 14

ICP-RIE inductively coupled plasma reactive ion etching. 29, 35–37, 45, 46, 49
IG index guided. 32
IG-RW index guided ridge waveguide. 33, 34, 79
IQE internal quantum efficiency. 59–61, 72, 74

MQW multiple quantum well. 14, 32

PR photoresist. 28, 29, 31, 37, 38, 41, 42, 46, 47, 50–55

QIG quasi-index guided. 32
QIG-RW quasi-index guided ridge waveguide. 33, 43, 46, 79
QW quantum well. 13, 14

RW ridge-waveguide. 17, 32, 33, 38, 40, 41, 47, 52, 57

SCH separate confinement heterostructure. 14

SEM scanning electron microscopy. 31, 32, 37, 42, 43, 48–53, 66
SMSR side mode suppression ratio. 3, 21, 59, 72, 75, 78, 80

TDLAS tunable diode laser absorption spectroscopy. 2, 3, 59, 72
TLD tunable laser diode. 2, 3

Bibliography

[1] M. Lackner, “Tunable diode laser absorption spectroscopy (TDLAS) in the process industries - A review,” *Reviews in Chemical Engineering*, vol. 23, no. 2, pp. 65–147, 2007.

[2] M Lackner, G Totschnig, F Winter, M. A. Maiorov, D. Z. Garbuzov, and J. C. Connolly, “In situ laser measurements of CO and CH4 close to the surface of a burning single fuel particle,” *Measurement Science and Technology*, vol. 13, no. 10, pp. 1545–1551, 2002.

[3] J. Buus, M.-C. Amann, and D. J. Blumenthal, *Tunable laser diodes and related optical sources*. Hoboken, N. J.: John Wiley & Sons, 2005, xiv, 390 s. : ill.

[4] J Seufert, M Fischer, M Legge, J Koeth, R Werner, M Kamp, and A Forchel, “DFB laser diodes in the wavelength range from 760 nm to 2.5 um.,” *Spectrochimica acta. Part A, Molecular and biomolecular spectroscopy*, vol. 60, no. 14, pp. 3243–7, 2004.

[5] M. Ortsiefer, G. Bohm, M. Grau, K. Windhorn, E. Ronneberg, J. Rosskopf, R. Shau, O. Dier, and M.-C. Amann, “Electrically pumped room temperature CW VCSELs with 2.3 um emission wavelength,” *Electronics Letters*, vol. 42, no. 11, p. 640, 2006.

[6] L. Rothman, I. Gordon, Y. Babikov, A. Barbe, D. Chris Benner, P. Bernath, M. Birk, L. Bizzocchi, V. Boudon, L. Brown, A. Campargue, K. Chance, E. Cohen, L. Coudert, V. Devi, B. Drouin, A. Fayt, J.-M. Flaud, R. Gamache, J. Harrison, J.-M. Hartmann, C. Hill, J. Hodges, D. Jacquemart, A. Jolly, J. Lamouroux, R. Le Roy, G. Li, D. Long, O. Lyulin, C. Mackie, S. Massie, S. Mikhailenko, H. Müller, O. Naumenko, A. Nikitin, J. Orphal, V. Perevalov, A. Perrin, E. Polovtseva, C. Richard, M. Smith, E. Starikova, K. Sung, S. Tashkun, J. Tennyson, G. Toon, V. Tyuterev,

and G. Wagner, "The HITRAN2012 molecular spectroscopic database," *Journal of Quantitative Spectroscopy and Radiative Transfer*, vol. 130, pp. 4–50, 2013.

[7] B. E. A. Saleh and M. C. Teich, *Fundamentals of photonics*, 2nd. New Jersey: Wiley, 2007.

[8] M. Breivik, "Fabrication of mid-infrared laser diodes for gas sensing applications," Doctoral Thesis, Norwegian University of Science and Technology, 2013.

[9] A. Yariv and P. Yeh, *Photonics: optical electronics in modern communications*, 6th ed. Oxford Univerisity Press, 2007.

[10] K. Haddeland, "GaSb S-bend Laser: Fabrication and Characterization."

[11] T.-N. Tran, private communication, 2014–2015.

[12] K. Dutting and O. Hildebrand, "Analysis and simple tuning scheme of asymmetric Y-lasers," *IEEE journal of Quantum Electronics*, vol. 30, no. 3, pp. 654–659, 1994.

[13] M. Kuznetsov, "Design of widely tunable semiconductor three-branch lasers," *Lightwave Technology, Journal of*, vol. 12, no. 12, pp. 2100–2106, 1994.

[14] M. Quirk and J. Serda, *Semiconductor manufacturing technology*. New Jersey: Prentice-Hall, Inc., 2001.

[15] *AZ5214E - Image Reversal Resist Data Sheet*, `http://www.microchemicals.com/micro/az_5214e.pdf`, visited Dec. 2014, Micro Chemicals.

[16] A. Lipson, S. G. Lipson, and H. Lipson, *Optical physics*. Cambridge: Cambridge University Press, 2011, xviii, 572 s. : ill.

[17] R. F. Egerton, "The Scanning Electron Microscope," in *Physical Principles of Electron Microscopy*, New York: Springer, 2005, ch. 5, pp. 125–153.

[18] T.-N. Tran, M. Breivik, S. K. Patra, and B. O. Fimland, "High precision AlGaAsSb ridge-waveguide etching by in situ reflectance monitored ICP-RIE," in *Proceedings of SPIE - The International Society for Optical Engineering*, vol. 9134, SPIE, May 2014.

[19] J. A. Gupta, P. J. Barrios, J. Lapointe, G. C. Aers, and C. Storey, "Single-mode $2.4\,\mu\mathrm{m}$ InGaAsSb/AlGaAsSb distributed feedback lasers for gas sensing," *Applied Physics Letters*, vol. 95, no. 4, p. 041 104, 2009.

[20] A. Vogt, A. Simon, H. L. Hartnagel, J. Schikora, V. Buschmann, M. Rodewald, H. Fuess, S. Fascko, C. Koerdt, and H. Kurz, "Ohmic contact formation mechanism of the PdGeAu system on n-type GaSb grown by molecular beam epitaxy," *Journal of Applied Physics*, vol. 83, no. 12, p. 7715, 1998.

[21] K. S. Mobarhan, *App note 1: Test and Characterization of Laser Diodes: Determination of Principal Parameters*, `http://www.newport.com/servicesupport/PDF_Files/APPNOTE1.pdf`, visited Dec. 2014, Newport Corporation.

[22] J. Wang, W. Yuan, C. S. Seibert, and D. C. Hall, "Loss characterization of high-index-contrast ridge waveguide oxide-confined inalgaas quantum well racetrack ring-resonator lasers," *Proceedings of SPIE*, vol. 7230, pp. 1–12, 2009.

[23] J. P. Hohimer, D. C. Craft, G. R. Hadley, G. a. Vawter, and M. E. Warren, "Single-frequency continuous-wave operation of ring resonator diode lasers," *Applied Physics Letters*, vol. 59, no. 26, pp. 3360–3362, 1991.

[24] B. C. Smith, *Fundamentals of Fourier transform infrared spectroscopy*. Boca Raton, FL: CRC Press, 2011.

[25] N. Kagawa, O. Wada, and R. Koga, "Suppression of the étalon fringe in absorption spectrometry with an infrared tunable diode laser," *Optical Engineering*, vol. 36, no. 9, pp. 2586–2592, 1997.

[26] J. D'Errico, *(SLM) - Shape Language Modelling*, `http://www.mathworks.com/matlabcentral/fileexchange/24443-slm-shape-language-modeling/`.